SPECTROSCOPY AND PHOTOCHEMISTRY OF METAL-OXO COMPLEXES

Thesis by

Jay Richmond Winkler

In Partial Fulfillment of the Requirements

for the Degree of

Doctor of Philosophy

California Institute of Technology

Pasadena, California

1984

(Submitted August 16, 1983)

ACKNOWLEDGMENT

My first thanks go to Professor Harry B. Gray for his help, advice, support, encouragement, and friendship during the past five years. I am indebted to him for permitting me to see how chemistry is done the Gray-way.

Caltech is a marvelous place and innumerable faculty members, visitors, and fellow students here have taught me a great deal for which I am very grateful. I am thankful for the opportunity to have worked with Milo Bordignon, John Chesick, George McLendon, and Israel Pecht. I would also like to acknowledge John Buhr, Dan Buttry, Mike Hopkins, Andy Maverick, Vinnie Miskowski, Dan Nocera, Mark Paffett, Steven Rice, Terry Smith, Peter Wolczanski, and Tom Zietlow for many helpful discussions. A special acknowledgment goes to Dr. O. R. Wulf for his friendly salutations and interesting conversation.

A number of individuals outside Caltech considerably brightened my existence (often just before clouding it with a hangover) and for these pleasant diversions I wish to thank Fo, George, Hollywood, Horan, Jamie, Jinx, Noah and his Red Sox, and Shou.

Three close friendships have been particularly important to me during my stay at Caltech. Dan and Karen Nocera have borne too much of my company and I thank them for their tolerance. Melissa Patton deserves special thanks for putting up with me, especially when I was talking more to myself than to her.

I am eternally grateful to my parents and sisters for their

unfailing and unfathomable support and encouragement in the past twenty-seven years.

Finally, I would like to acknowledge the Sun Company for a graduate fellowship in the 1982-83 academic year.

ABSTRACT

Electronic spectroscopic, photophysical, and photochemical investigations of two types of metal-oxo complexes are described. The electronic absorption spectra of various molybdenyl ions (MoO^{3+}) were measured in crystals and solutions. These spectra clearly support $^2B_1(\underline{x}^2-\underline{y}^2) \leftarrow {}^2B_2(\underline{xy})$ and $^2E(\underline{xz},\underline{yz}) \leftarrow {}^2B_2(\underline{xy})$ assignments for the two weak bands near 25,000 and 14,000 cm^{-1}, respectively, in these molecules. A Franck-Condon analysis of the $^2B_1 \leftarrow {}^2B_2$ band in the 5 K single crystal absorption spectrum of $(Ph_4As)MoOCl_4$ indicated a 0.07(1) Å elongation of the metal-chloride bond in the excited state. Crystalline $(Ph_4As)MoOCl_4$ luminesces from the lower energy component of a split $^2E(\underline{xz},\underline{yz})$ state with a lifetime of 160 ns at 300 K, increasing to 1.4 μs at 5 K. No luminescence was detected from any molybdenyl ion in solution.

The electronic absorption and emission spectra of $\underline{trans}$-$ReO_2L_4^z$ (L = CN^-, z = 3-; L = $\frac{1}{2}$(ethylenediamine), z = +; L = pyridine, z = +; L = 4-picoline, z = +; L = 4-$\underline{t}$-butylpyridine, z = +) were also measured in crystals and solutions. The lowest energy absorption bands are assigned to components of a split $^3E_g[(e_g)^1(b_{2g})^1]$ state (ground state $^1A_{1g}[(b_{2g})^2]$). Emission from at least two of these components was identified in the cyanide and pyridine complexes and only the ethylenediamine complex failed to luminesce. Franck-Condon analyses of the emission spectra indicated $\underline{ca.}$ 0.1 Å elongations of each Re-O bond in the ^3E_g excited states. The lifetime of the ^3E_g state varies from 10 to 300 μs in crystals and is $\underline{ca.}$ 10 μs for $\underline{trans}$-$ReO_2L_4^z$ species in

aprotic solvents. Protons efficiently quench the luminescence of these molecules. Experiments directed toward photoinduced oxygen atom transfer chemistry are also described.

TABLE OF CONTENTS

List of Figures

List of Tables

CHAPTER ONE

Introduction

The mathematical separation of nuclear and electronic motions that arises from application of the Born-Oppenheimer (BO) approximation[1] to problems in molecular quantum mechanics leads to a ubiquitous chemical concept: the potential energy surface. The physical basis for the BO approximation lies in the large discrepancy between nuclear and electronic masses. If nuclear masses are, in fact, assumed infinite, the Hamiltonian operator for the molecular system reduces to the "electronic" Hamiltonian in which only the potential energy term depends on the nuclear coordinates. The eigenfunctions, $\psi(\underset{\sim}{r},\underset{\sim}{R})$ (where $\underset{\sim}{r}$ is the set of all electronic coordinates and $\underset{\sim}{R}$ is the set of all nuclear coordinates), and eigenvalues, $E(\underset{\sim}{R})$, of this "electronic" Hamiltonian, therefore, bear only parametric dependences on nuclear positions. The N-dimensional surfaces, $E(\underset{\sim}{R})$, then describe the potential energy of the molecular system for all configurations $\underset{\sim}{R}$.

The description of a chemical reaction as motion along an N-dimensional hypersurface is an especially important application of the potential energy surface concept. The N nuclear coordinates that describe a chemical transformation include the translational, rotational, and vibrational degrees of freedom of all species participating in the reaction. Clearly, it is not possible to solve exactly a dynamical problem of such complexity. The considerable utility of potential energy surfaces is, nevertheless, beautifully demonstrated by activated complex theory.[2] This formalism is based on the assumption of an (N-1)-dimensional hypersurface that separates products from reactants in the N-dimensional coordinate space of $E(\underset{\sim}{R})$. Whenever

the reactants, during their regular course of motion on $E(\underset{\sim}{R})$, cross the special (N-1)-dimensional hypersurface, products are formed. The set of nuclear configurations, $\underset{\sim}{S}$, that comprise this special (N-1)-dimensional hypersurface represent the activated complex. A pedagogical simplification of the potential energy hypersurface for a reacting system is the potential energy curve drawn along some generalized reaction coordinate (Figure 1.1).[3] In this case, N=1 and the (N-1)-dimensional activated complex "surface" is simply the point of intersection of the reactant and product potential curves, E_{gr} and E_p, respectively. Though Figure 1.1 is a crude simplification of the actual problem, it does provide a useful picture of the relationship between chemical reactivity and molecular potential energy surfaces.

Potential surfaces also describe photochemical reactions and illustrate some of the unique advantages that photochemistry holds over its thermal counterpart. Thermal processes involve motion only along E_{gr} and E_p in which all reactants and products are in ground electronic states (we will neglect thermal reactions that yield electronically excited products). The "electronic" Hamiltonian, however, has a nearly infinite set of eigenvalues, each corresponding to a unique surface $E_k(\underset{\sim}{R})$. A photochemical reaction, therefore, simply involves reactant motion on some surface E_{kr} $(k \neq g)$. Two important advantages of photochemical reactivity arise from the fact that $E_{kr} > E_{gr}$ for most values of $\underset{\sim}{R}$: (i) activation barriers to a reaction are usually lower and (ii) reactions that are endergonic from the ground state surface may be exergonic from the excited state surface. These aspects of photochemistry are illustrated in Figure 1.1. A third facet

Figure 1.1. Potential energy curves for thermal ($E_{gr} \rightarrow E_p$) and photochemical ($E_{kr} \rightarrow E_p$) reactions.

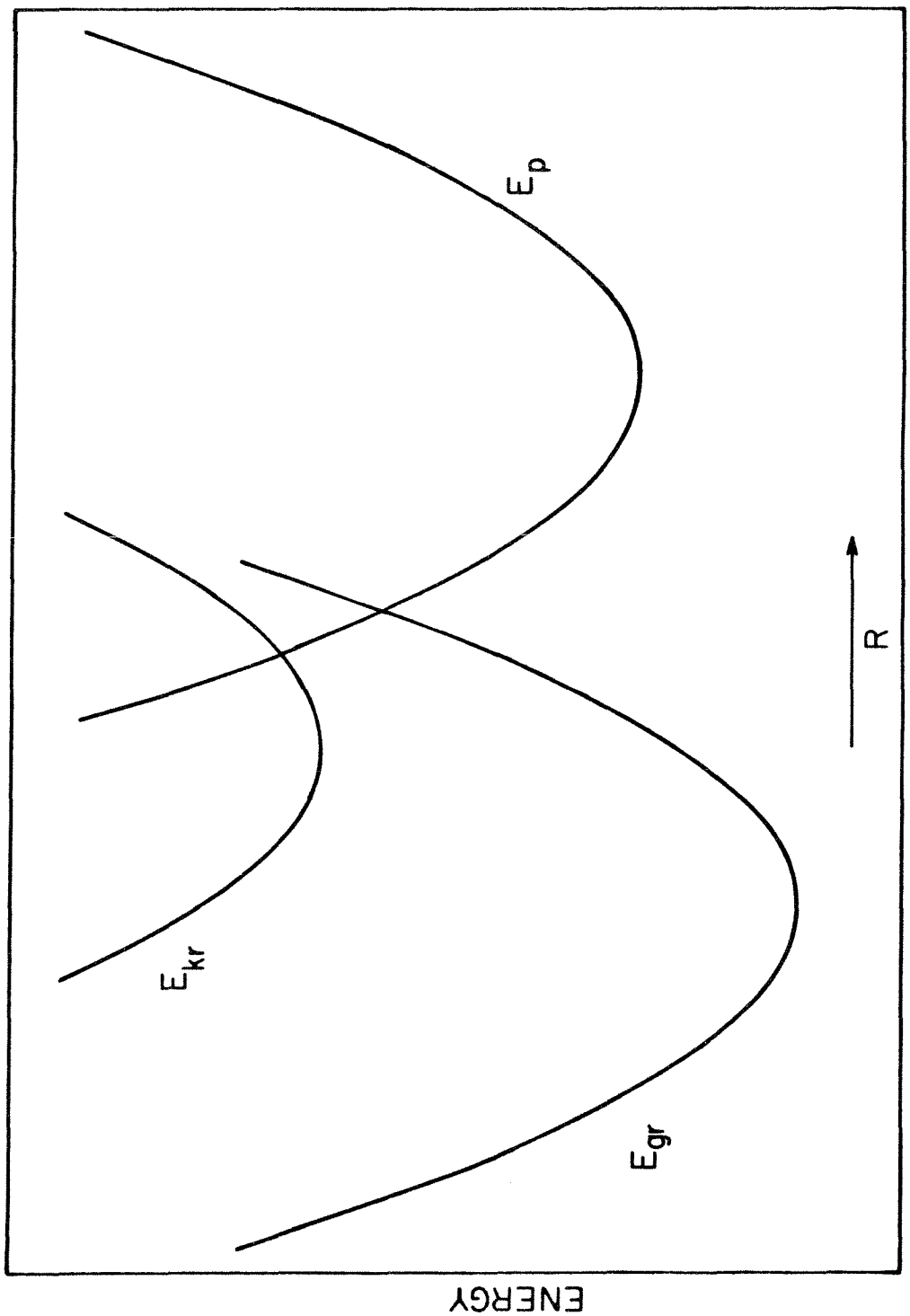
ENERGY
E_p
E_{kr}
E_{gr}
R

of photochemical reactivity that is related to point (i) above results from the displacement of the minimum of E_{kr} relative to E_{gr}. If the minimum on the E_{kr} surface is closer to the activated complex than that of E_{gr}, then the activation barrier will be reduced and the energy of the excited species will be specifically directed toward motion along the reaction coordinate.

In order to understand thermal and photochemical reactivity, the shapes and positions of potential surfaces must be determined. As mentioned above, this problem is far too complex to be solved theoretically but electronic spectroscopy provides a direct experimental probe of ground and excited state molecular potential energy surfaces. Polarized absorption and emission spectra of single crystals elucidate the symmetries of the wavefunctions involved in the transitions and vibrational fine structure maps the shapes and relative positions of their potential surfaces. The rates and mechanisms of excited state decay are particularly relevant to photochemistry and can be examined by time-resolved electronic spectroscopy. The combination of these techniques can provide a reasonably clear picture of molecular potential energy surfaces and the transitions between them.

The following chapters describe the spectroscopic determination of the potential surfaces in two types of transition metal-oxo complexes: (i) molybdenyl ions (Chapter Three) and (ii) dioxorhenium species (Chapter Four). Oxo complexes pervade the chemistry of metals in high oxidation states.[4] The large formal positive charges on the metal centers in these molecules and the Lewis basicity of the O^{2-} ion produce very short metal-oxygen multiple bonds.[5] Metal-oxo

compounds are commonly used as powerful oxidizing agents in inorganic and organic chemistry.[6] Many of these oxidations involve net oxygen atom transfers to the substrate (perhaps in conjunction with one or more proton transfers) though the mechanisms of these transformations are frequently rather complex. Direct oxygen atom transfer from a metal-oxo species to a substrate is an appealing mechanism that could lead to highly efficient and selective oxidation reactions. Photochemical induction of oxygen atom transfer could lead to even greater specificity than the thermal analog and, in the ideal situation, photochemical energy storage. The last section of Chapter Four describes attempts at photochemical oxygen atom transfer reactions based on the knowledge of excited state potential surfaces acquired from the spectroscopic studies of metal-oxo complexes.

CHAPTER TWO

Theory

A. The Adiabatic Born-Oppenheimer Approximation and the Franck-Condon Principle

The notions of electronic states and potential energy surfaces are, as mentioned in Chapter One, constructs of the adiabatic Born-Oppenheimer (ABO) approximation. Transitions between electronic states are governed by the Franck-Condon (FC) principle which, again, relies on the disparities in mass and velocity between electrons and nuclei. The formal development of the ABO approximation and FC principle are outlined in succeeding paragraphs leading to expressions which permit extraction of potential energy surfaces from spectroscopic data.

The Hamiltonian operator for a system of N nuclei and n electrons is (neglecting relativistic effects such as spin-orbit coupling)[7]

$$H = -\sum_{\alpha} \frac{\hbar^2}{2M_{\alpha}} \nabla_{\alpha}^2 - \sum_{i} \frac{\hbar^2}{2m_e} \nabla_i^2 - \sum_{\alpha,i} \frac{Z_{\alpha} e^2}{r_{ai}} + \sum_{\alpha<\beta} \frac{Z_{\alpha} Z_{\beta} e^2}{R_{\alpha\beta}} + \sum_{i<j} \frac{e^2}{r_{ij}} \tag{2.1}$$

where M_{α} is the mass of nucleus α, m_e is the electronic mass, $Z_{\alpha}e$ is the charge on nucleus α, $-e$ is the electronic charge, $r_{\alpha i}$, $R_{\alpha\beta}$, and r_{ij} are the distances between nucleus α and electron i, nuclei α and β, and electrons i and j, respectively, ∇_{α}^2 and ∇_i^2 are Laplacian operators for the coordinates of nucleus α and electron i, respectively, and $\hbar$ is Planck's constant divided by 2π. The first two terms of the Hamiltonian represent the kinetic energies of the nuclei ($\hat{T}_N$) and electrons ($\hat{T}_e$) while the final three terms correspond to the potential energy of the system $\{\hat{V}(\underset{\sim}{r}, \underset{\sim}{R})\}$. In the Born-Oppenheimer approximation the nuclear

masses are assumed infinite leaving the "electronic" Hamiltonian[8]

$$\hat{H} = \hat{T}_e + \hat{V}(\underset{\sim}{r}, \underset{\sim}{R}) \tag{2.2}$$

with eigenfunctions $\psi_k(\underset{\sim}{r}, \underset{\sim}{R})$ and eigenvalues $E_k(\underset{\sim}{R})$ that depend parametrically upon the nuclear coordinates $\underset{\sim}{R}$. If the functions $\psi_k(\underset{\sim}{r}, \underset{\sim}{R})$ form a complete set, eigenfunctions of the total Hamiltonian are given by[7]

$$\Psi_k(\underset{\sim}{r}, \underset{\sim}{R}) = \sum_i \chi_{ki}(\underset{\sim}{R})\, \psi_i(\underset{\sim}{r}, \underset{\sim}{R}). \tag{2.3}$$

In the adiabatic approximation the off-diagonal matrix elements of $\hat{H}$ in the basis $\chi_k(\underset{\sim}{R})\psi_k(\underset{\sim}{r}, \underset{\sim}{R})$ are ignored and the molecular wavefunction reduces to[7]

$$\Psi_k^{ABO} = \chi_k(\underset{\sim}{R})\, \psi_k(\underset{\sim}{r}, \underset{\sim}{R}). \tag{2.4}$$

Though these functions represent a tremendous simplification of the molecular problem, they still necessitate solution of the "electronic" Schrödinger equation at all values of $\underset{\sim}{R}$. Another approximation is frequently introduced to reduce the calculational complexity of the problem. In this "crude adiabatic approximation" the function $\psi_k(\underset{\sim}{r}, \underset{\sim}{R})$ is replaced by $\psi_k^0(\underset{\sim}{r}) = \psi_k(\underset{\sim}{r}, \underset{\sim}{R}_0)$ where R_0 is an equilibrium conformation of the molecule. In addition, the external coordinate system of the electrons, $\underset{\sim}{r}$, is generally transformed to an internal set (still denoted $\underset{\sim}{r}$) with only minor approximation.

In the ABO scheme the nuclear wavefunctions $\chi_k(\underset{\sim}{R})$ are solutions of the Schrödinger equation of motion for the nuclei in the potential field $E_k(\underset{\sim}{R})$. The solution of the nuclear problem is greatly facilitated

by two coordinate transformations. The first involves replacement of the external coordinates $\underset{\sim}{R}$ by a set of mass weighted internal coordinates $\underset{\sim}{S}$, where

$$S_i = \sqrt{M_\alpha}\,(R_{\alpha j} - R^0_{\alpha j}) \tag{2.5}$$

and $i = 1, 2, \ldots, 3N$, $j = x$, y, or z, and $R^0_{\alpha j}$ is the value of $R_{\alpha j}$ at some equilibrium position.[7] The potential function $E_k(\underset{\sim}{S})$ is then expanded in a Taylor series about the equilibrium configuration of state $\psi_k(\underset{\sim}{r}, \underset{\sim}{S})$,

$$E_k(\underset{\sim}{S}) = E^0_k + \sum_i \left[\frac{\partial E_k(S)}{\partial S}\right]_{S=0} S_i + \tfrac{1}{2} \sum_{i,j} \left[\frac{\partial^2 E_k(\underset{\sim}{S})}{\partial S_i \partial S_j}\right]_{S=0} S_i S_j + \cdots \tag{2.6}$$

The coefficients of the first order terms in this expansion are gradients of the potential evaluated at the equilibrium configuration $\underset{\sim}{S} = 0$. The gradient of the potential, however, is just the force acting on the nuclei but, since $\underset{\sim}{S} = 0$ was assumed to be an equilibrium configuration, this force is zero and these coefficients must vanish. If this series is truncated after the second order terms and a second coordinate transformation ($\underset{\sim}{S} \rightarrow \underset{\sim}{s}$) is performed that eliminates the cross terms $S_i S_j$ ($i \neq j$) in (2.6), then six of the coefficients of s_i^2 vanish (corresponding to three translational and three rotational degrees of freedom) and leave a Schrödinger equation for 3N-6 harmonic oscillators.[7] The total nuclear wavefunction $\chi_k(\underset{\sim}{s})$, then, is simply the product of 3N-6 single particle harmonic oscillator wavefunctions,

$$\chi^v_k(\underset{\sim}{s}_k) = \prod_{\mu=1}^{3N-6} \phi^{v_\mu}_{k\mu}(s_{k\mu}) \tag{2.7}$$

where v_μ is the quantum number of vibrational mode μ. The final molecular wavefunctions in the adiabatic Born-Oppenheimer approximation are

$$\Psi_k^{ABO}(\underset{\sim}{r}, \underset{\sim}{s}) = \{ \prod_{\mu=1}^{3N-6} \phi_{k_\mu}^{v_\mu}(s_{k_\mu}) \} \psi_k(\underset{\sim}{r}, \underset{\sim}{s}). \qquad (2.8)$$

Transitions between two electronic states Ψ_j and Ψ_k are governed by the Franck-Condon (FC) principle. In its classical form the FC principle imposes three restrictions on transitions between ABO surfaces: electronic motion is so fast that (i) the nuclei do not move during an electronic transition nor (ii) do their momenta change and (iii) that the oscillator (vibrating molecule) is at a classical turning point at the instant of the transition.[9] These restrictions then imply that transitions between surfaces must be vertical and must begin and end at classical turning points (i.e., on the potential surfaces). A quantum mechanical expression of the FC principle is provided by time dependent perturbation theory which demonstrates that the probability of electric dipole transitions between states Ψ_j and Ψ_k is proportional to $|P_{jk}|^2$ where P_{jk} is the matrix element[9]

$$P_{jk} = \langle \Psi_j(\underset{\sim}{r}, \underset{\sim}{R}) \,|\, P(\underset{\sim}{r}, \underset{\sim}{R}) \,|\, \Psi_k(\underset{\sim}{r}, \underset{\sim}{R}) \rangle \qquad (2.9)$$

and $P(\underset{\sim}{r}, \underset{\sim}{R})$ is the electric dipole operator

$$P(\underset{\sim}{r}, \underset{\sim}{R}) = -\sum_i e\, \underset{\sim}{r}_i + \sum_\alpha Z_\alpha\, e\, \underset{\sim}{R}_\alpha \qquad (2.10)$$

in which the vectors $\underset{\sim}{r}_i$ and $\underset{\sim}{R}_\alpha$ are parallel to the electric field vectors of the incident or emitted radiation. Using ABO wavefunctions, the

matrix element P_{jk} becomes

$$P_{jk} = \langle \chi_j(\underset{\sim}{R})\psi_j(\underset{\sim}{r},\underset{\sim}{R}) \left| -\sum_i e\,\underset{\sim}{r}_i \right| \chi_k(\underset{\sim}{R})\psi_k(\underset{\sim}{r},\underset{\sim}{R})\rangle$$
$$+ \langle \chi_j(\underset{\sim}{R})\psi_j(\underset{\sim}{r},\underset{\sim}{R}) \left| \sum_\alpha Z_\alpha\, e\,\underset{\sim}{R}_\alpha \right| \chi_k(\underset{\sim}{R})\psi_k(\underset{\sim}{r},\underset{\sim}{R})\rangle . \qquad (2.11)$$

Integrating over just the electronic coordinates yields

$$P_{jk} = \langle \chi_j(\underset{\sim}{R}) \left| D_{jk}(\underset{\sim}{R}) \right| \chi_k \underset{\sim}{R})\rangle + \langle \chi_j \underset{\sim}{R}) \left| \sum_\alpha Z_\alpha\, e\,\underset{\sim}{R}_\alpha \right| \chi_k(R)\rangle\, \delta_{jk} . \qquad (2.12)$$

The delta function in the second term arises from the orthonormality of the ABO wavefunctions and requires that this term correspond only to vibrational transitions within one electronic state. The first term in (2.12) relates to transitions between electronic states. In the Condon approximation,[9] $D_{jk}(\underset{\sim}{R})$ is assumed to be weakly dependent upon $\underset{\sim}{R}$ and is removed from the integral over the nuclear coordinates. The probability of the $\Psi_j^{v'} \rightarrow \Psi_k^{v''}$ transition (where v' and v'' are the sets of all vibrational quantum numbers in states Ψ_j and Ψ_k, respectively) in the harmonic ABO approximation is then proportional to

$$\left| P_{jk}^{v'v''} \right|^2 = \left| D_{jk}(\underset{\sim}{R}_0) \right|^2 \prod_{\mu=1}^{3N-6} \left| \langle \phi_{j\mu}^{v'_\mu}(s_{j\mu}) \left| \phi_{k\mu}^{v''_\mu}(s_{k\mu}) \right\rangle \right|^2 \qquad (2.13)$$

where Duschinky effects[10] and off-diagonal coupling between modes have been neglected in the vibrational overlap integrals. The matrix element $D_{jk}(\underset{\sim}{R}_0)$ is the electronic transition dipole moment and the squares of the vibrational overlap integrals are known as Franck-Condon factors.

Group theory proves to be of considerable utility in the determination of selection rules for molecular electronic transitions. In order that the transition matrix element not vanish, the function

$$\{\Psi_j(\underset{\sim}{r},\underset{\sim}{R})\}\{\sum_i -e\,\underset{\sim}{r}_i\}\{\Psi_k(\underset{\sim}{r},\underset{\sim}{R})\} \tag{2.14}$$

must transform as the totally symmetric irreducible representation of the highest symmetry point group common to both states Ψ_j and Ψ_k.[7] The direct product $\Gamma_j \times \Gamma_k$ (where Γ_i is the irreducible representation according to which the function Ψ_i transforms) must, therefore, contain the representation $\Gamma_{\underset{\sim}{r}}$. In point groups of high (cubic) symmetry the dipole moment operator, $-\sum_i e\,\underset{\sim}{r}_i$, transforms as a threefold degenerate representation such that all polarization directions are equivalent. This degeneracy is reduced in point groups of lower symmetry, however, producing $\Psi_j \rightarrow \Psi_k$ transitions induced by light of specific polarization.

Within the level of approximation defined above, the electronic transition dipole moment is independent of the extent of vibrational excitation in states Ψ_j and Ψ_k. The relative intensities of the individual vibronic transitions $\Psi_j^{v'} \rightarrow \Psi_k^{v''}$ will be governed by the relative magnitudes of the Franck-Condon factors. Symmetry arguments can also be applied to the evaluation of vibrational overlap integrals. If the molecule in the electronic states Ψ_j^0 and Ψ_k^0 belongs to the same point group, then distortions between them can occur only along totally symmetric normal coordinates. The repeated product of FC factors in (2.13), therefore, can be greatly simplified. For all normal

coordinates along which there is no distortion between states Ψ_j and Ψ_k, the orthogonality of harmonic oscillator wavefunctions requires that the only non-zero FC factors be those in which the vibrational quantum numbers of $\phi_{j\mu}^{v'\mu}(s_{j\mu})$ and $\phi_{k\mu}^{v''\mu}(s_{k\mu})$ are identical.[11] If the initial state $\Psi_j^{v'}$ is vibrationally unexcited then so must be all modes of state $\Psi_k^{v''}$ that are not distorted relative to state $\Psi_j^{v'}$. The orthonormality of harmonic oscillator eigenfunctions is lost, however, when the functions have different origins. In this instance several FC factors of a given normal coordinate can be non-zero and will lead to progressions in the electronic spectrum in totally symmetric vibrational modes. Harmonic FC factors with displaced nuclear coordinates and disparate force constants have been well studied and can be expressed in terms of recursion relations that depend upon three parameters: the vibrational frequencies of the mode in states Ψ_j and Ψ_k and the magnitude of the displacement along this normal coordinate.[12] These formulae and their application are described in Appendix 1.

The vibrational frequencies of the distorting mode are direct spectroscopic observables so that only the magnitude of the distortion need be calculated from the spectra. The exact expressions for emission and absorption intensities of a specific vibronic transition are[13]

$$I_{em}^{v'v''} = \frac{64}{3}\frac{\pi^4 C}{h^4} N_{v'} \tilde{\nu}_{v'v''}^3 \left| P_{jk}^{v'v''} \right|^2 \qquad (2.15a)$$

$$I_{abs}^{v'v''} = \frac{8}{3}\frac{\pi^3}{h^2 c} I_0 \Delta x N_{v''} \tilde{\nu}_{v'v''} \left| P_{jk}^{v'v''} \right|^2 \qquad (2.15b)$$

where $N_{v'}$ and $N_{v''}$ are the populations of the initial states, I_0 is the intensity of the incident radiation in absorption, Δx is the path length in absorption, and $\tilde{\nu}_{v'v''}$ is the wavenumber of the $\Psi_j^{v'} \leftarrow \Psi_k^{v''}$ transition. The emission intensity is given in terms of emitted photons per second while the absorption intensity, in the case of weakly absorbing samples, is roughly proportional to the integrated absorbance of the vibronic band.[13] Absolute intensities are frequently difficult to measure but the relative intensities of vibronic bands provide all of the information necessary in the calculation of excited state distortions (Appendix 1). In order to reduce spectral congestion and line broadening, spectra are normally recorded at cryogenic temperatures so that the initial electronic state is vibrationally unexcited. The relative intensities of vibronic bands then take the form[14]

$$\left[\frac{I_{em}^{0v''_n}}{I_{\ell m}^{0v''_n}}\right] = \left[\frac{\tilde{\nu}_{0v''_n}}{\tilde{\nu}_{0v''_m}}\right]^3 \left[\frac{\langle \chi_j^0(\underset{\sim}{s}_j) | \chi_k^{v''_n}(\underset{\sim}{s}_k)\rangle}{\langle \chi_j^0(\underset{\sim}{s}_j) | \chi_k^{v''_m}(\underset{\sim}{s}_k)\rangle}\right]^2 \qquad (2.16a)$$

$$\left[\frac{I_{abs}^{v'_n 0}}{I_{abs}^{v'_m 0}}\right] = \left[\frac{\tilde{\nu}_{v'_n 0}}{\tilde{\nu}_{v'_m 0}}\right] \left[\frac{\langle \chi_j^{v'_n}(\underset{\sim}{s}_j) | \chi_k^0(\underset{\sim}{s}_k)\rangle}{\langle \chi_j^{v'_m}(\underset{\sim}{s}_j) | \chi_k^0(\underset{\sim}{s}_k)\rangle}\right]^2 . \qquad (2.16b)$$

The entire theory of Franck-Condon transitions between adiabatic Born-Oppenheimer potential surfaces is summarized in Figure 2.1. The left half of the diagram contains the potential surfaces for states Ψ_j and Ψ_k and the righthand portion illustrates the spectra that would arise from transitions between them at low temperature. This figure also illustrates the connection between the classical and quantum

Figure 2.1. Schematic representation of Franck-Condon transitions between adiabatic Born-Oppenheimer potential surfaces. The spectra resulting from these transitions appear in the righthand portion of the diagram.

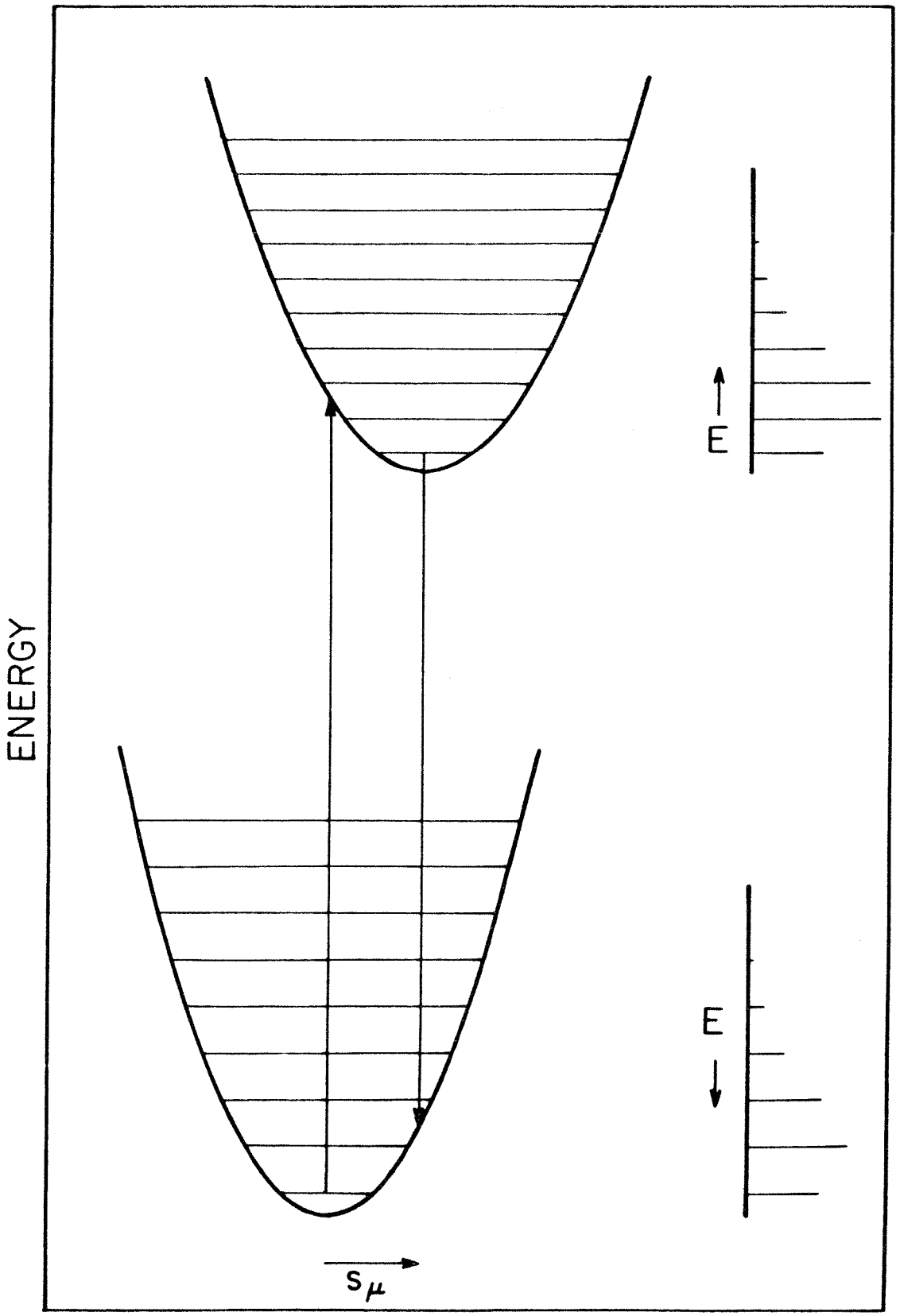
ENERGY
E
E
s_μ

mechanical FC principles. The vertical arrows represent the most probable transitions since nuclear positions and momenta are not changing (classical FC) and also correspond to regions of maximum overlap of the vibrational wavefunctions in the two states (quantum mechanical FC). It is also clear from the figure that the larger the distortion along the normal coordinate s_μ the higher will be the vibrational quantum number of the most intense vibronic transition. Given sufficiently resolved vibrational fine structure in molecular electronic absorption and emission spectra, Franck-Condon analyses can yield an accurate representation of molecular potential energy surfaces.

B. The Decay of Electronic Excited States

Excited molecules are metastable species that can decay by four distinct pathways: luminescence; energy transfer; intramolecular non-radiative decay; and photochemistry. The final pathway is, of course, the most chemically interesting, however, all four processes are inter-related and can operate simultaneously in a given molecule. These four routes are often governed by first order or pseudo-first order kinetics resulting in exponential decay of the excited molecule, M^*. The overall rate constant, k, for the decay of M^* is then given by

$$k = \frac{1}{\tau} = k_r + k_{ET} + k_{nr} + k_p \qquad (2.17)$$

where k_r, k_{ET}, k_{nr}, and k_p are rates of luminescence, energy transfer, intramolecular non-radiative decay, and photochemical reactions,

respectively, and τ is defined as the excited state lifetime.

The rate of luminescence is determined by the intensity of the electronic transition and can be approximated from the absorption spectrum by the Strickler-Berg formula[15]

$$k_r = (2.880 \times 10^{-9})\, n^2 \langle \tilde{\nu}_f^{-3} \rangle_{Av}^{-1} \frac{g_l}{g_u} \int \epsilon \, d \ell n \tilde{\nu} \qquad (21.8)$$

where n is the index of refraction of the medium in which the chromophore is embedded, $\langle \tilde{\nu}_f^{-3} \rangle^{-1}$ is the reciprocal of the mean value of $\tilde{\nu}^{-3}$ in the fluorescence spectrum, g_l and g_u are the degeneracies of the lower and upper states, respectively, and ϵ is the absorption coefficient for the $u \leftarrow l$ transition.

Förster[16] and Dexter[17] have presented theories of energy transfer quenching of electronic excited states but no such work will be related in the following chapters and a discussion of the theory will be forgone.

The past twenty years has been a period of considerable interest in the mechanisms of intramolecular non-radiative decay processes in polyatomic molecules.[18] This phenomenon results from the breakdown of the adiabatic Born-Oppenheimer approximation, that is, from intramolecular vibronic coupling of the zero-order vibronic states in a polyatomic molecule. Bixon and Jortner[19] classify molecules according to four categories of non-radiative decay. Their statistical limit is characterized by a high density of vibronic states wherein the average vibronic coupling matrix elements between states are considerably greater than the mean energy spacing between states. The three other

cases involve more coarsely spaced vibronic levels as are found in small di- and triatomic molecules and are not applicable to the metal complexes discussed in Chapters Three and Four.

The simplest model of radiationless decay in the statistical limit is depicted schematically in Figure 2.2.[18b] The states Ψ_0, Ψ_s, and $\{\Psi_n\}$ are ABO wavefunctions representing, respectively, the ground electronic state, the initially prepared excited state, and a dense manifold of vibronic levels corresponding to an electronic state lower in energy than Ψ_s. The energy difference, ΔE, between states $\Psi_s^{v=0}$ and $\Psi_n^{v=0}$ is the energy gap for the $\Psi_s \rightarrow \Psi_n$ transition. The off-diagonal matrix elements of the nuclear kinetic energy operator, V_{sn}, that were ignored in the adiabatic approximation now serve to couple Ψ_s to states in the manifold $\{\Psi_n\}$. The non-radiative decay of Ψ_s into $\{\Psi_n\}$ is then governed by the "golden rule" transition rate[18b] where

$$k_{nr}(s \rightarrow n) = \frac{2\pi}{\hbar} \sum_{i,j} p(si) \left| \langle \Psi_{si} | V | \Psi_{nj} \rangle \right|^2 \delta (E_{si} - E_{nj}) \qquad (2.19)$$

$p(si)$ is the Boltzmann averaged probability of populating the i^{th} vibronic level of Ψ_s, $\langle \Psi_{si} | V | \Psi_{nj} \rangle \equiv V_{si,nj}$ is the non-adiabatic matrix element of the nuclear kinetic energy operator, and $\delta(E_{si} - E_{nj})$ is a delta function to ensure energy conservation. Clearly, the most important and difficult parts of this expression are the matrix elements, $V_{si,nj}$, but, with the application of some reasonable approximations, they can be recast into a more physically transparent form.

The nuclear parts of the ABO wavefunctions are, as before, assumed to be comprised of 3N-6 uncoupled harmonic oscillators and

Figure 2.2. Schematic representation of the non-adiabatic coupling process that leads to intramolecular non-radiative electronic relaxation. The adiabatic Born-Oppenheimer states Ψ_0, Ψ_s, and $\{\Psi_n\}$ are, respectively, the ground electronic state, initially prepared electronic excited state, and a manifold of vibronic levels of state n ($E_n < E_s$). States Ψ_0 and Ψ_s are connected by the transition moment μ_{sn} but no other radiative transitions are allowed. V_{sn} is the matrix element coupling Ψ_s to $\{\Psi_n\}$ and ΔE is the energy gap between the two states (reference 18b).

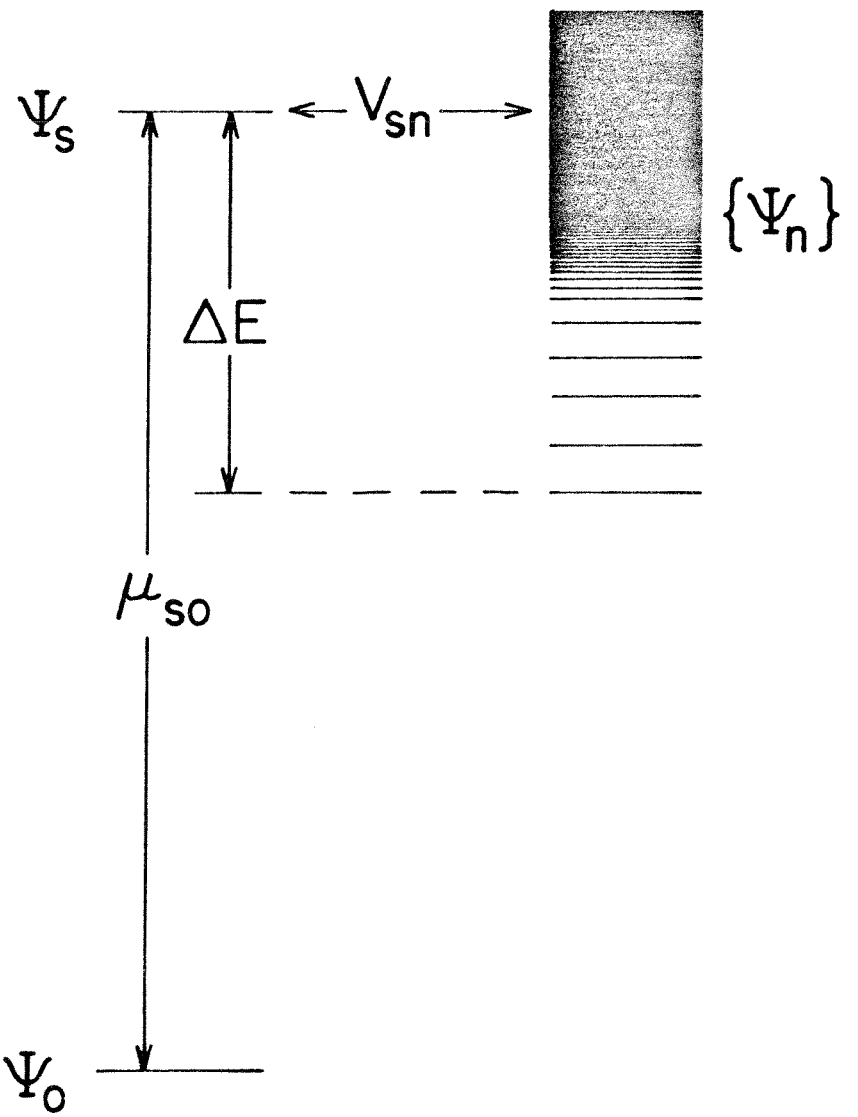
Ψ_s
V_{sn}
$\{\Psi_n\}$
ΔE
μ_{so}
Ψ_o

that the modes are parallel in states Ψ_s and Ψ_n but may be displaced and have different force constants. The coupling operator is generally given the form[18b]

$$V_{sn}(\underset{\sim}{s}) = \sum_{\mu=1}^{3N-6} C_{sn}^{\mu} i\hbar \frac{\partial}{\partial s_{n\mu}} \tag{2.20}$$

which arises from the lowest order off-diagonal matrix element of the nuclear kinetic energy operator. The matrix element C_{sn}^{μ} is an integral over just the electronic coordinates, viz.

$$C_{sn}^{\mu}(\underset{\sim}{s}) = \hbar \langle \Psi_s(\underset{\sim}{r}, \underset{\sim}{s}) \left| \frac{i\partial}{\partial s_{n\mu}} \right| \Psi_n(\underset{\sim}{r}, \underset{\sim}{s}) \rangle \tag{2.21}$$

and is often assumed to be a slowly varying function of $\underset{\sim}{s}$ such that an equilibrium value, $C_{sn}^{\mu}(\underset{\sim}{s}^0)$, is chosen to permit its removal from integrals over nuclear coordinates in $V_{si,nj}$. Finally, it is commonly assumed that only one mode, μ, is active in promoting the $\Psi_s \rightarrow \Psi_n$ transition which reduces the sum in (2.20) to a single term. The generating function method of Kubo and Toyazawa[20] can then be used to evaluate $V_{si,nj}$. The resultant probability for the $\Psi_s \rightarrow \Psi_n$ transition is the Fourier transform of a product of generating functions[18b]

$$k_{nr}(s \rightarrow n) = \hbar^{-2} \int_{-\infty}^{+\infty} f(t) \exp(-i\Delta E t/\hbar) dt \tag{2.22}$$

where

$$f(t) = \left| C_{sn}^{\mu} \right|^2 \tilde{f}_{\mu}(t) \prod_{\nu \neq \mu}^{3N-7} f_{\nu}(t) \, . \tag{2.23}$$

The functions $f_\nu(t)$ are single mode generating functions for optical absorption and $\tilde{f}_\mu(t)$ is the single mode generating function for the nuclear momentum operator in the mode $s_{n\mu}$. The explicit forms of these functions are known so that calculation of non-radiative decay rates involves only the evaluation of some definite integrals. A common simplifying assumption that vibrational force constants are the same in states Ψ_s and Ψ_n and that normal modes (except the promoting mode μ) are only linearly displaced permits expression of $k_{nr}(s \rightarrow n)$ in the form[18b]

$$k_{nr}(s \rightarrow n) = \left|C_{sn}^{\mu}\right|^2 (\omega_\mu/4\hbar) \exp(-G)$$

$$\times\{(\coth y_\mu + 1) \int_{-\infty}^{+\infty} \exp\left[+i\left(\frac{\Delta E}{\hbar} - \omega_\mu\right)t + G_+(t) + G_-(t)\right] dt$$

$$+(\coth y_\mu - 1) \int_{-\infty}^{+\infty} \exp\left[-i\left(\frac{\Delta E}{\hbar} + \omega_\mu\right)t + G_+(t) + G_-(t)\right] dt\} \tag{2.24}$$

where

$$y_\mu \equiv \frac{\hbar\omega_\mu}{2k_B T} , \tag{2.25}$$

$$G_+(t) = \sum_{\nu=1}^{3N-7} X_\nu (\bar{n}_\nu + 1) \exp(i\omega_\nu t) , \tag{2.26a}$$

$$G_-(t) = \sum_{\nu=1}^{3N-7} X_\nu \bar{n}_\nu \exp(-i\omega_\nu t) , \tag{2.26b}$$

$$\bar{n}_\nu = \left[\exp\left(\frac{\hbar\omega_\nu}{k_B T}\right) - 1\right]^{-1} , \tag{2.27}$$

$$G = G_{+}(t=0) + G_{-}(t=0) \ , \tag{2.28}$$

and

$$X_{\nu} = \tfrac{1}{2} \frac{\omega_{\nu}}{\hbar} (s^{0}_{n\nu} - s^{0}_{s\nu})^{2} \tag{2.29}$$

in which $(s^{0}_{n\nu} - s^{0}_{s\nu})$ is the difference in equilibrium positions for mode ν in states Ψ_s and Ψ_n. Various limiting behaviors result from (2.24) depending upon the magnitudes of X_{ν} and T and they will be discussed as the need arises in the following chapters. It is not a coincidence that the parameters in (2.24) are just those germane to electronic spectroscopy since both theoretical formalisms involve Franck-Condon transitions between potential energy surfaces. The uncertainties in these parameters, however, coupled with the breakdown of the single promoting mode, parallel harmonic oscillator approximations result in rather large errors in calculations of absolute molecular non-radiative decay rates.[18b] Even though it is constrained by several approximations, equation (2.24) does offer some physical insight into the non-radiative decay processes in excited metal-oxo complexes.

CHAPTER THREE

Molybdenyl Ions

A. Introduction

The molybdenyl ions are the second row, group VI representatives of a set of formally $\underline{d}^1$ metal mono-oxo complexes, MO^{n+} (M = V, n = 2; M = Cr, Mo, W, n = 3).[21] These species can be either five coordinate, forming a square pyramid with oxygen at the apex, four basal ligands, and the metal positioned slightly above the basal plane, or six coordinate by adding a weakly bound ligand trans to the oxo group yielding a tetragonally distorted octahedron. The ligands are generally anionic (i.e., halides or conjugate bases of strong acids), though complexes with some neutral ligands have been prepared.[21c] The electronic spectra and structures of the vanadyl, chromyl, and molybdenyl ions were discussed by Ballhausen, Gray, and Hare[22,23] over twenty years ago in terms of a simple molecular orbital diagram. Although countless subsequent studies have been performed, differences of opinion still surface over the interpretation of the electronic absorption spectra of many of these complexes. This chapter contains a discussion and assignment of the electronic absorption spectra of some molybdenyl ions as well as an examination of the luminescence properties of $MoOCl_4^-$.

B. Materials and Methods

Miscellaneous Procedures: Reagent grade solvents were used throughout unless otherwise specified. Burdick and Jackson brand dichloromethane was degassed with five freeze-pump-thaw cycles on a high vacuum line ($< 10^{-3}$ torr) and stored under vacuum over activated (heating under vacuum for 12 hrs.) Linde type 4A molecular sieves.

When needed, this solvent was transferred under vacuum by flask to flask distillation and further degassed with three freeze-pump-thaw cycles. These and all other anaerobic manipulations were performed on an all glass vacuum line equipped with an Edwards 2 inch oil vapor diffusion pump. Analytical grade Dowex AG-50W-X2 cation exchange resin was washed with 6M hydrochloric acid (HCl) then equilibrated with 0.1M HCl prior to use.

$MoO(H_2PO_4)_4^-$ and $MoO(HSO_4)_4^-$: These complexes were prepared by acidification of $Mo_2O_4^{2+}{}_{(aq)}$ solutions[24] rather than by the published route.[25] A solution of $(NH_4)_6[Mo_7O_{24}]\cdot 4H_2O$ in 3M HCl (1.8g/100 ml) was reduced with elemental mercury to yield an orange solution which was decanted from the mercury, filtered, concentrated by rotary evaporation to a third of the original volume, diluted by a factor of 100, and adsorbed atop a Dowex AG-50W-X2 cation exchange column. The column was rinsed with 0.1M H_2SO_4 or 0.1M H_3PO_4 until no chloride ion (by Ag^+ test) was present in the eluate then eluted with 1M H_2SO_4 or H_3PO_4. These eluates were diluted with concentrated H_2SO_4 or H_3PO_4 to yield 10^{-2} M Mo(V) solutions in 17 M H_2SO_4 or 13 M H_3PO_4. Molybdenum concentrations were determined by Ce(IV) titrations.

$(Ph_4As)MoOCl_4$: A solution containing 10g of $(NH_4)_6[Mo_7O_{24}]\cdot 4H_2O$ and 8g of hydrazine sulfate in 50 ml of concentrated HCl was heated for ca. 1 hour at ca. 80°C until it was a deep green color. Solid (PhAs)Cl·HCl was added and digested just below the boiling point of the solution for about 2 hours. Upon cooling overnight, a green solid precipitated which was filtered and washed with cold concentrated HCl

then anhydrous diethyl ether. The solid was dried by heating (110°C) under vacuum ($< 10^{-3}$ torr) for 8 hours, dissolved in dry CH_2Cl_2, and filtered under vacuum through a medium porosity frit. The solution was evaporated slowly under an Ar gas flow and produced large green rectangular prismatic crystals. Examination under a polarizing microscope confirmed that the crystals were axial, in accord with the published crystal structure of this compound.[26]

$(Ph_4As)MoOBr_4$: This compound was prepared analogously to the method of Bino and Cotton.[27] $Mo_2(O_2CCH_3)_4$, prepared by the literature method,[28] was dissolved in 8 M hydrobromic acid (220 mg/50 ml) and heated gently (ca. 50°C), with stirring, for 2 hours. Solid $(Ph_4As)Cl \cdot HCl$ was added and stirring was continued overnight during which time a yellow solid precipitated which was collected by filtration, washed with a small amount of cold water, and air dried. The solid was heated at 50°C under vacuum ($< 10^{-3}$ torr) for 3 days, then dissolved in dry CH_2Cl_2 and filtered. The solution was evaporated slowly under an Ar gas flow to yield red-brown crystals.

Absorption Spectra: Electronic absorption spectra were recorded on a Cary model 17 spectrophotometer. Low temperatures were achieved with either a CTI model 21 cryocooler (300-30 K) or an Andonian Associates liquid helium (LHe) dewar system (77-4.5 K). Temperatures in the cryocooler were measured with a chromel/Au:Fe thermocouple and the temperature could be varied with a small resistive heater. The temperature at the sample in the LHe dewar was monitored with a calibrated glassy carbon resistor mounted in a brass block in thermal contact with the sample. The temperature could be

adjusted with a resistive heater that warmed the He gas before it passed over the sample. Polarized spectra were recorded along crystal extinction directions using a pair of Glan-Thompson calcite polarizers. Extinction directions were determined spectrophotometrically by rotating polarizers to absorption maxima and minima. Single crystals for absorption spectra were mounted on fused silica disks and masked with "copper grease" (a mixture of fine copper powder and Apiezon H grease). Crystals were polished in order to achieve the desired thickness. In this procedure, crystals were placed on a fused silica disk and embedded in molten phenyl salicylate. Upon solidification of the phenyl salicylate, the mass was polished by hand using first 5 micron then 0.3 micron alumina on paper as abrasives. Phenyl salicylate was removed by washing with diethyl ether. Crystal faces were determined by examination under a polarizing microscope or by X-ray photography.

Luminescence Spectra: Luminescence spectra were recorded on an instrument constructed by Steven F. Rice at Caltech. Light from a 200 W Hg/Xe arc lamp was wavelength selected by a Spex Minimate 0.25 meter monochromator equipped with a set of fixed slits, modulated with a beam chopper, collimated, filtered with an interference or Corning glass filter, and focused onto the sample. Emitted light from solid or solution samples at room temperature or in the cryocooler was collected at a right angle to the excitation beam path. Light emitted from samples in the LHe dewar was either collected off the front (excitation) surface or was deflected into the collection optics following transmission through a crystalline sample. Regardless of

orientation, the emitted light was filtered from the excitation beam with a Corning glass filter, collimated, and focused onto the entrance slit of a Spex model 1870 0.5 meter monochromator. The slit width of this monochromator could be continuously varied from zero to ten millimeters with a precision of ±10 microns. The detector was either a Hamamatsu model R955 or R406 (red sensitive) photomultiplier tube. The signal from the photomultiplier was amplified with a Princeton Applied Research (PAR) model 181 current sensitive preamplifier and input to a PAR model 186A lock-in amplifier phased with the excitation beam chopper. Spectra were transcribed on a strip chart recorder running synchronously with the emission monochromator scan drive. The spectrometer response was determined using a calibrated tungsten filament lamp and spectra were corrected for this response by the method of Drushel, Sommers, and Cox.[29] Solid samples were single crystals or polycrystalline arrays mounted on fused silica disks with Dow Corning high vacuum silicone grease. Solution samples were prepared under vacuum in an 10 ml roundbottom flask equipped with a sidearm 1 cm fluorescence cuvette.

Luminescence Lifetimes: Luminescence lifetimes were measured using a Quanta Ray DCR Nd:YAG laser with a pulse duration of 8 ns (fwhm). The 1064 nm fundamental line was frequency doubled or tripled with a harmonic generator to provide, respectively, up to 75 mJ per pulse at 532 nm or 35 mJ per pulse at 355 nm. Luminescence from the sample was collimated and focused through a Corning glass filter (to remove scattered laser light) onto the entrance slit of a MacPherson model 270 0.35 meter monochromator. The signal

from either a Hamamatsu R928 or R406 (red sensitive) photomultiplier tube was enhanced with a LeCroy model VV101ATB fast response amplifier and passed on to the 50 ohm impedance input of a Biomation model 6500 waveform recorder. The laser and data collection systems were controlled by a Digital PDP 11/03 computer, the software for which was designed by Leslie G. Butler at Caltech, to permit signal averaging and curve fitting to single exponential decays. Luminescence from solid and solution samples was collected at a right angle to the excitation beam. Variable temperature experiments between 300 and 80 K were performed with a glass dewar through which flowed nitrogen gas that had been cooled by passage through a copper coil immersed in a dewar of liquid nitrogen. Temperatures between 80 and 4.5 K were achieved with the above mentioned LHe dewar. The 180° disposition of windows in both of these dewars required that the emitted light be collected off the front (excited) surface of the sample then deflected by mirrors to the MacPherson monochromator. The laser flashlamp energy was generally set below its maximum value with solid samples since higher laser powers led to non-exponential decays.

Electron Paramagnetic Resonance spectra: EPR spectra were recorded on a Varian E-Line Century Series spectrometer. Samples in quartz tubes were immersed in liquid nitrogen in a quartz "finger" dewar for spectra at 77K. Spectra in concentrated sulfuric and phosphoric acids could only be run at low temperature because the high values of the room temperature dielectric constants of these solvents prevented tuning of the EPR cavity.

C. Results

The EPR spectra of molybdenum(V) in concentrated H_2SO_4 and H_3PO_4 at 77K are shown in Figure 3.1. These spectra are indicative of axial doublet spin systems coupled to nuclei of spin I = 0 and I = 5/2.[30] The g values and molybdenum hyperfine coupling constants are in agreement with those previously reported[25] and are similar to those of other molybdenyl ions (Table 3.1).[31]

The electronic absorption spectra of molybdenum(V) in concentrated HX ($X = Cl^-$, HSO_4^-, $H_2PO_4^-$) solution are shown in Figure 3.2. The spectra are characterized by two weak bands below 30,000 cm^{-1}. The lower energy of the two maximizes near 14,000 cm^{-1} ($\epsilon \sim 20\ M^{-1}\ cm^{-1}$) and its position is essentially independent of the nature of X. The higher energy band is more solvent dependent, maximizing at 22,500 cm^{-1} ($\epsilon = 14\ M^{-1}\ cm^{-1}$) in HCl and at 26,000 cm^{-1} ($\epsilon = 15\ M^{-1}\ cm^{-1}$) in H_2SO_4 and H_3PO_4. More intense absorption appears at higher energy with discrete bands resolving at 28,000 cm^{-1} ($\epsilon \sim 500\ M^{-1}\ cm^{-1}$), 32,500 cm^{-1} ($\epsilon \sim 3,800\ M^{-1}\ cm^{-1}$), and 42,000 cm^{-1} ($\epsilon \sim 5,000\ M^{-1}\ cm^{-1}$) for Mo(V) in HCl though only a rising absorption background for Mo(V) in H_2SO_4 and H_3PO_4.

In some instances molybdenyl ions can be isolated from solution as crystalline solids. $(Ph_4As)MoOCl_4$, for example, crystallizes in the tetragonal space group $P_{4/n}$ in which each anion has C_{4V} symmetry[26] and, as such, is ideally suited for polarized spectroscopy. The σ, π, and axial electronic absorption spectra recorded at room temperature and 5K are shown in Figures 3.3 and 3.4. The two absorption features below 25,000 cm^{-1} are predominantly σ polarized and the similarity

Figure 3.1. EPR spectra of Mo(V) in (a) 17 M H_2SO_4 and (b) 13 M H_3PO_4.

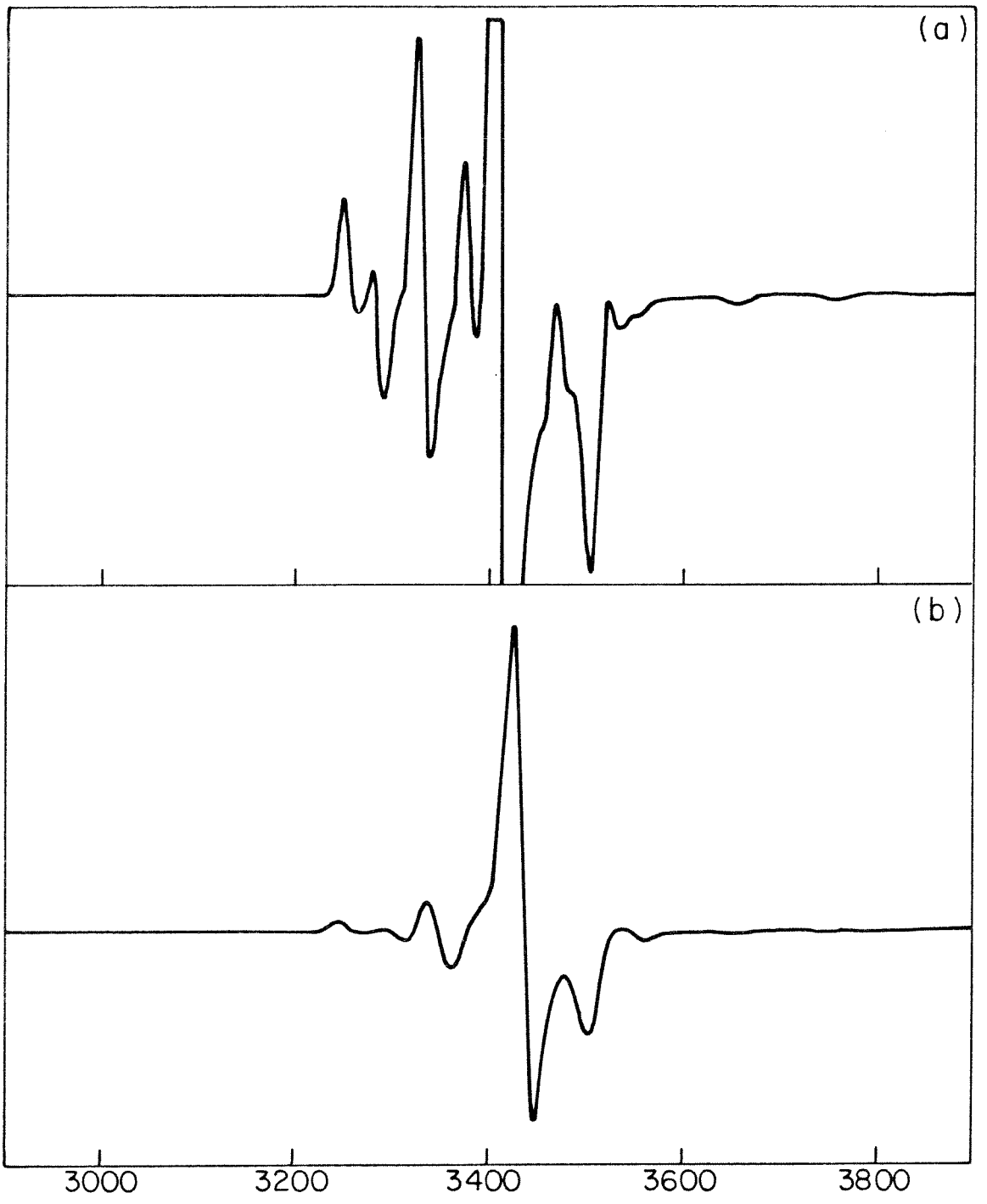
(a)
(b)
3000
3200
3400
3600
3800
H, Gauss

Table 3.1. EPR parameters of molybdenyl ions.

Complex	$g_{\|\|}$	$g_{\perp}$	A^a	B^a	ref.
Mo(V) in 17 M H_2SO_4	1.889	1.941	94	43	--
Mo(V) in 13 M H_3PO_4	1.892	1.927	88	38	--
$MoOF_5^{2-}$	1.874	1.911	92.93	45.13	31b
$MoOCl_5^{2-}$	1.970	1.938	74.6	30.5	31a,b
$MoOBr_5^{2-}$	2.090	1.945	66.0	30	31a

a. In units of 10^{-4} cm^{-1}.

Figure 3.2. Electronic absorption spectra of Mo(V) in (a) 12 M HCl, (b) 17 M H_2SO_4, and (c) 13 M H_3PO_4.

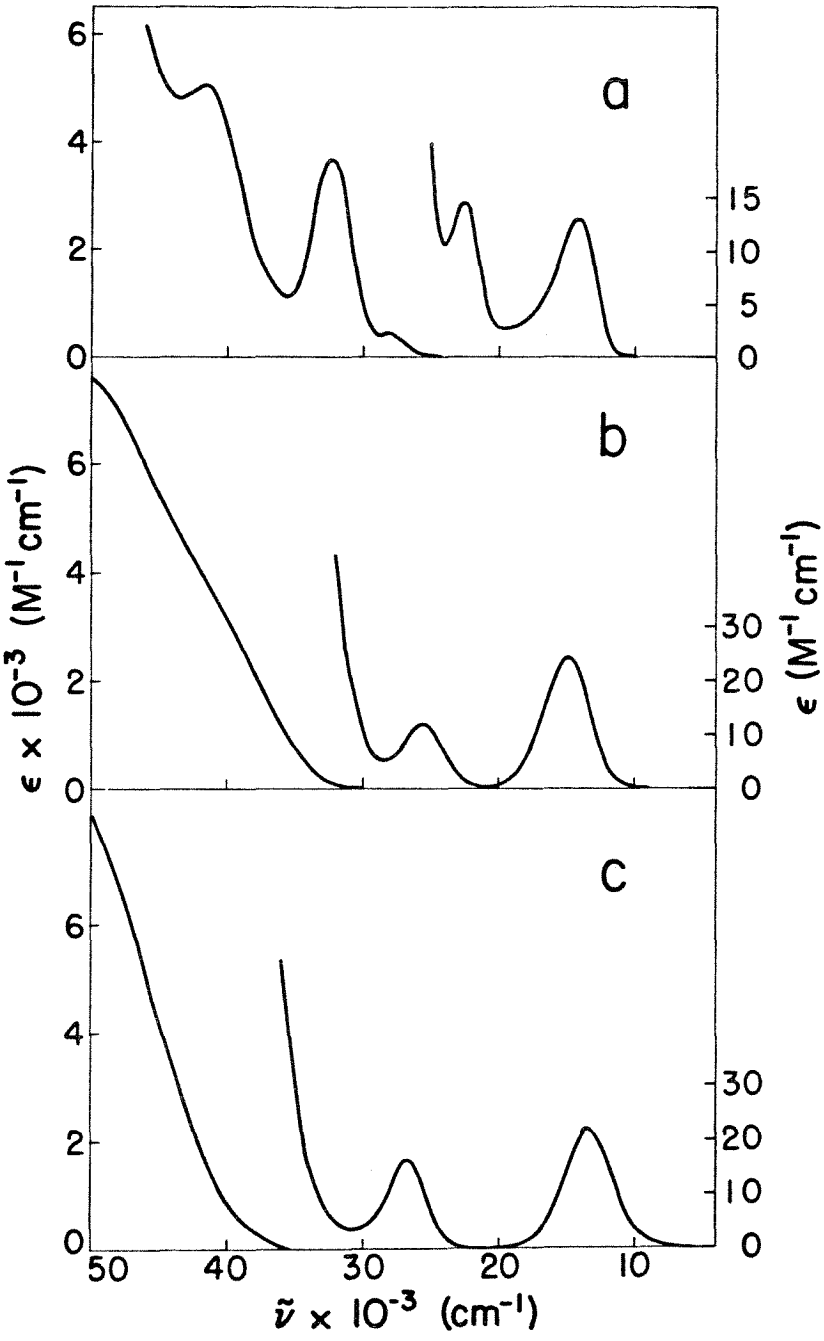
a
b
c
6
4
2
0
15
10
5
0
30
20
10
0
50
40
30
20
10
ε x 10⁻³ (M⁻¹cm⁻¹)
ε (M⁻¹cm⁻¹)
ν̃ x 10⁻³ (cm⁻¹)

Figure 3.3. Single crystal polarized electronic absorption spectra of $(Ph_4As)MoOCl_4$ at ambient temperature.

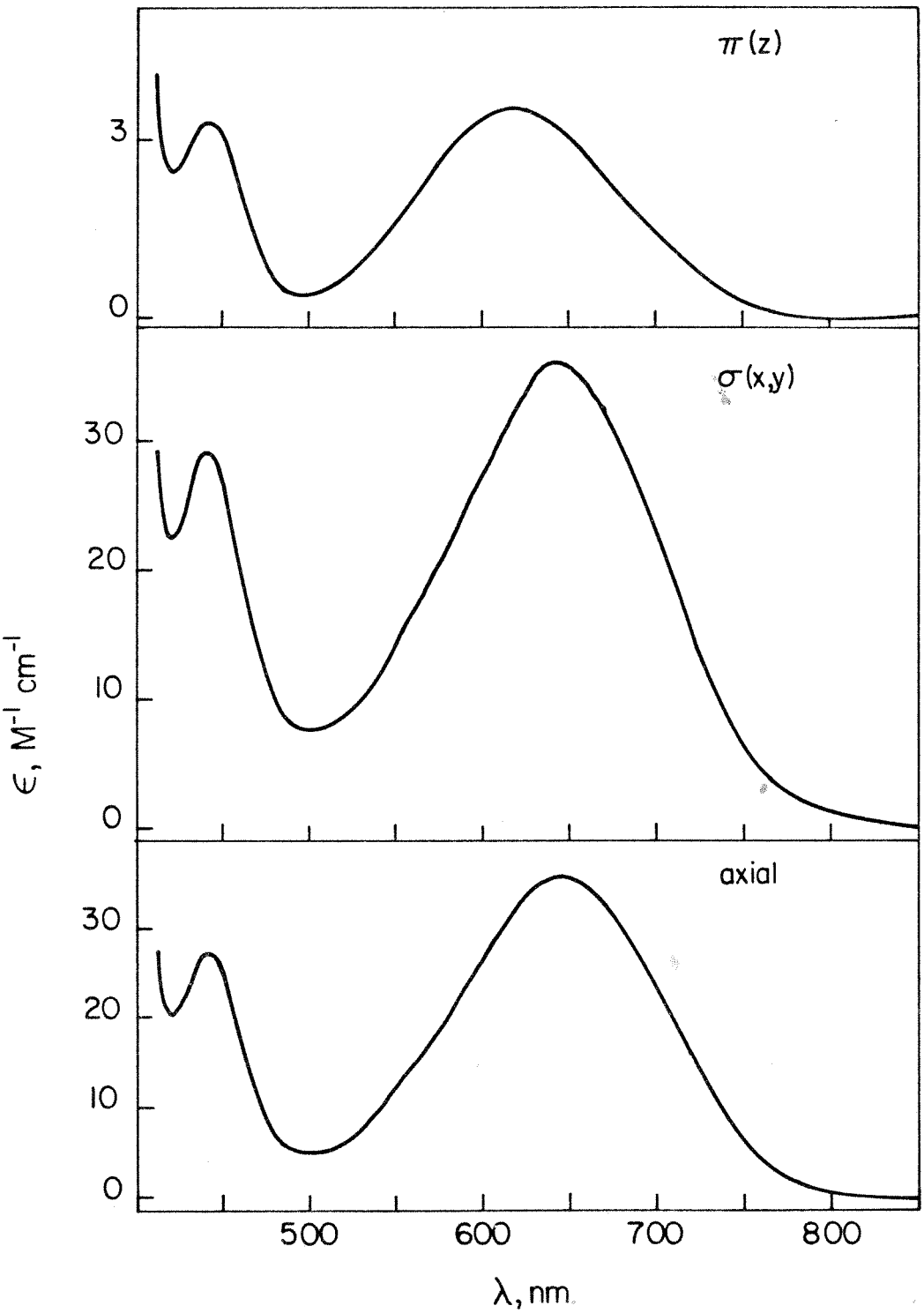
π (z)
σ (x,y)
axial
3
0
30
20
10
0
30
20
10
0
500
600
700
800
ε, M⁻¹ cm⁻¹
λ, nm

Figure 3.4. Single crystal polarized electronic absorption spectra of $(Ph_4As)MoOCl_4$ at 5 K.

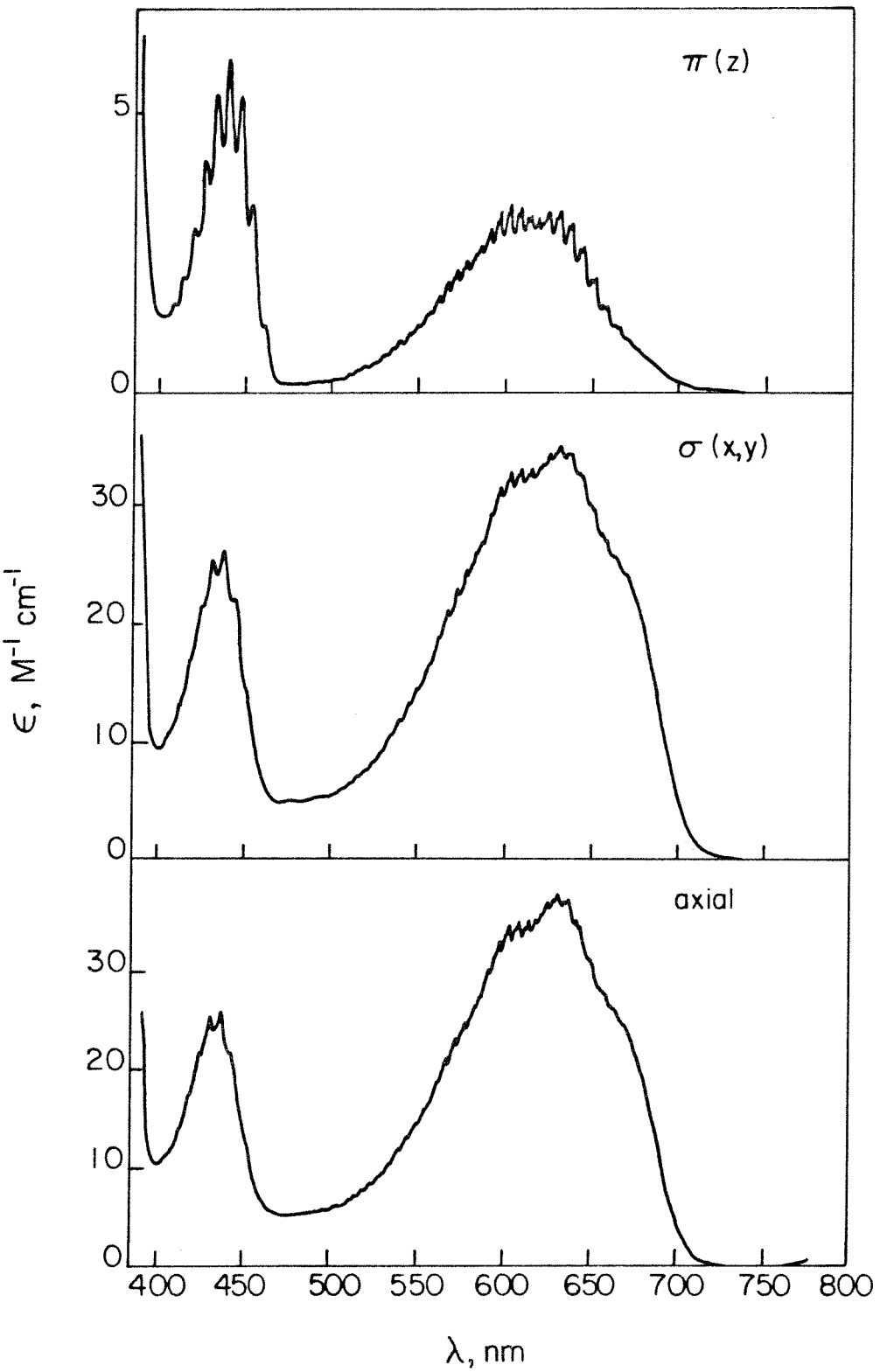
π (z)
σ (x,y)
axial
5
0
30
20
10
0
30
20
10
0
400
450
500
550
600
650
700
750
800
λ, nm
ε, M⁻¹ cm⁻¹

between the σ and axial spectra indicates that both bands arise from electric dipole induced transitions. At the absorption maxima, then, the angles between the crystal axis and transition moments are 66° for the higher and 74° for the lower energy band. Upon cooling from room temperature to 5K, both bands lose some intensity and a great deal of vibrational fine structure resolves. The 675 to 725 nm edge of the lower energy band is unstructured but at slightly shorter wavelengths, three distinct progressions of 900, 165, and 50 cm^{-1} are apparent. The peak positions and energy spacings of these progressions are identical in the σ and π spectra and are listed in Table 3.2. The band maximizing near 430 nm displays a much simpler vibrational progression in a ca. 350 cm^{-1} mode. The peak maxima in this progression are not the same in the σ and π spectra but, as with the lower energy band, are better resolved in the π polarization. The peak maxima and energy spacings for the 430 nm band are listed in Table 3.3. The oscillator strengths of both absorption bands at room temperature and 5K are outlined in Table 3.4.

Crystalline samples of $(Ph_4As)MoOCl_4$ also luminesce and the corrected room temperature and 5K emission spectra of the $MoOCl_4^-$ ion are shown in Figure 3.5. The excitation wavelength for these spectra was 436 nm though identical spectra resulted from 690 nm excitation. Clearly, much less vibrational fine structure is present in emission at low temperature than is found in the absorption spectrum even though the emission monochromator resolution was <50 cm^{-1}. Only a poorly resolved progression in a ca. 1,000 cm^{-1} mode appears at 5K. Luminescence was not observed from solutions of $(Ph_4As)MoOCl_4$

Table 3.2. Vibronic peak maxima and spacings of the lowest energy absorption band of $(Ph_4As)MoOCl_4$ at 5 K.

λ_{max}, nm[a]	$\tilde{\nu}$, cm^{-1}	Energy separations, cm^{-1}		
680.5	14,695			
673.5	14,848	55	163	
671.0	14,903			
666.2	15,011	58	159	
663.6	15,069			
659.2	15,170	58	167	
656.7	15,228			
652.0	15,337	57	162	
649.6	15,394			
645.2	15,499	56	165	
642.9	15,555			
638.4	15,664	54	164	
636.2	15,718			
631.8	15,828	45	159	907
630.0	15,873			
625.5	15,987	54		
623.4	16,041			
621.8	16,082			
619.3	16,147			
615.6	16,244			
613.4	16,303			
609.5	16,407			

Table 3.2. Continued

λ_{max}, nm[a]	$\tilde{\nu}$, cm^{-1}	Energy separations, cm^{-1}
607.5	16,461	
603.5	16,570	
601.7	16,620	900
597.5	16,736	
595.6	16,790	
591.7	16,900	
590.0	17,056	
583.3	17,144	
581.0	17,212	
577.7	17,310	
575.7	17,370	
572.3	17,473	
570.5	17,528	890
567.0	17,637	
565.5	17,683	
562.0	17,794	
560.0	17,857	
557.0	17,953	
554.5	18,034	
552.3	18,106	
549.5	18,198	
547.7	18,258	
544.5	18,365	

Table 3.2. Continued

λ_{max}, nm	$\tilde{\nu}$, cm^{-1}
542.9	18,420
539.7	18,529
538.3	18,577
535.2	18,685
533.7	18,737
530.7	18,843
528.9	18,907
524.3	19,073
519.5	19,249
515.3	19,406
511.0	19,569
509.6	19,623
505.3	19,790
500.9	19,964
496.7	20,133
492.2	20,317
488.0	20,492
484.1	20,657
480.5	20,812
477.0	20,964
473.5	21,119
470.3	21,623
467.7	21,381

a. Uncertainties are ±0.2 nm.

Table 3.3. Vibronic peak maxima and spacings of the 430 nm absorption band of $(Ph_4As)MoOCl_4$ at 5 K.

λ_{max}, nm[a]	$\tilde{\nu}$, cm^{-1}	Energy separations, cm^{-1}
$\sigma(\underline{x},\underline{y})$ Polarization		
457.0	21,882	
		252
451.8	22,134	
		353
444.7	22,487	
		334
438.2	22,821	
		349
431.6	23,170	
		326
425.6	23,496	
		376
418.9	23,872	
		370
412.5	24,242	
		298
407.5	24,540	
$\pi(\underline{z})$ Polarization		
461.2	21,683	
		363
453.6	22,046	
		360
446.3	22,406	
		357
439.3	22,763	
		348
432.7	23,111	
		352
426.2	23,463	
		347
420.0	23,810	
		339
414.1	24,149	
		361
408.0	24,510	

a. Uncertainties are ± 0.2 nm.

Table 3.4. Oscillator strengths and calculated radiative decay rates for the two lowest energy bands in $(Ph_4As)MoOCl_4$.

Band	Polarization	f(T = 300 K)	f(T = 5 K)	k_r, s^{-1}
625 nm	$\sigma(\underline{x}, \underline{y})$	$6.4\,(3) \times 10^{-4}$	$5.0(3) \times 10^{-4}$	7×10^4
625 nm	$\pi(\underline{z})$	$6.0(3) \times 10^{-5}$	$3.9(3) \times 10^{-5}$	
430 nm	$\sigma(\underline{x}, \underline{y})$	$2.9(3) \times 10^{-4}$	$1.6(2) \times 10^{-4}$	
430 nm	$\pi(\underline{z})$	$3.4(3) \times 10^{-5}$	$3.6(3) \times 10^{-5}$	

Figure 3.5. Corrected luminescence spectra of $(Ph_4As)MoOCl_4$ at (a) ambient temperature and (b) 5 K, recorded with 436 nm excitation.

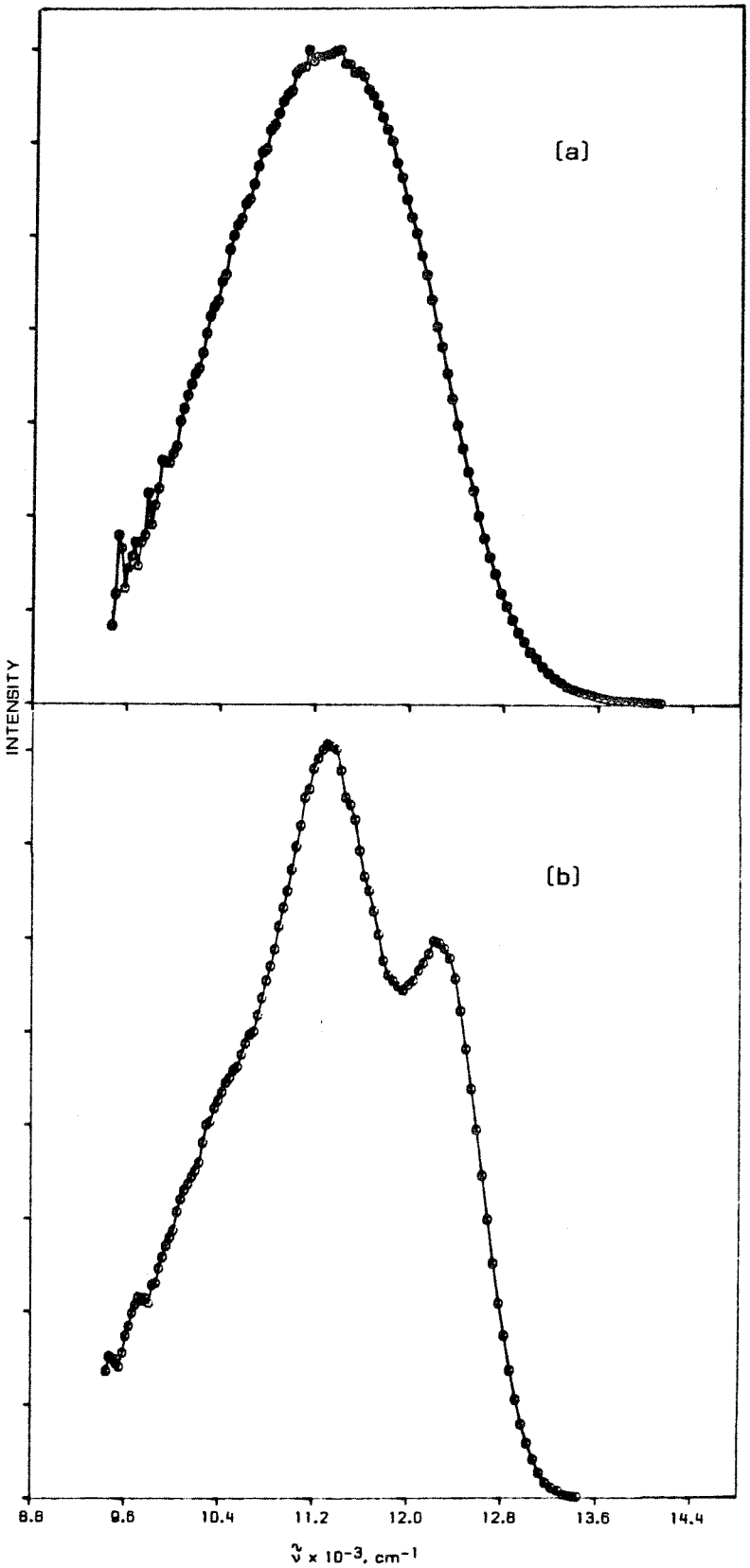
[a]
[b]
INTENSITY
8.8
9.6
10.4
11.2
12.0
12.8
13.6
14.4
$\tilde{\nu} \times 10^{-3}$, cm^{-1}

in dry, degassed CH_2Cl_2 nor from $MoOCl_5^{2-}$ in frozen (77K) concentrated HCl glasses.

The luminescence lifetime of crystalline $(Ph_4As)MoOCl_4$, measured with 532 nm excitation, is 160 ns at room temperature and increases to 1.37 μs upon cooling to 4.8K. As shown in Figure 3.6, however, the change in lifetime is rather sudden with the greatest variation occurring between 240 and 300K. That the radiative decay rate calculated from the Strickler-Berg formula (eqn 2.18, Table 3.4) is about ten times slower than the luminescence decay rate and that the oscillator strength of the lower energy band changes by only 10% upon cooling from 300 to 5K indicate that k_{nr} (eqn 2.17) is responsible for the behavior illustrated in Figure 3.6. Apparently, the non-radiative decay rate is strongly temperature dependent and, at least in the high temperature region, qualitatively exhibits Arrhenius activation behavior (Figure 3.7).

The spectra of $(Ph_4As)MoOBr_4$ are very much like those of $(Ph_4As)MoOCl_4$ and are shown in Figure 3.8. The absorption spectrum of a single crystal of $(Ph_4As)MoOBr_4$ at 77K exhibits three prominent features. The lowest energy band maximizes near 630 nm and displays vibrational progressions in 900 and 130 cm^{-1} modes though the low energy edge is unstructured. The very weak absorption around 720 nm is probably due to a small amount of $(Ph_4As)MoOBr_4(OH_2)$ in the crystal lattice. Unlike the chloro complex, $MoOBr_4^-$ possesses two weak absorption bands between 450 and 500 nm. The two bands are polarized similarly (probably xy, by analogy to $MoOCl_4^-$) and neither is structured at low temperature. The luminescence spectra

Figure 3.6. Variation in luminescence decay rate of $(Ph_4As)MoOCl_4$ as a function of temperature between 5 and 300 K.

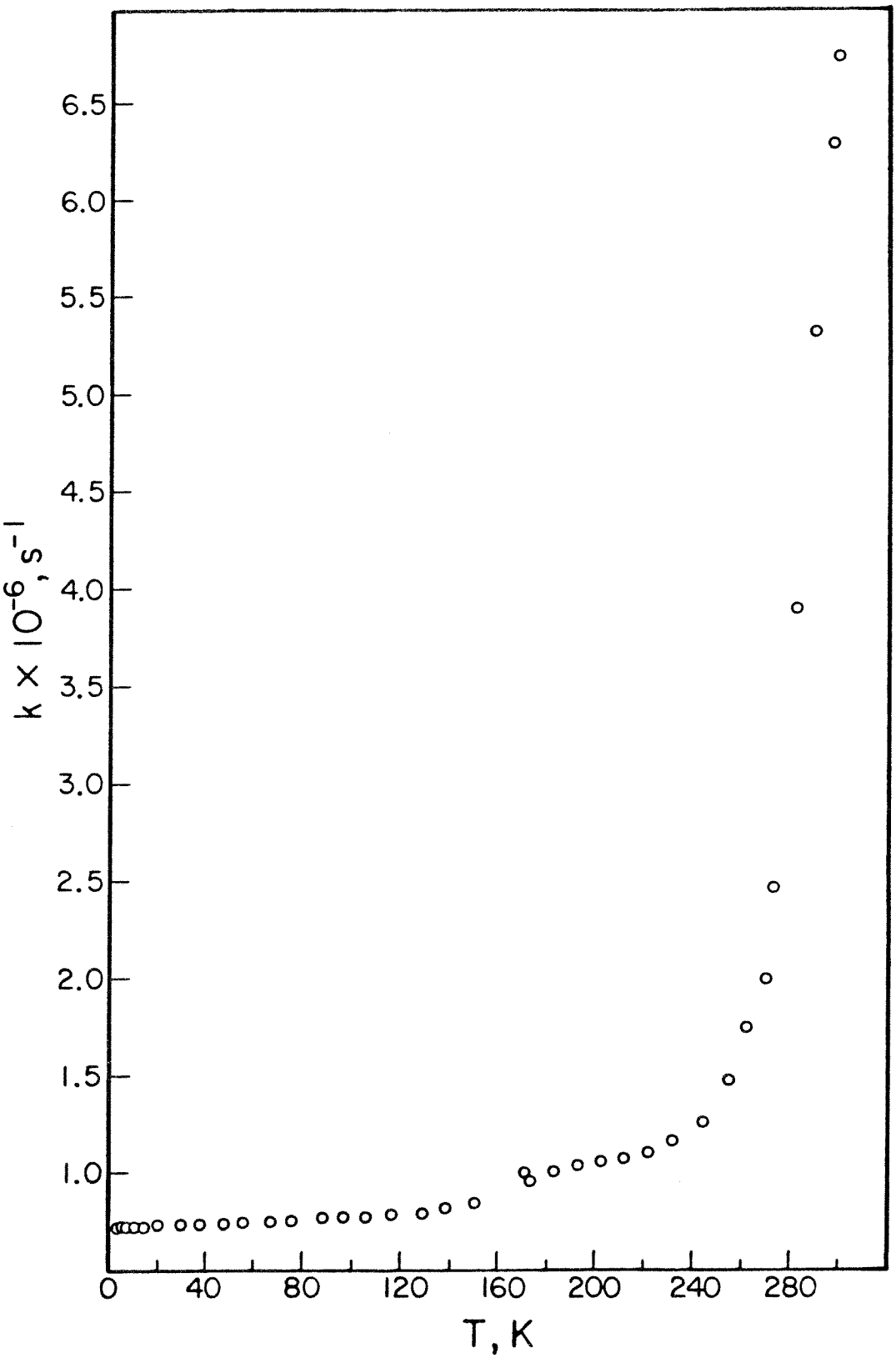
6.5
6.0
5.5
5.0
4.5
4.0
3.5
3.0
2.5
2.0
1.5
1.0
k X 10^-6, s^-1
0
40
80
120
160
200
240
280
T, K

Figure 3.7. Arrhenius plot of the luminescence decay rate of $(Ph_4As)MoOCl_4$.

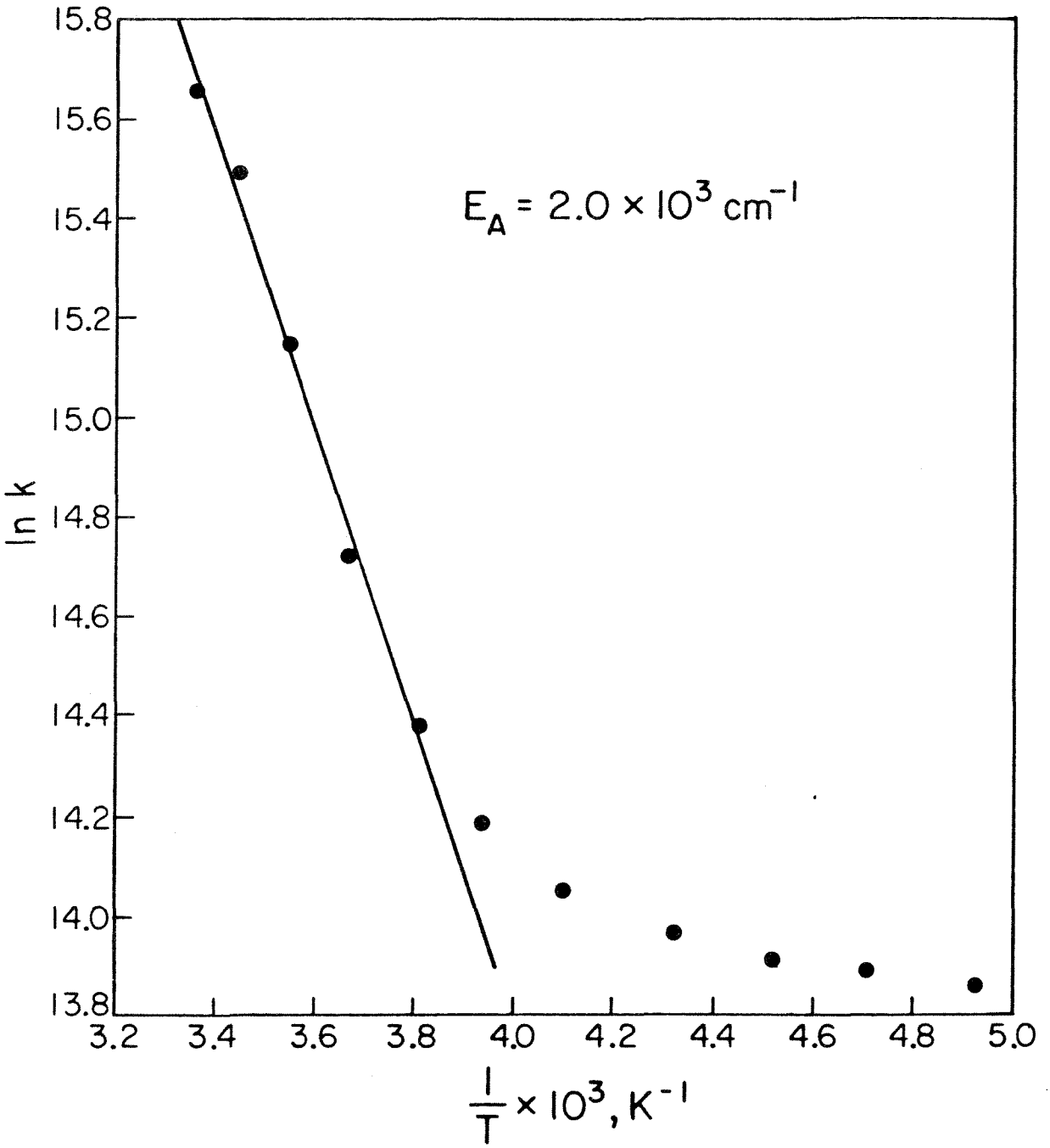
15.8
15.6
15.4
15.2
15.0
14.8
14.6
14.4
14.2
14.0
13.8
ln k
$E_A = 2.0 \times 10^3\ cm^{-1}$
3.2
3.4
3.6
3.8
4.0
4.2
4.4
4.6
4.8
5.0
$\frac{1}{T} \times 10^3, K^{-1}$

Figure 3.8. Single crystal polarized electronic absorption spectra of $(Ph_4As)MoOBr_4$ at 30 K. (a) z polarization, (b) xy polarization.

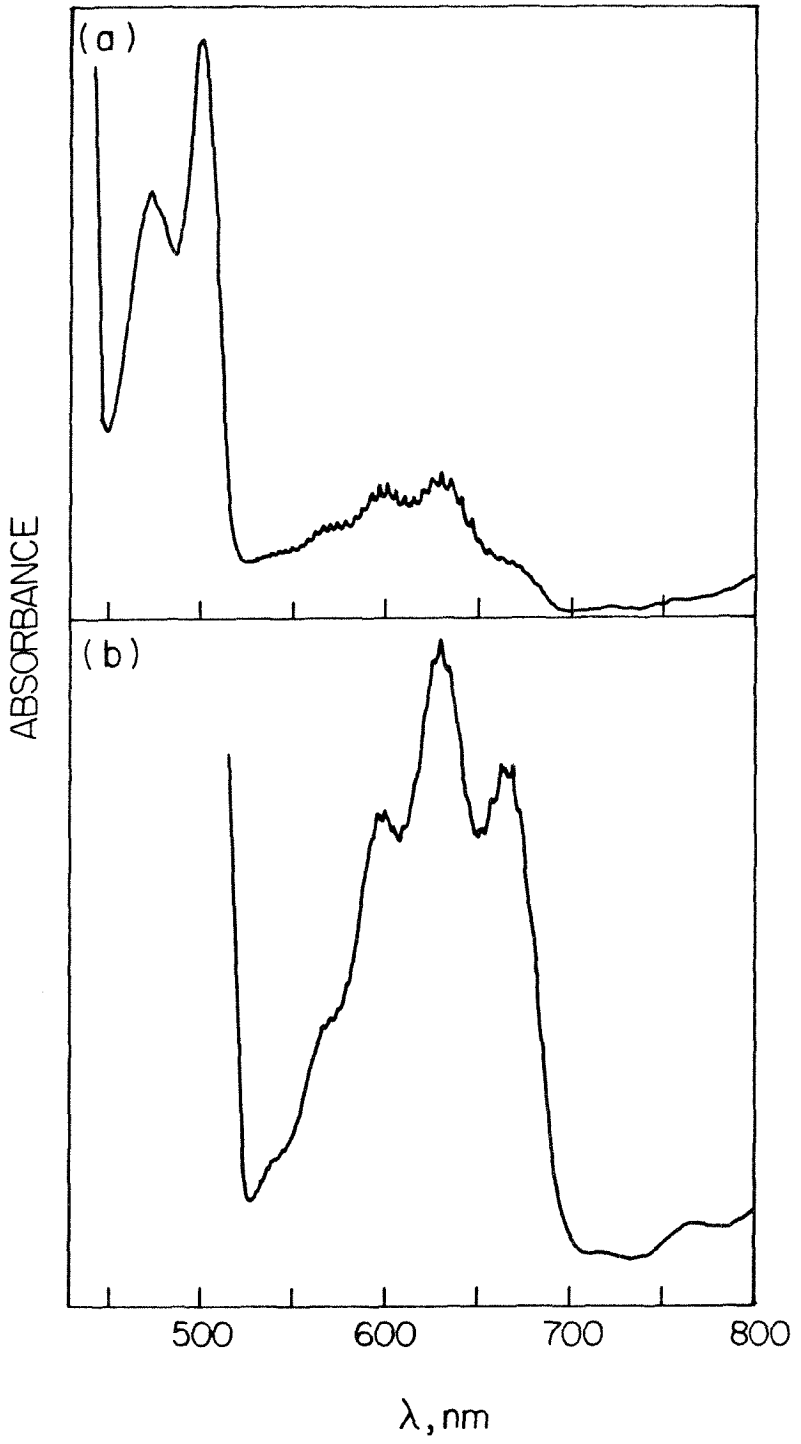
(a)
(b)
ABSORBANCE
500
600
700
800
λ, nm

of $(Ph_4As)MoOBr_4$ are also quite similar to those of the chloride analog and are reproduced in Figures 3.9 and 3.10.

D. Discussion

The electronic structures of the molybdenyl ions have been widely discussed[32] in the twenty-one years since Gray and Hare[23] assigned the electronic spectrum of $MoOCl_5^{2-}$. The molecular orbital scheme proposed by these gentlemen (based on earlier work by Ballhausen and Gray[22] on the vanadyl ion) is reproduced in Figure 3.11. In this model, the metal $d\pi$ orbitals are split into a doubly degenerate pair of $\underline{e}$ symmetry (in the C_{4V} point group) and a non-degenerate $\underline{b}_2$ orbital. The $\underline{e}$ set is primarily metal-oxygen π-antibonding and, as such, is at higher energy than the metal-equatorial ligand π-antibonding $\underline{b}_2$ level. The separation between these orbitals, therefore, reflects the differences in π bonding between the oxygen and chloride ligands. The $d\sigma$ orbitals are also split as a result of the disparate σ bonding to the metal by oxygen and chloride. As will be described below, the molecular orbital model illustrated in Figure 3.11 effectively describes all of the spectroscopic properties of the molybdenyl ion.

The metal center in the molybdenyl ions is formally $\underline{d}^1$ which, based on the Gray-Hare model, produces a paramagnetic $^2B_2$ ground state. The electron paramagnetic resonance spectra of MoO^{3+} species have been thoroughly studied and provide a convenient means of characterizing these ions. $MoOX_5^{2-}$ ($X = F^-$, Cl^-, Br^-) complexes exhibit the axial doublet spectra with anisotropic hyperfine coupling to

Figure 3.9. Corrected luminescence spectrum of $(Ph_4As)MoOBr_4$ at ambient temperature recorded with 436 nm excitation.

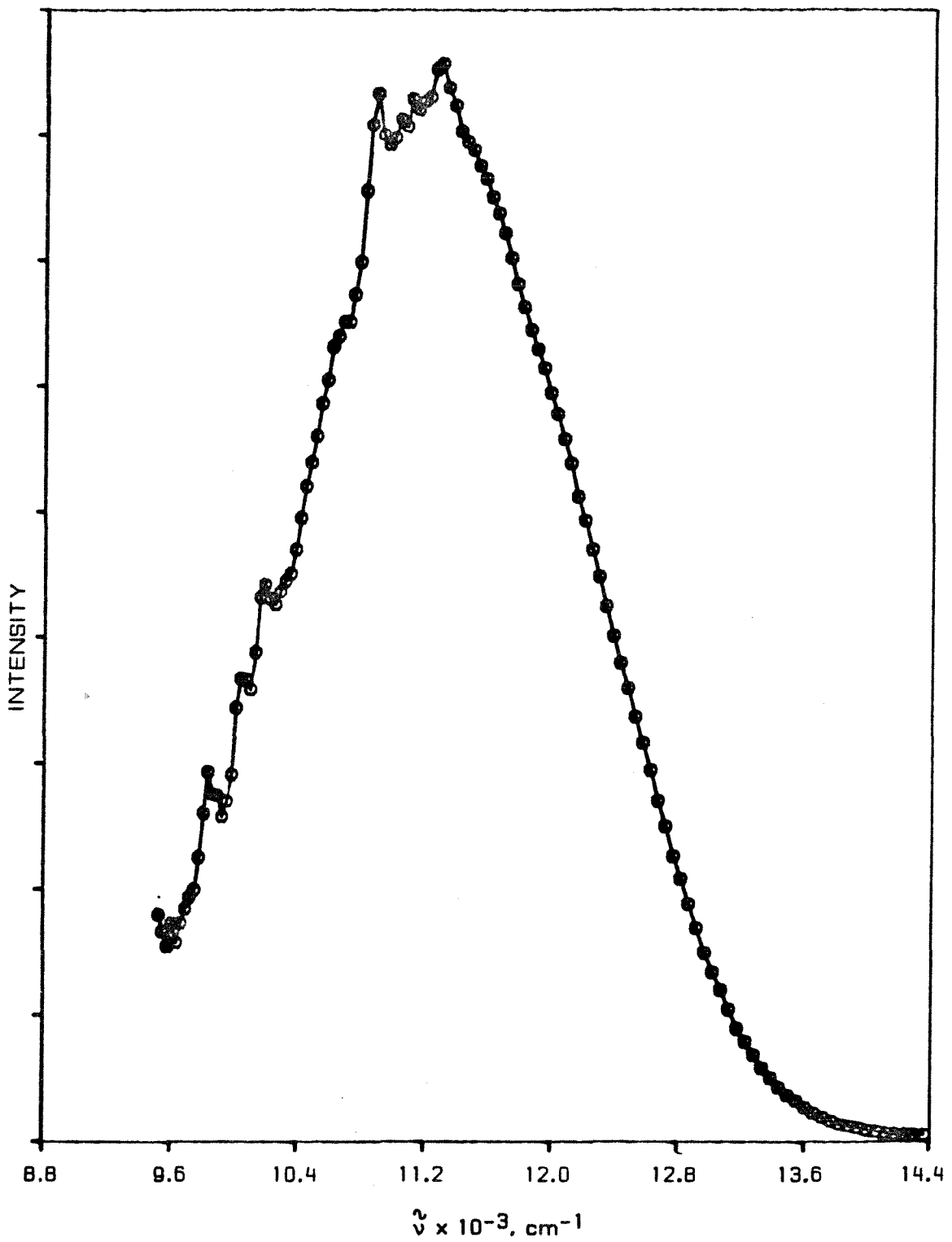
INTENSITY
8.8
9.6
10.4
11.2
12.0
12.8
13.6
14.4
$\tilde{\nu} \times 10^{-3}$, cm^{-1}

Figure 3.10. Corrected luminescence spectrum of $(Ph_4As)MoOBr_4$ at 77 K recorded with 436 nm excitation.

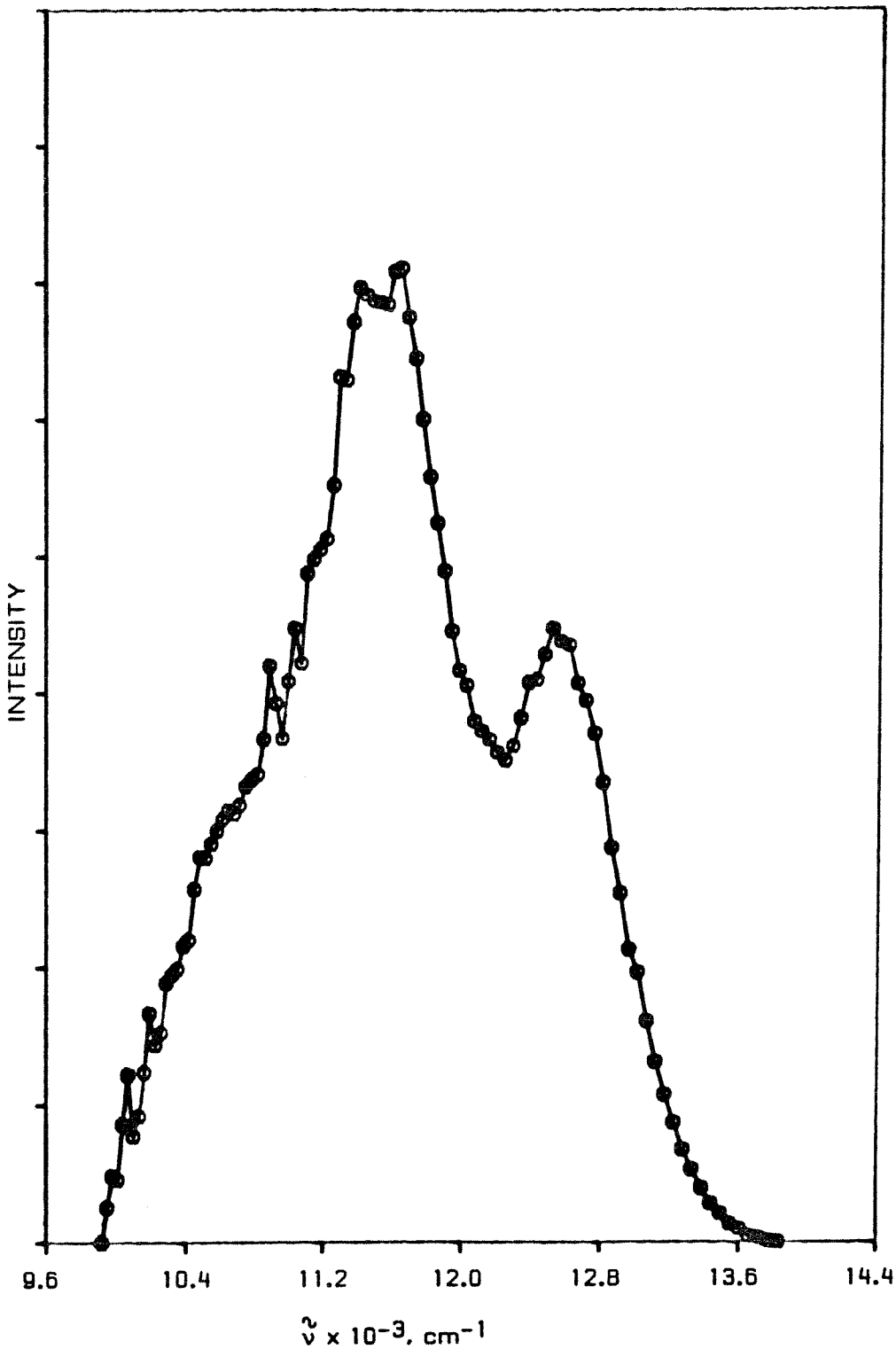
INTENSITY
9.6
10.4
11.2
12.0
12.8
13.6
14.4
$\tilde{\nu} \times 10^{-3}$, cm^{-1}

Figure 3.11. Gray-Hare molecular orbital diagram for the molybdenyl ions.

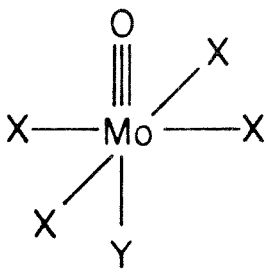

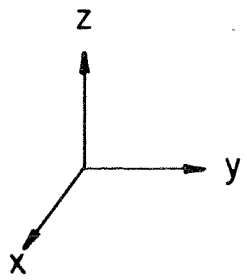

a_1 (z^2) Ground State: $^2B_2$

b_1 (x^2-y^2) Excited States:
$^2E(xz,yz) \leftarrow {}^2B_2$ (xy)

e (xz, yz) $^2B_1(x^2-y^2) \leftarrow {}^2B_2(xy)$

b_2 (xy) $^2A_1(z^2) \leftarrow {}^2B_2$ (xy)

the metal center expected from a lone electron in a non-degenerate orbital in an axially symmetric ligand field.[30,31] The spectra in Figure 3.1, therefore, suggest a central MoO^{3+} core with four equatorial and one axial ligand for molybdenum(V) in concentrated H_2SO_4 and H_3PO_4. It is likely that the four equatorial groups are HSO_4^- or $H_2PO_4^-$ and the axial ligand could be the same as the equatorial or could simply be a water molecule.[25] Molybdenyl ions without halide ligands are uncommon structures[21c] that prove to be particularly helpful in the assignment of MoO^{3+} electronic spectra.

The similarity of the electronic spectra in the region below 30,000 cm^{-1} of molybdenum(V) in concentrated HX ($X = Cl^-$, HSO_4^-, and $H_2PO_4^-$) (Figure 3.2) and crystalline $(Ph_4As)MoOCl_4$ (Figure 3.3) indicates that the two weak bands near 14,000 and 25,000 cm^{-1} arise from transitions localized within the MoO^{3+} structural unit. The higher energy bands in $MoOCl_5^{2-}$ (28,000 and 32,500 cm^{-1}) are not present in the spectra of $MoOX_4^-$ (where $X = HSO_4^-$ or $H_2PO_4^-$ and the ambiguous axial ligand has been omitted) and, therefore, must arise from chloride ligand to metal charge transfer (LMCT) transitions, not oxygen LMCT as originally suggested by Gray and Hare.[23] The halide LMCT transitions red shift when chloride is replaced by bromide and give rise to the bands at 475 and 500 nm in the $(Ph_4As)MoOBr_4$ absorption spectrum.

Recent theoretical work by Weber and Garner[33] on $MoOCl_4^-$ has raised the possibility that Cl → Mo charge transfer transitions may fall at lower energies than 28,000 cm^{-1}. $X\alpha$ calculations performed

by these authors placed the $^2E(\underline{xz}, \underline{yz}) \leftarrow {}^2B_2(\underline{xy})$ and $^2B_1(\underline{x}^2-\underline{y}^2) \leftarrow {}^2B_2(\underline{xy})$ ligand field transitions at 15,600 and 23,300 cm^{-1}, respectively, whereas the lowest chloride LMCT transition ($^2E \leftarrow {}^2B_2$) was predicted at 18,700 cm^{-1}. Weber and Garner concluded that the weak feature peaking at 22,600 cm^{-1} in the spectrum of a crystal of $(Ph_4As)MoOCl_4$ was attributable to the lowest Cl → Mo CT transition ($^2E \leftarrow {}^2B_2$). The evidence offered in Figure 3.2, however, strongly supports the original Gray-Hare $^2B_1(\underline{x}^2-\underline{y}^2) \leftarrow {}^2B_2(\underline{xy})$ assignment for this band because analogous absorptions are present in the spectra of $MoO(HSO_4)_4^-$ and $MoO(H_2PO_4)_4^-$. The fact that the $^2B_1(\underline{x}^2-\underline{y}^2) \leftarrow {}^2B_1(\underline{xy})$ band appears at slightly higher energy (~26,000 cm^{-1}) in the latter two complexes is entirely consistent with simple theoretical considerations because the equatorial ligand field generated by four oxygen-donor ligands should exceed that of four chlorides (the observed increase of 3,000-4,000 cm^{-1} in the $\underline{x}^2-\underline{y}^2/\underline{xy}$ splitting is in line with the ratio $Dq(O)/Dq(Cl) \sim 1.2$[34]). What is more, the equatorial ligand field splitting in $MoOCl_4^-$ (or $MoOCl_5^{2-}$), as deduced from the $^2B_1(\underline{x}^2-\underline{y}^2) \leftarrow {}^2B_2(\underline{xy})$ assignment of the 22,600 cm^{-1} band, agrees closely with the analogous splitting in $MoCl_6^-$ ($^2E_g \leftarrow {}^2T_{2g}$ at 24,000 cm^{-1}).[35] Weber and Garner, in fact, assigned the 475 and 500 nm bands in the $(Ph_4As)MoOBr_4$ spectrum to Br → Mo CT transitions, though they calculate these transitions to lie 9,000 and 7,000 cm^{-1} to lower energy, respectively. This discrepancy is nearly identical to that found in $(Ph_4As)MoOCl_4$ if the lowest energy chloride LMCT transition corresponds to the 28,000 cm^{-1} absorption band. Thus, there is little doubt that the original interpretation of the 22,500 cm^{-1} band in the spectrum of $MoOCl_5^{2-}$ was correct.

The low temperature behavior of the 22,600 cm^{-1} band in the $(Ph_4As)MoOCl_4$ crystal spectrum also supports its assignment to a $^2B_1 \leftarrow {}^2B_2$ transition. The oscillator strength of this band in the xy polarization decreases by about a factor of 2 upon cooling the crystal from room temperature to 5K [$f_{xy}(300K) = 2.9 \times 10^{-4}$; $f_{xy}(5K) = 1.6 \times 10^{-4}$] while in the z polarization the oscillator strength is essentially temperature independent [f_z (300 and 5K) = 3.6×10^{-5}]. The behavior of this band in the xy polarization is consistent with a vibronic mechanism in which the $^2B_1(x^2 - y^2) \leftarrow {}^2B_2(xy)$ transition in $MoOCl_4^-$ gains intensity through a promoting mode of e symmetry.[36] The same vibronic coupling mechanism that is responsible for the temperature dependence of f_{xy} also creates the differences between the xy and z polarizations of the peak maxima in the vibrational fine structure that resolves at 5K. As shown in Table 3.3, the apparent origin and vibronic maxima of the xy polarized progression are blue shifted relative to the corresponding z polarized features. This shift, which would correspond to the energy of the vibronic promoting mode in the $^2B_1$ state, averages 70 cm^{-1} but varies widely from peak to peak. It is unlikely, therefore, that a single promoting mode is involved ($MoOCl_4^-$ possesses three vibrational modes of e symmetry that could give xy polarized intensity to a $^2B_1 \leftarrow {}^2B_2$ transition). In addition, spin-orbit mixing of $^2B_1$ with ^2E states could lead to temperature independent intensity in xy polarization. A spin-orbit coupling mechanism is probably also responsible for the z polarized intensity in the $^2B_1(x^2 - y^2) \leftarrow {}^2B_2(xy)$ transition. The ca. 350 cm^{-1} progression that resolves in this band at 5K indicates a distortion along the totally

symmetric Mo-Cl stretching coordinate ($\nu_{Mo\text{-}Cl}$ = 354 cm^{-1} in the ground state[37]). A distortion along this coordinate is in agreement with the $^2B_1 \leftarrow {}^2B_2$ assignment which involves promotion of an electron from the weakly Mo-Cl π-antibonding $\underline{xy}$ orbital to the Mo-Cl σ-antibonding $\underline{x}^2 - \underline{y}^2$ level. A Franck-Condon fit to the $\underline{z}$ polarized $^2B_1 \leftarrow {}^2B_2$ absorption band, based on a calculated distortion of 0.07 (1) Å (from 2.333(3) Å[26]) along each Mo-Cl bond, is shown in Figure 3.12 (Appendix 1).

The $^2E(\underline{xz}, \underline{yz}) \leftarrow {}^2B_2(\underline{xy})$ assignment of the lowest energy absorption band near 15,500 cm^{-1} in $(Ph_4As)MoOCl_4$ has remained uncontested in the past twenty years. This excitation corresponds to the promotion of an electron from the $b_2(\underline{xy})$ orbital to the Mo-O π-antibonding $e(\underline{xz}, \underline{yz})$ orbital. The energy of this band is insensitive to the nature of the equatorial ligand, as expected from its assignment, but does red shift upon axial coordination trans to the oxo ligand (compare spectra of $(Ph_4As)MoOCl_4$, Figure 3.3, and MoO^{3+} in HX, Figure 3.2, where the sixth coordination site is presumably occupied by X^- or H_2O). The $^2E \leftarrow {}^2B_2$ transition should be $\underline{xy}$ polarized though spin-orbit and vibronic coupling mechanisms could account for the 16° deflection of the transition moment out of the equatorial plane.

The low temperature single crystal absorption spectrum of $(Ph_4As)MoOCl_4$ (Figure 3.4) provides a wealth of information about the ^2E excited state. The band is clearly split into two components: one highly structured absorption envelope and an apparently unstructured band at lower energy. The excitation wavelength independence of the $(Ph_4As)MoOCl_4$ emission spectrum indicates that the luminescence arises from the lower energy component of the ^2E state and, like its

Figure 3.12. Franck-Condon fit to the z polarized $^2B_1 \leftarrow {}^2B_2$ absorption band in $(Ph_4As)MoOCl_4$. Upper spectrum: calculated. Lower spectrum: experimental.

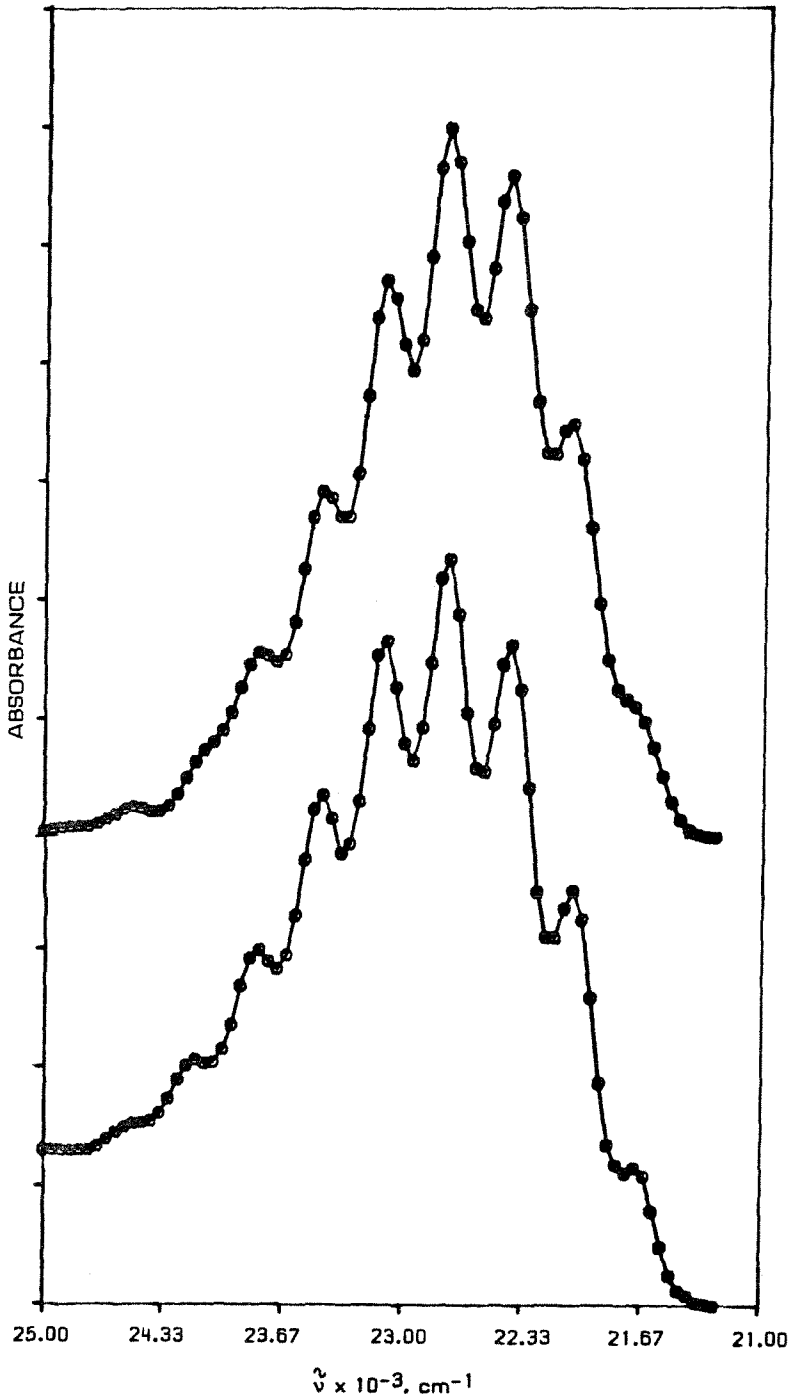
ABSORBANCE
25.00
24.33
23.67
23.00
22.33
21.67
21.00
$\tilde{\nu} \times 10^{-3}$, cm^{-1}

counterpart in absorption, is not highly structured, displaying only a poorly resolved 1,000 cm^{-1} progression. Not only, then, are there two components in the ^2E absorption band, but they also correspond to states with significantly different potential surfaces. Two perturbations can split the fourfold degeneracy of the ^2E potential surfaces: spin orbit coupling and Jahn-Teller distortions.[38,39] A ^2E state yields Γ_6 and Γ_7 in the C'_{4v} point group and first-order ligand field theory predicts that the two components will be separated by ξ, the effective molecular spin orbit coupling constant, with the Γ_7 state at higher energy (Appendix 2). A transition from the $\Gamma_7(^2B_2)$ ground state to a Γ_6 excited state is electric dipole allowed in xy polarization, whereas a transition to a Γ_7 state is allowed in xy and z polarizations. The highly structured component of the 15,500 cm^{-1} absorption system in $(Ph_4As)MoOCl_4$ can therefore be assigned to the $\Gamma_7(^2E) \leftarrow \Gamma_7(^2B_2)$ transition and the lower energy component to $\Gamma_6(^2E) \leftarrow \Gamma_7(^2B_2)$. This spin-orbit coupling interaction, however, should have no first order effect on the shapes of the $\Gamma_6(^2E)$ and $\Gamma_7(^2E)$ potential surfaces and it is probably the so-called pseudo-Jahn-Teller coupling that distorts them.

The vibrational fine structure that resolves in the $^2E \leftarrow {}^2B_2$ absorption and emission bands does, nevertheless, prove to be quite informative. The 900 cm^{-1} progression that accompanies the $\Gamma_7(^2E) \leftarrow \Gamma_7(^2B_2)$ transition indicates a distortion along the Mo-O stretching coordinate as does the 1,000 cm^{-1} progression in the $\Gamma_6(^2E) \rightarrow \Gamma_7(^2B_2)$ emission band. The spectral congestion in the absorption band prohibits a reliable Franck-Condon analysis of the vibrational fine structure but a reasonable fit (Appendix 1) to the

emission band results from a calculated 0.09(1) Å (from 1.61(1) Å[26]) elongation of the molybdenum oxygen bond (Figure 3.13) in the $\Gamma_6(^2E)$ state. The assignment of the 165 cm^{-1} progression is less apparent. The energy of the mode is similar to any of three ground state bending vibrations [$\nu_{\underline{a}_1}(\pi_{MoCl})$ = 184 cm^{-1}, $\nu_{\underline{b}_1}(\pi_{MoCl})$ = 158 cm^{-1}, and $\nu_{\underline{b}_2}(\delta_{MoCl})$ = 167 cm^{-1}] and distortions along all three coordinates are allowed in a $^2E \leftarrow {}^2B_2$ transition, the latter two corresponding to Jahn-Teller distortions. It is tempting to assign the 165 cm^{-1} progression to a distortion along the symmetric O-Mo-Cl bending coordinate [$\nu_{\underline{a}_1}(\pi_{MoCl})$] since the elongation of the Mo-O bond should be accompanied by a reduction in the O-Mo-Cl bond angle, but this does not preclude Jahn-Teller distortions. Finally, the 50 cm^{-1} splitting of the vibronic components in $\Gamma_7(^2E) \leftarrow \Gamma_7(^2B_2)$ could represent a lattice mode progression.

The final insights into the nature of the $\Gamma_6(^2E)$ state are provided by its luminescence properties. Sparingly few $\underline{d}^1$ metal complexes are known to emit[40] but the luminescence quantum yield of the $\Gamma_6(^2E)$ state in $(Ph_4As)MoOCl_4$, based on $k_r = 7 \times 10^4\ s^{-1}$ (Table 3.4), is $\phi_{em} \sim 0.1$. The temperature dependence of the lifetime of this excited state then (Figure 3.6) reflects the behavior of the non-radiative decay rate. The explanation of this thermal activation probably lies in the Gaussian regime[41] of non-radiative molecular electronic relaxation theory. This limiting case results from an expansion of the function $[G_+(t) + G_-(t)]$ (eqn. 2.26) in a power series of t,[41-43]

$$G_+(t) + G_-(t) = G + it \sum_{\nu} \omega_{\nu} X_{\nu} - \tfrac{1}{2} D^2 t^2 + O(t^3) \qquad (3.1)$$

Figure 3.13. Franck-Condon fit to the $\Gamma_6(^2E) - \Gamma_7(^2B_2)$ emission band in $(Ph_4As)MoOCl_4$. Upper spectrum: calculated. Lower spectrum: experimental.

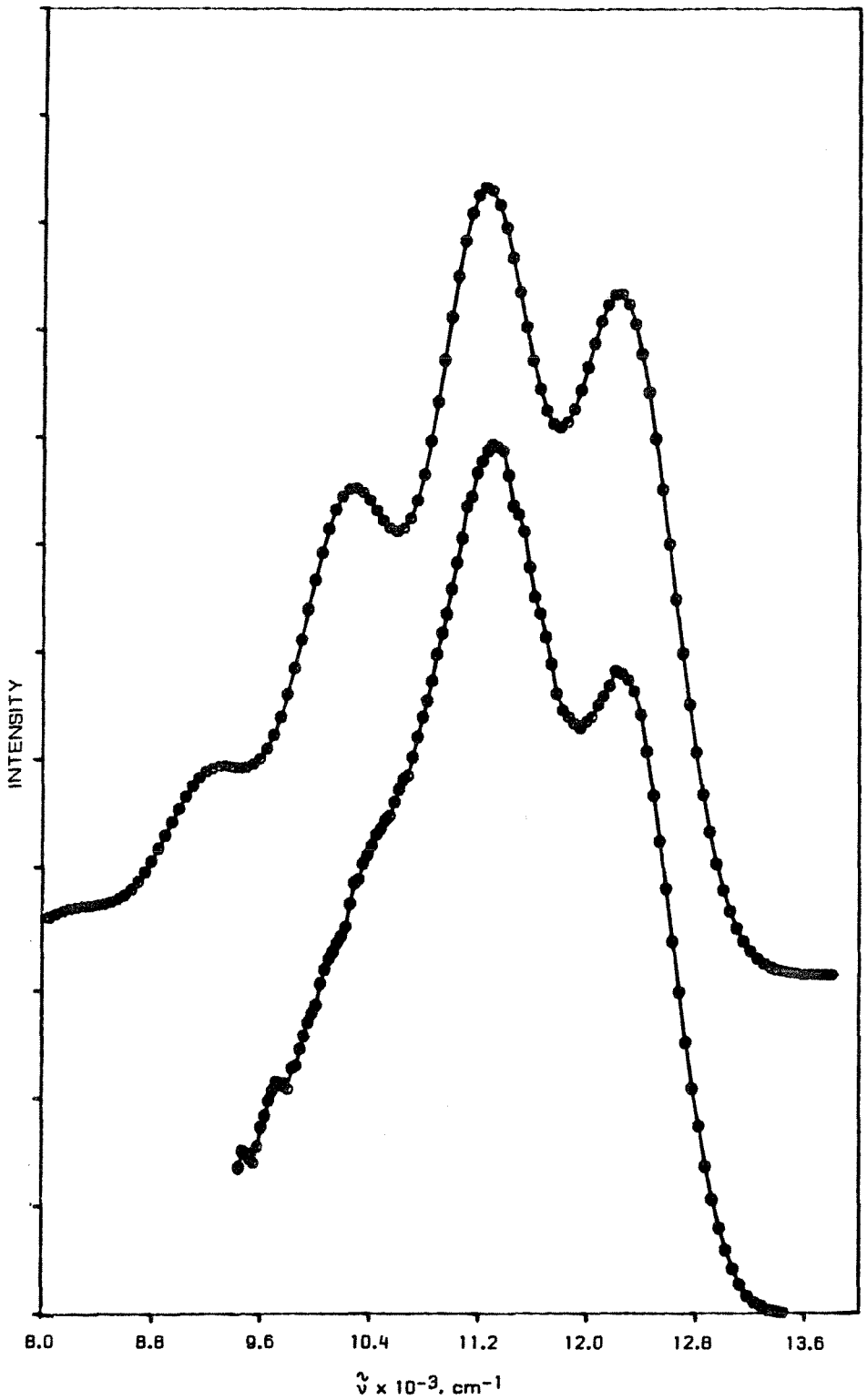
INTENSITY
8.0
8.8
9.6
10.4
11.2
12.0
12.8
13.6
$\tilde{\nu} \times 10^{-3}$, cm^{-1}

where

$$D^2 = \sum_{\nu} \omega_{\nu} X_{\nu} (2\bar{n}_{\nu} + 1). \tag{3.2}$$

This expansion can be truncated after the quadratic terms and substituted into (2.24) to yield

$$k_{nr}(s \rightarrow n) = \frac{\sqrt{2\pi}}{4\hbar D} |C_{sn}^{\mu}|^2 \omega_{\mu} \{(\coth y_{\mu} + 1)\exp[(\Delta E - \hbar\omega_{\mu} - E_M)^2/2D^2\hbar^2]$$

$$+ (\coth y_{\mu} - 1)\exp[(\Delta E + \hbar\omega_{\mu} - E_M)^2/2D^2\hbar^2]\} \tag{3.3}$$

where

$$E_M = \sum_{\nu} \hbar \omega_{\nu} X_{\nu} . \tag{3.4}$$

Two further approximations permit (3.3) to be cast in a more familiar form.[41-43] First, it is assumed that an average frequency, $\langle\omega\rangle$, can be introduced in (3.2) such that

$$\hbar^2 D^2 \cong \hbar \langle\omega\rangle E_M \coth \left(\frac{\hbar\langle\omega\rangle}{2k_B T}\right). \tag{3.5}$$

Second, if the promoting frequency is much smaller than $(\Delta E - E_M)$, then it may be neglected in the exponents of (3.3). Equation (3.3) then assumes the form of an Arrhenius activation law,[41-43, 44]

$$k_{nr}(s \rightarrow n) = \left(\frac{\pi}{4E_M k_B T^*}\right)^{\frac{1}{2}} |C_{sn}^{\mu}|^2 \omega_{\mu} \coth y_{\mu} \exp[-E_A/k_B T^*] \tag{3.6}$$

where

$$E_A = \tfrac{1}{4}\frac{(\Delta E - E_M)^2}{E_M} \qquad (3.7)$$

and

$$k_B T^* = \tfrac{1}{2}\hbar\langle\omega\rangle \coth(\hbar\langle\omega\rangle/2k_B T). \qquad (3.8)$$

The validity of equation 3.6, of course, rests upon the simplifying assumptions incorporated in its derivation. The higher order terms in (3.1) can be safely ignored if G is large enough to permit the generating function f(t) (2.23) to decay exponentially to a small value before these terms in (3.1) can become non-negligible.[42] Hence, the most common criterion for Gaussian behavior is $G \gg 1$, though some alternatives and exceptions have been noted.[41] The magnitude of G reflects the extent to which the Ψ_S potential surface is displaced relative to that of Ψ_n. When G is large, the two surfaces are likely to intersect and the parameters in (3.6) are directly related to the shapes and positions of these surfaces (Figure 3.14). The vertical transition energy is just $(\Delta E + E_M)$, the magnitude of the displacement between surfaces is $\sqrt{2X_\nu}$, and it has been shown[20, 42] that $E_A = \tfrac{1}{4}\frac{(\Delta E - E_M)^2}{E_M}$ for any N-dimensional coordinate space. In the Gaussian regime, therefore, Ψ_S decays at low temperature ($E_A \gg kT^*$) by tunnelling to Ψ_n, but at higher temperatures by crossing over the activation barrier E_A to the Ψ_n surface below.[43]

The low temperature luminescence spectrum demonstrates that the $\Gamma_6(^2E)$ state in $(Ph_4As)MoOCl_4$ is greatly distorted relative to the ground Γ_7 ($^2B_2$) state and it is reasonable to expect (3.6) to describe its non-radiative decay behavior. Though equation 3.6 qualitatively

Figure 3.14. Shapes and positions of ground and excited state potential surfaces of a molecule in the Gaussian regime of non-radiative decay.

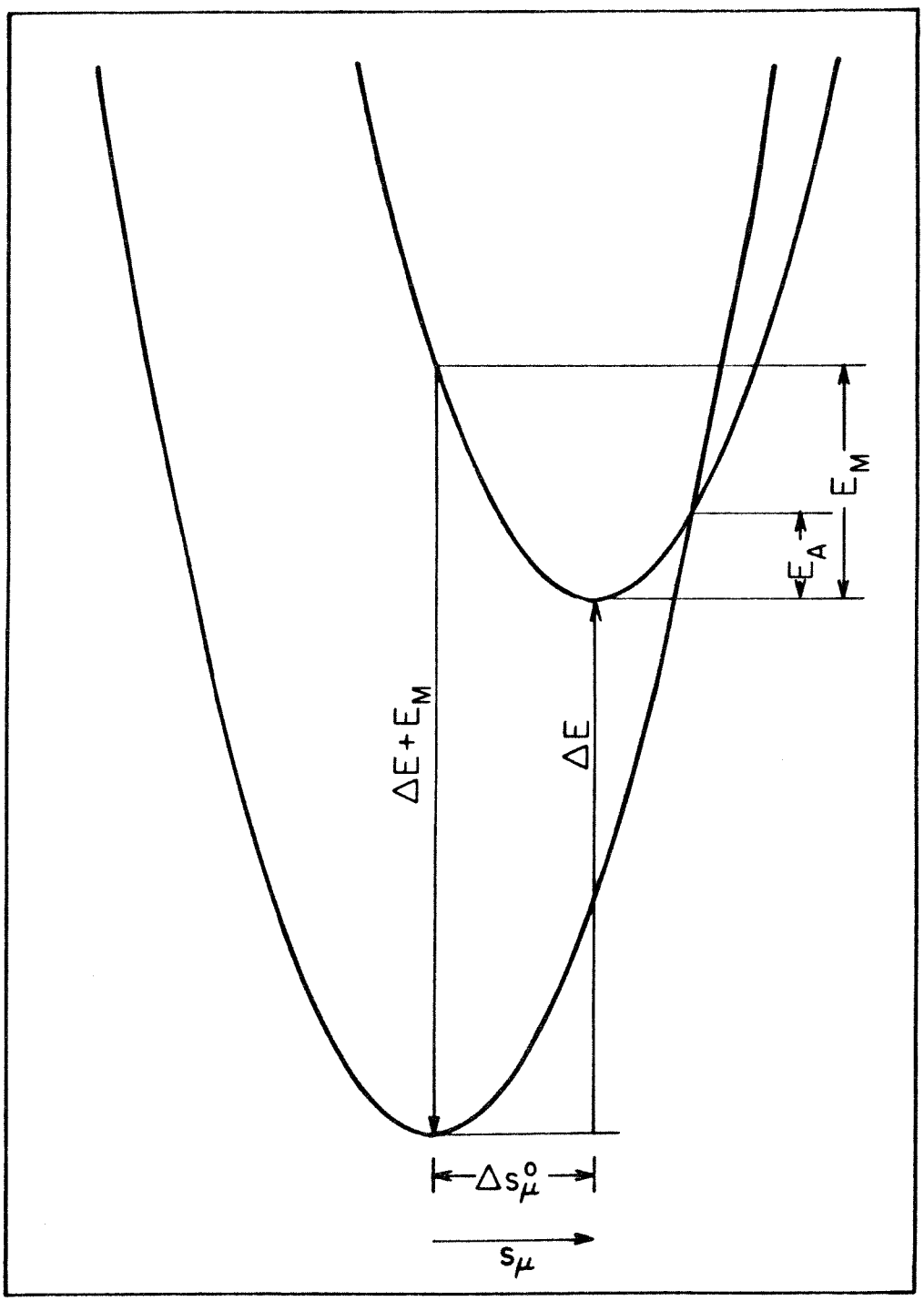
E_M
E_A
$\Delta E + E_M$
ΔE
Δs_μ^o
s_μ

explains the data in Figure 3.7, it fails to fit these data exactly. The reasons for this failure probably lie in the many approximations used to arrive at this rather simple expression for k_{nr}. Foremost among these are the simple displaced harmonic potential surface model, the neglect of promoting modes, the expansion in (3.1), and the introduction of an average vibrational frequency $\langle\omega\rangle$. While the inadequacies of these approximations do not necessarily render (3.6) invalid, they could prevent precise modelling of experimental data (unless a prohibitively and ridiculously large set of parameters is included). It must suffice, therefore, simply to say that the non-radiative decay of the $\Gamma_6(^2E)$ state in $(Ph_4As)MoOCl_4$ lies in the Gaussian regime that is approximated by equation 3.6.

The non-radiative decay of molybdenyl ions in solution or frozen glasses is so rapid that no luminescence can be observed. These ions are, therefore, of little photochemical value. The $(\underline{xz},\underline{yz}) \leftarrow (\underline{xy})$ transition, however, is likely to be found in other metal-oxo complexes and, if a new barrier to non-radiative decay can be introduced, these species could possess quite long-lived excited states. A system of this type, in which the new barrier is a spin restriction, is described in the following chapter.

CHAPTER FOUR

Dioxorhenium Complexes

A. Introduction

The trans-dioxometal core is a common structural unit for second and third row d^2 metal centers. Examples from groups VI through VIII have been isolated and characterized.[45] In all cases the O-M-O linkage is nearly linear with short, ca. 1.8 Å, metal-oxygen multiple bonds.[45] The four equatorial ligands that complete the tetragonally distorted octahedral coordination sphere in these species are usually halides, pseudo-halides, or amines. The complexes discussed in this chapter all possess a trans-dioxorhenium core with cyanide or amine equatorial ligands. The electronic spectroscopy of trans-dioxometal species has not been as extensively investigated as that of the mono-oxo "yl" ions and the major portion of this chapter is devoted to a discussion of the electronic spectroscopy and photophysical properties of three representative dioxorhenium ions. The results of these investigations provide a reasonably clear picture of the low-lying dioxorhenium excited states and suggest the potential for some novel reactivity: photoinduced oxygen atom transfer. The final section of this chapter, then, includes a discussion of the solution luminescence behavior of dioxorhenium complexes as well as experiments directed toward excited state atom transfer chemistry.

B. Materials and Methods

Miscellaneous Procedures: Dry dichloromethane was prepared as described in Chapter Three. Burdick and Jackson brand tetrahydrofuran (THF) was refluxed over and distilled from a mixture of sodium metal and benzophenone under an Ar atmosphere, degassed with five

freeze-pump-thaw cycles, and stored under vacuum over sodium and benzophenone. After a few days, the THF solution acquired the characteristic purple color of the benzophenone dianion. Pyridine from Burdick and Jackson was refluxed under Ar over sodium metal, distilled, degassed with five freeze-pump-thaw cycles, and stored under vacuum over CaH_2. Spectroscopy grade acetone (Baker) was degassed with five freeze-pump-thaw cycles and stored under vacuum over activated Linde 4Å molecular sieves. These solvents were transferred by flask to flask distillation on a high vacuum line ($< 10^{-3}$ torr) and further degassed with three freeze-pump-thaw cycles prior to use. All anaerobic manipulations were performed on the high vacuum line described in Chapter Three. Elemental analyses were performed by Larry Henling in the Caltech Analytical Laboratory.

$K_3ReO_2(CN)_4$: This salt was prepared by the method of Beard et al.[46] A final crystallization by slow evaporation of an aqueous solution of $K_3ReO_2(CN)_4$ produced large, well-formed rhombic crystals which were characterized by oscillation and Weissenberg X-ray photographs.[47]

$[ReO_2(py)_4]BPh_4$ (py = pyridine, Ph = C_6H_5): The iodide salt of this cation was prepared by the procedure of Beard et al.[48] The tetraphenylborate salt was isolated by addition of an aqueous $NaBPh_4$ solution to a solution of $[ReO_2(py)_4]I$ in water. The resulting yellow solid was filtered and washed with water. Large crystals of this salt were grown by layering petroleum ether over a 4:1 acetone:pyridine solution containing the complex. As the petroleum ether diffused into the lower layer, large red prismatic crystals of $[ReO_2(py)_4]BPh_4$ formed. Elemental analysis results were: C, 61.76%; H, 4.79%;

N, 6.57%. Calculated values were: C, 61.90%; H, 4.72%; N, 6.56%.

$[ReO_2(py\text{-}d_5)_4]BPh_4$ (py-d_5 = C_5D_5N): This complex was prepared by the same procedure used for the pyridine analog but replacing H_2O with D_2O (Aldrich, 99.8 atom % D) and pyridine with pyridine-d_5 (Aldrich, 99 atom % D).

$[Re^{18}O_2(py)_4]BPh_4$: Finely ground K_2ReCl_6 (1.02 g), prepared by the published procedure,[49] and $AgBF_4$ (0.438 g) were mixed with 1 ml $H_2{}^{18}O$ (Merck, Sharp, and Dohme, 97 atom %) in an Ar-filled glove bag. The solution was degassed with five freeze-pump-thaw cycles and 5 ml of dry pyridine was then added to the mixture by flask to flask distillation on the vacuum line. The mixture was refluxed overnight under a static pressure of Ar to yield a red solution and some Ag nuggets. The solvent was stripped off under vacuum and the residue taken up with absolute ethanol (U.S. Industrial Chemical Co.) and filtered. One equivalent of $NaBPh_4$ was added to the filtrate, the white NaCl filtered, and petroleum ether added to precipitate an orange solid. A layer of petroleum ether was vacuum distilled over a solution of 5:1 dry acetone: pyridine containing the complex and allowed to diffuse into the lower layer producing red crystals. Infrared spectra of the natural abundance and ^{18}O samples exhibit antisymmetric rhenium-oxygen stretching vibrations at 815 and 780 cm^{-1}, respectively.

$[ReO_2(4\text{-picoline})_4]BPh_4$: A mixture of K_2ReCl_6 (0.5 g), 4-picoline (ca. 10 ml), and H_2O (ca. 1 ml) was refluxed for 20 hrs. One equivalent of $NaBPh_4$ was added to precipitate an orange solid which was recrystallized from a mixture of water and 4-picoline. Large crystals were grown by diffusion of petroleum ether into a 4:1 acetone:4-picoline

solution containing the complex. Elemental analysis results were: C, 63.25%; H, 5.36%; N, 6.17%. Calculated values were: C, 63.36%; H, 5.32%; N, 6.16%.

[ReO_2(4-t-butylpyridine)$_4$]BPh_4: A mixture of K_2ReCl_6 (0.5 g), 4-t-butylpyridine (6 ml), and H_2O (ca. 1 ml) was refluxed for ca. 12 hours. The solution was heated to boiling to drive off the H_2O and, upon cooling, an orange solid precipitated which was recrystallized from 4-t-butylpyridine and water. The BPh_4^- salt was prepared by mixing [ReO_2(4-t-butylpyridine)$_4$]Cl (95.2 mg) and $NaBPh_4$ (53.25 mg) in a two-phase mixture of 4-t-butylpyridine (5 ml) and water (5 ml) and stirring overnight. The organic layer was then separated and petroleum ether was added to precipitate an orange solid. Crystals were grown by diffusion of petroleum ether into a 4:1 acetone:4-t-butylpyridine solution containing the complex. Elemental analysis results were: C, 66.63%; H, 6.75%; N, 5.18%. Calculated values were: C, 66.84%; H, 6.73%; N, 5.20%.

[$ReO_2(en)_2$]Cl (en = ethylenediamine): The complex was prepared from K_2ReCl_6 by the method of Murmann.[50] Large crystals were grown by evaporation of an aqueous solution containing the complex. The salt was characterized by oscillation and Weissenberg X-ray photographs.[51]

Spectroscopy: All spectroscopic techniques were identical to those described in Chapter Three. Some luminescence lifetimes were measured from Polaroid photographs of oscilloscope traces on a Tektronix model 466 storage oscilloscope. Infrared spectra were recorded on a Beckman model IR4240 spectrometer.

Luminescence Quantum Yields: Absolute luminescence quantum yields were measured by the method of Demas and Crosby.[52] Solutions containing the sample or quantum yield standard were prepared under vacuum in a 10 ml roundbottom flask with a sidearm 1 cm fluorescence cuvette and sealed from the atmosphere by a Kontes quick release teflon stopper. Solutions were rigorously degassed with no fewer than five freeze-pump-thaw cycles. The absorbances of these solutions were less than 0.1 (1 cm path) at the 436 nm excitation wavelength. The quantum yield standard was $[Ru(2,2'\text{-bipyridine})_3]Cl_2$ (Sigma Chemical Co.) in water (NANOpure) which has a reported quantum yield of 0.042 with 436 nm excitation.[53] The quantum yield of the samples was determined from the relation[52]

$$\phi_s = \phi_r \left(\frac{B_r}{B_s}\right)\left(\frac{n_s}{n_r}\right)^2\left(\frac{D_s}{D_r}\right) \qquad (4.1)$$

where the subscripts s and r refer to sample and reference ($[Ru(2,2'\text{-bipyridine})_3]Cl_2$) solutions, respectively, n is the index of refraction of the solvent, and D is the integrated emission intensity. The quantity B is given by

$$B = (1 - 10^{-AL}) \qquad (4.2)$$

where A is the absorbance at the excitation wavelength and L is the pathlength.

Stern-Volmer Quenching: Investigations of bimolecular photochemical reactivity were performed by the Stern-Volmer quenching method.[54] Luminescence quenching was monitored by steady-state or time-

resolved emission measurements. Data were fit to the Stern-Volmer relation[54]

$$\frac{\phi_{em,o}}{\phi_{em}(Q)} = \frac{\tau_o}{\tau(Q)} = 1 + k_q \tau_o [Q] \qquad (4.3)$$

where $\phi_{em,o}$ and τ_o are the luminescence quantum yield and lifetime, respectively, in the absence of quencher, $\phi_{em}(Q)$ and $\tau(Q)$ are the quantum yield and lifetime at quencher concentration [Q], and k_q is the bimolecular quenching rate constant. The equivalence between steady-state and time-resolved experiments implied by equation (4.3) is valid only if no static quenching (i.e., ground state complex formation between emitter and quencher) mechanism is active. Lifetime measurements, therefore, provide a more direct probe of excited state reactivity and were generally chosen over their steady-state counterparts. Samples were prepared in a vessel similar to that used in quantum yield experiments but which was connected to the vacuum line via a U tube in which samples could be degassed with freeze-pump-thaw cycles in the case of liquid quenchers or dynamic vacuum in the case of solids. Once degassed, liquid quenchers were distilled into the 10 ml roundbottom flask and solids were rinsed into the flask with solvent distilled from the sample solution. Solid quenchers were measured by weight and a 20 μl Hamilton syringe was used to deliver aliquots of liquid quenchers. Liquid quenchers were stored under a static pressure of Ar gas and removed against an Ar flow. All lifetimes were measured with 532 nm laser excitation.

Quenchers: The following chemicals were used in luminescence quenching experiments. Water was obtained from house deionized water by passage through a Barnstead NANOpure water purifying system. Methanol from Burdick and Jackson was refluxed over sodium metal and distilled. Methanol tended to break roundbottom flasks when thawed so, rather than freezing in liquid nitrogen, the solvent was repeatedly cooled in a dry ice/acetone slurry, evacuated, and warmed to room temperature. Similarly, methanol was transferred under vacuum by flask to flask distillation by cooling the receiving flask in a dry ice/acetone bath. Absolute ethanol (U.S. Industrial Chemical Co.), D_2O (Aldrich, 99.8 + atom % D), CH_3OD (Aldrich, 99.5 + atom % D), C_2H_5OD (Aldrich, 99.5 + atom % D), and CD_3OD (Aldrich, 99.5 + atom % D) were all used without further purification. Triphenylphosphine, PPh_3 (Aldrich, 99%), was recrystallized three times from absolute ethanol under an Ar atmosphere. Triphenylphosphite, $P(OPh)_3$ (Aldrich, 97%) was stirred over sodium metal under Ar for one day then twice fractionally distilled under vacuum at ca. 155°C and stored under Ar. Alternatively, $P(OPh)_3$ was dissolved in diethyl ether, passed down activated alumina and silica gel columns, and stirred over CaH_2 for two days. The ether was then removed by vacuum and the compound twice vacuum fractionally distilled (ca. 155°C), then sublimed to yield a white solid at room temperature. Triisopropylphosphite, $P(OCH(CH_3)_2)_3$ (Aldrich, 90%), was stirred over sodium metal under an Ar atmosphere for four hours then vacuum distilled from sodium metal at ca. 31°C. Mesityl oxide, $(CH_3)_2CCHCO(OCH_3)$ (practical grade from Eastman), was fractionally distilled under Ar

at 128-130° C and stored under Ar. Ethyl methacrylate, $H_2CC(CH_3)CO(OC_2H_5)$ (Rohm and Haas), was twice fractionally distilled under Ar at 117-118° C and stored under Ar. Diethyl maleate, $(C_2H_5O)OCCHCHCO(OC_2H_5)$ (Aldrich, 80%), was twice vacuum fractionally distilled at ca. 80° C and stored under Ar. Pyridinium tetraphenylborate, $(pyH)(BPh_4)$ was prepared by addition of an aqueous solution of $NaBPh_4$ to a mixture of 5 ml pyridine and 5 ml concentrated HCl. The white solid that precipitated was filtered, washed with water, and air dried. The compound was recrystallized from an acetone/light petroleum ether mixture.

Steady-State Irradiation: Steady-state irradiations were performed with an Oriel 1,000 W Hg/Xe lamp or a 450 W high pressure Hg lamp. High energy radiation was eliminated with Corning glass cutoff filters. Samples were prepared under vacuum in a 10 ml roundbottom flask with a sidearm fluorescence cuvette and sealed from the atmosphere with a Kontes quick release teflon stopper. In one instance, a sample was irradiated in a flame sealed evacuated quartz EPR tube.

C. Results

1. Spectroscopy

The room temperature electronic absorption spectra of three dioxorhenium ions, $ReO_2(en)_2^+$, $ReO_2(py)_4^+$, and $ReO_2(CN)_4^{3-}$, are shown in Figures 4.1 through 4.3. The spectra are very similar at wavelengths longer than 400 nm being characterized by a band maximizing between 400 and 450 nm with a less intense shoulder on the low energy side. The 400 nm band is relatively weak in the cyanide and

Figure 4.1. Single crystal polarized electronic absorption spectra of $[ReO_2(en)_2]Cl$ at ambient temperature. (a) Electric field vector of the incident light oriented perpendicular to the crystal needle axis. (b) Parallel orientation of electric field and the crystal needle axis.

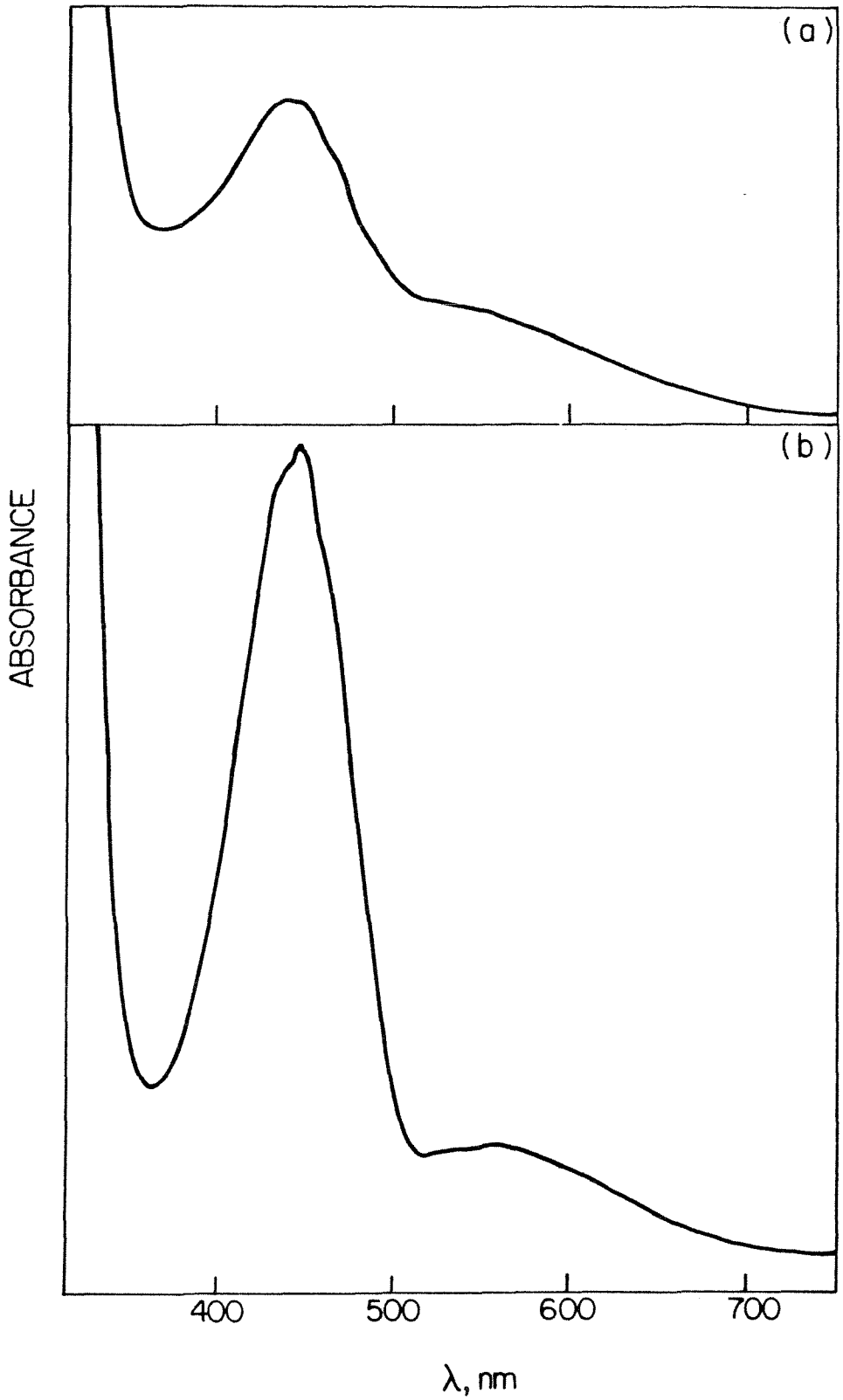
(a)
(b)
ABSORBANCE
400
500
600
700
λ, nm

Figure 4.2. Electronic spectrum of $[ReO_2(py)_4]BPh_4$ in CH_2Cl_2 at ambient temperature.

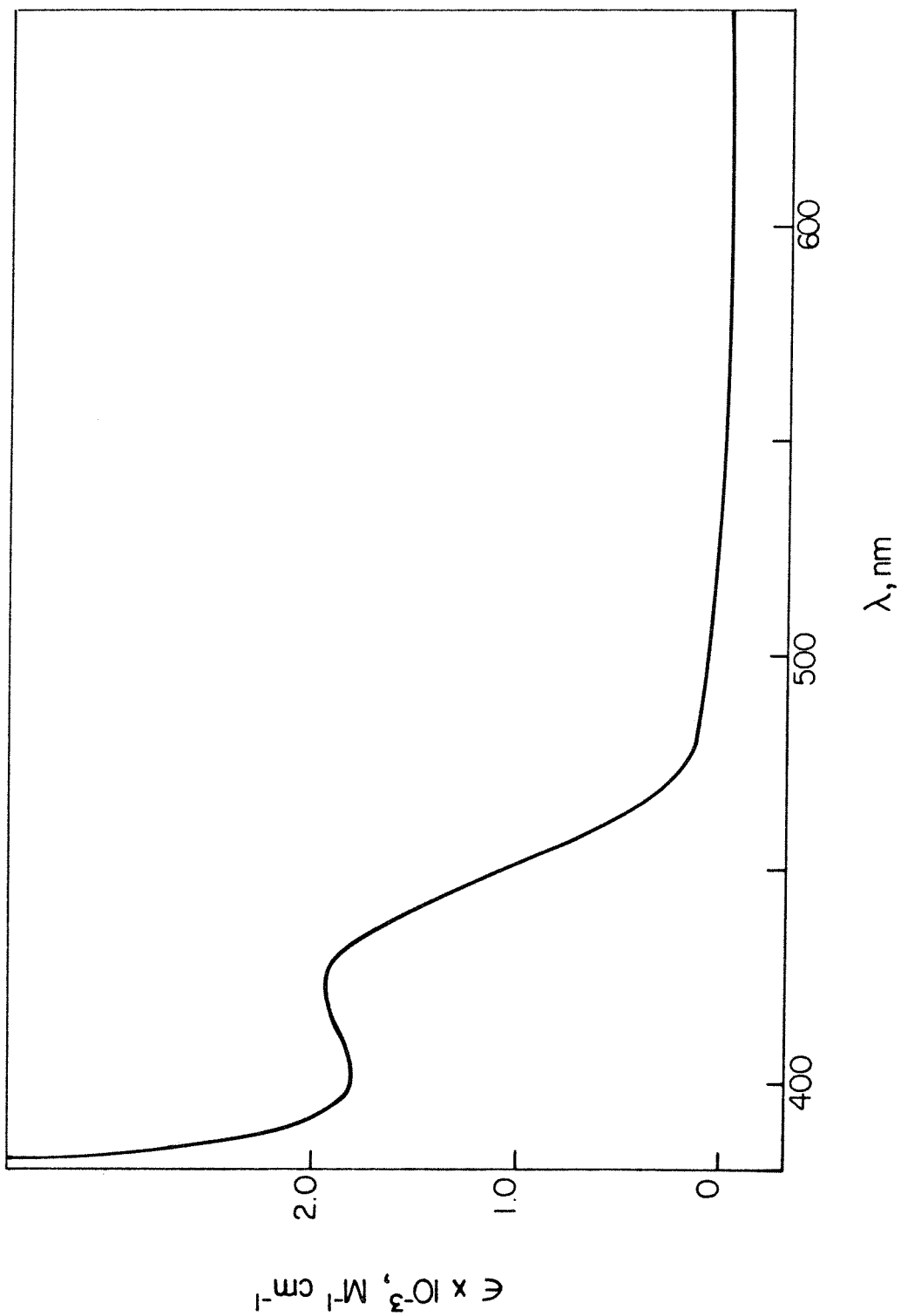
ε x 10⁻³, M⁻¹ cm⁻¹
2.0
1.0
0
400
500
600
λ, nm

Figure 4.3. Single crystal electronic absorption spectrum of $K_3ReO_2(CN)_4$ at ambient temperature.

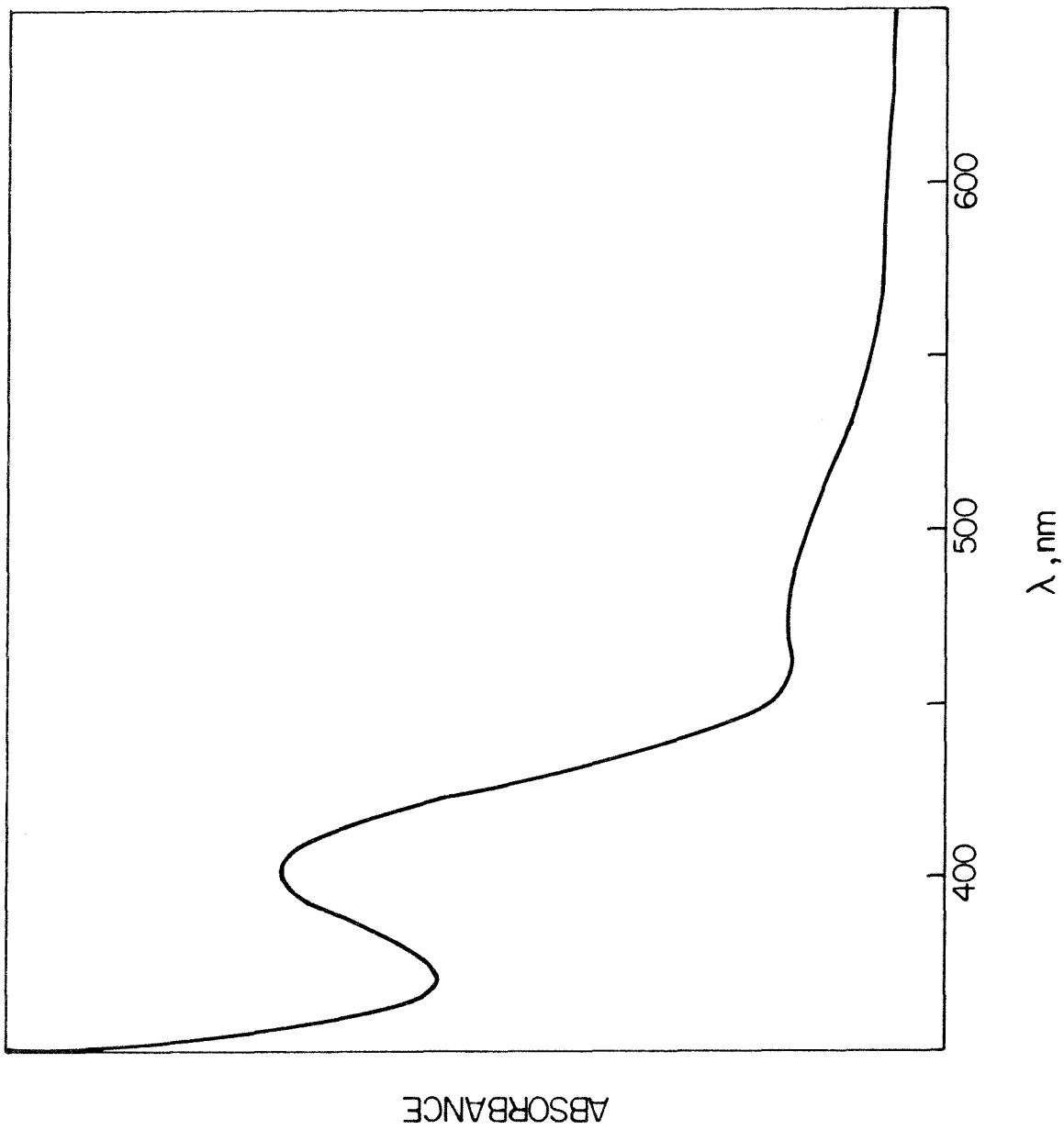
ABSORBANCE
400
500
600
λ, nm

ethylenediamine complexes ($\epsilon \leq 50\ M^{-1}\ cm^{-1}$) but is considerably more intense in the pyridine complex ($\epsilon \sim 1,200\ M^{-1}\ cm^{-1}$). A great deal more information about the electronic structures of these dioxorhenium ions is provided by their low temperature absorption spectra and the luminescence spectra and lifetimes of the cyanide and pyridine complexes.

The 30K polarized electronic absorption spectra of a $[ReO_2(en)_2]Cl$ crystal are reproduced in Figure 4.4. The monoclinic crystals of this complex grow as needles, the axis of which is roughly parallel to the crystallographic a axis.[51] The spectrum recorded with the electric field vector of the incident light oriented perpendicular to the needle axis is labelled 4.4a while Figure 4.4b corresponds to the parallel orientation of the electric field and the needle axis. Three distinct absorption systems appear in these spectra (labelled I, II, and III) though band I is too intense to be resolved in the parallel polarization. Band I maximizes at a wavelength shorter than 320 nm and progresses in a ca. 800 cm^{-1} mode. Band II, which corresponds to the 440 nm absorption maximum in Figure 4.1, is much less intense than band I and, in the perpendicular polarization, displays progressions in modes of 800 and 225 cm^{-1}. Peak maxima and separations are listed in Table 4.1. In the parallel polarization, a new set of peaks appears in band II, the lowest energy component of which is labelled B. These peaks lie approximately 220 cm^{-1} to the red of the first components of the 225 cm^{-1} progression (the lowest energy member is labelled A) found in the perpendicular polarization, but their different polarization demonstrates that they do not, in fact, belong to this progression.

Figure 4.4. Single crystal polarized electronic absorption spectra of $[ReO_2(en)_2]Cl$ at 30 K. (a) Perpendicular orientation of the electric field of the incident light and the crystal needle axis. (b) Parallel orientation of electric field and needle axis.

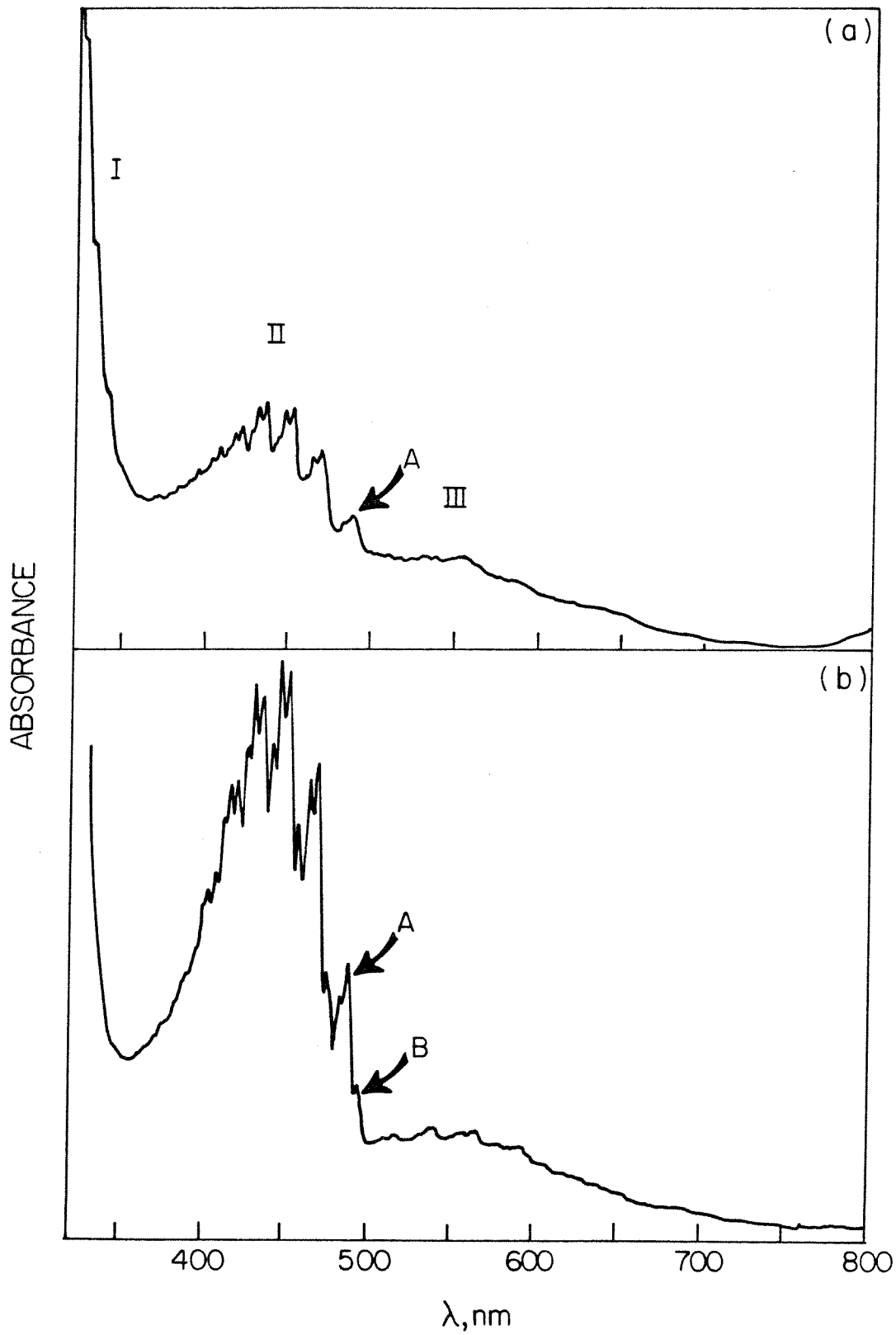
(a)
I
II
A
III
(b)
A
B
ABSORBANCE
400
500
600
700
800
λ,nm

Table 4.1. Vibronic peak maxima and spacings of band II in the 30 K absorption spectrum of $[ReO_2(en)_2]Cl$, perpendicular polarization.

λ_{max}, nm[a]	$\tilde{\nu}$, cm^{-1}	Energy Separations, cm^{-1}		
A 489.9	20,412			
		241		
484.2	20,653			
				824
470.9	21,236			
		228		
465.9	21,464			
		237		
460.8	21,701			810
453.6	22,046			
		231		
448.9	22,277			
		230		
444.3	22,507			801
437.7	22,847			
		226		
433.4	23,073			
		226		
429.2	23,299			799
422.9	23,646			
		232		
418.8	23,878			
		230		
414.8	24,108			798
409.1	24,444			
		229		
405.3	24,673			
		234		
401.5	24,907			

a. Uncertainties are ±0.2 nm.

Peaks A and B, therefore, probably correspond to vibronic origins for band II. Though band II is less intense in the perpendicular polarization on this crystal face, it is not so on other crystal faces (corresponding to rotations about the needle axis) and the spectrum of $[ReO_2(en)_2]Cl$ in a KCl disk more closely resembles Figure 4.4a. The progressions built on vibronic origin B are, therefore, much less intense than those built on A. Finally, the low energy shoulder of the room temperature spectrum in Figure 4.1 resolves into band III at low temperature which exhibits a progression in an 800 cm^{-1} mode. Band III, however, is very complex and extends from 500 nm to beyond 650 nm. Significantly, no luminescence was detected from the $[ReO_2(en)_2]^+$ ion in either the solid state or aqueous solution.

The single crystal polarized electronic absorption spectra of $[ReO_2(py)_4]BPh_4$ at 30 K are shown in Figure 4.5. The crystals grow as prismatic needles and the spectrum in Figure 4.5a corresponds to the parallel orientation of the needle axis and the electric field vector of the incident light while Figure 4.5b represents the perpendicular orientation. The 420 nm band in the room temperature spectrum (Figure 4.2) is too intense to be observed at low temperature in a crystal but the low energy shoulder resolves into a discrete, highly structured absorption profile (band III) with a maximum near 500 nm. Band III in the parallel polarization is composed of a 780 cm^{-1} vibrational progression subdivided by vibronic maxima with 160 to 180 cm^{-1} separations. The more closely spaced peaks do not correspond to a ca. 170 cm^{-1} progression, however, because they exhibit disparate polarization behavior and their relative intensities

Figure 4.5. Single crystal polarized electronic absorption spectra of $[ReO_2(py)_4]BPh_4$ at 30 K. (a) Parallel orientation of electric field and crystal needle axis. (b) Perpendicular orientation of electric field and crystal needle axis.

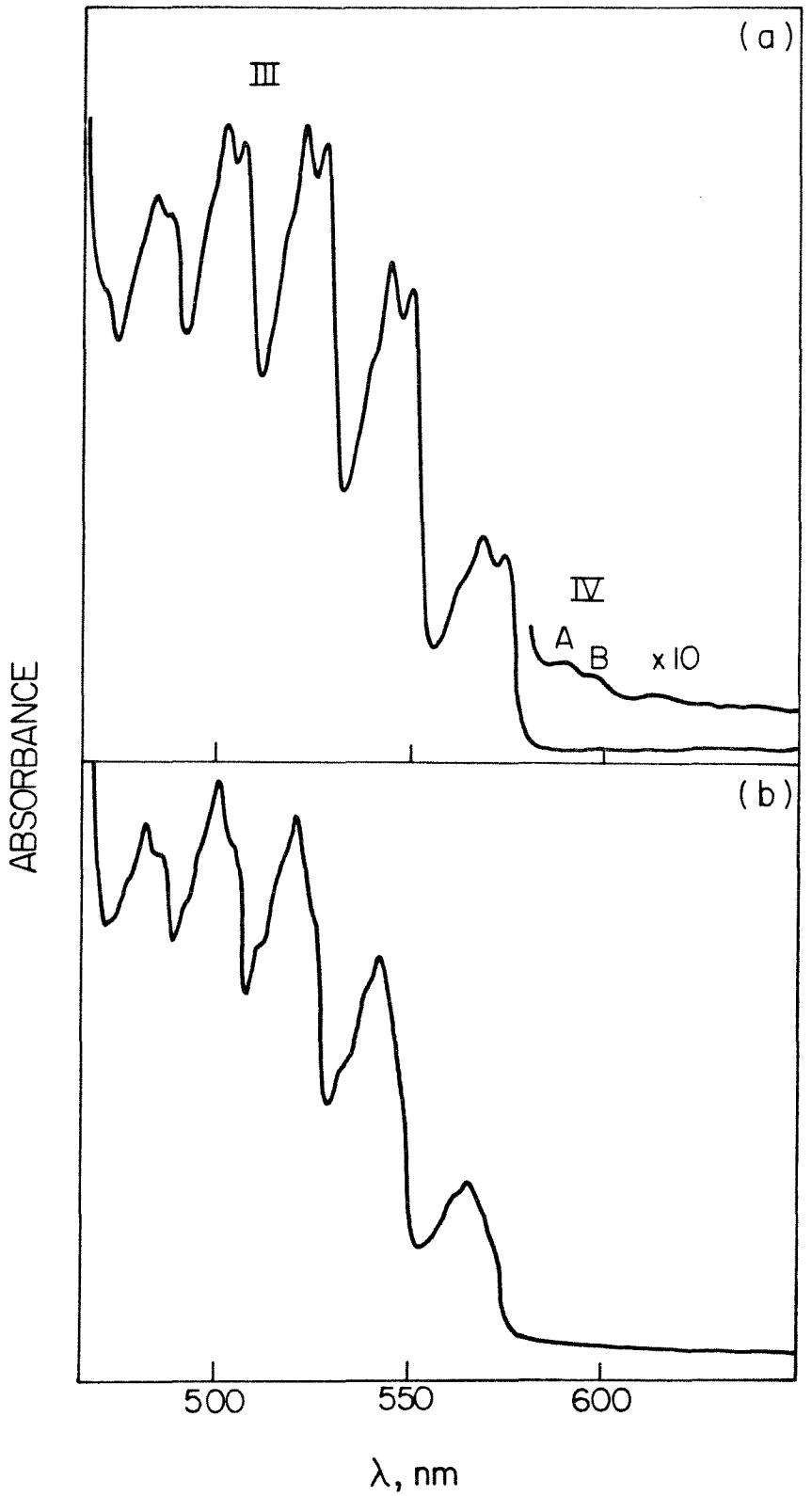
(a)
III
IV
A
B
x10
(b)
ABSORBANCE
500
550
600
λ, nm

are not commensurate with a harmonic Franck-Condon progression (Appendix 1). In addition, two very small features that comprise band system IV appear at 590.1 and 597.1 nm, but they have neither the proper energy spacings nor intensities to be components of the progressions in band III. Peak maxima and energy spacings for bands III and IV are listed in Table 4.2.

Further insight into the $[ReO_2(py)_4]BPh_4$ electronic structure is provided by its low temperature luminescence spectrum (Figure 4.6). In contrast to the absorption spectrum, the 4.5 K emission spectrum is particularly straightforward, consisting of one 900 cm^{-1} and one 190 cm^{-1} vibrational progression (peak positions are outlined in Table 4.3). The highest energy <u>real</u> feature that can be discerned in the luminescence spectrum of this complex is probably the shoulder on the high energy edge of peak O′, labelled O in Figure 4.7. Comparison with the origin region of the absorption spectrum (inset in Figure 4.5a) suggests that this shoulder at 16678(10) cm^{-1} (599.6(2) nm) is the electronic origin for the emission band and for part of absorption system IV. This assignment derives primarily from the symmetrical disposition of O 269(10) cm^{-1} from peak A in absorption and 268(10) cm^{-1} from peak A′ in emission. Furthermore, the highest energy feature in the 4.5 K emission spectrum of $[ReO_2(py\text{-}d_5)_4]BPh_4$ is a shoulder analogous to O. The peaks A and A′ must correspond to vibronic origins built on the pure electronic origin O. It is, of course, possible that peak O′ or O″ in Figure 4.7 corresponds to the true origin but the mirror symmetry about the shoulder O strongly supports its assignment to the origin. Upon warming to 30 K, the emission spectrum of

Table 4.2. Vibronic peak maxima and spacings of bands III and IV in the 30 K absorption spectrum of $[ReO_2(py)_4]BPh_4$, parallel polarization.

	λ_{max}, nm[a]	$\tilde{\nu}$, cm^{-1}	Energy separations, cm^{-1}		
IV B	597.1	16,748			
IV A	590.1	16,946			
	573.9	17,425			
			174		
	568.2	17,599			
			182		
	562.4	17,781			783
	549.2	18,208			
			178		
	543.9	18,386			
			167		
	539.0	18,553			778
III					
	526.7	18,986			
			178		
	521.8	19,164			
			167		
	517.3	19,331			781
	505.9	19,767			
			181		
	501.3	19,948			
			161		
	497.3	20,109			775
	486.8	20,542			
			162		
	483.0	20,704			

a. Uncertainties are ±0.2 nm.

Figure 4.6. Luminescence spectrum of crystalline $[ReO_2(py)_4]BPh_4$ at 5 K recorded with 436 nm excitation. Not corrected for spectrometer response.

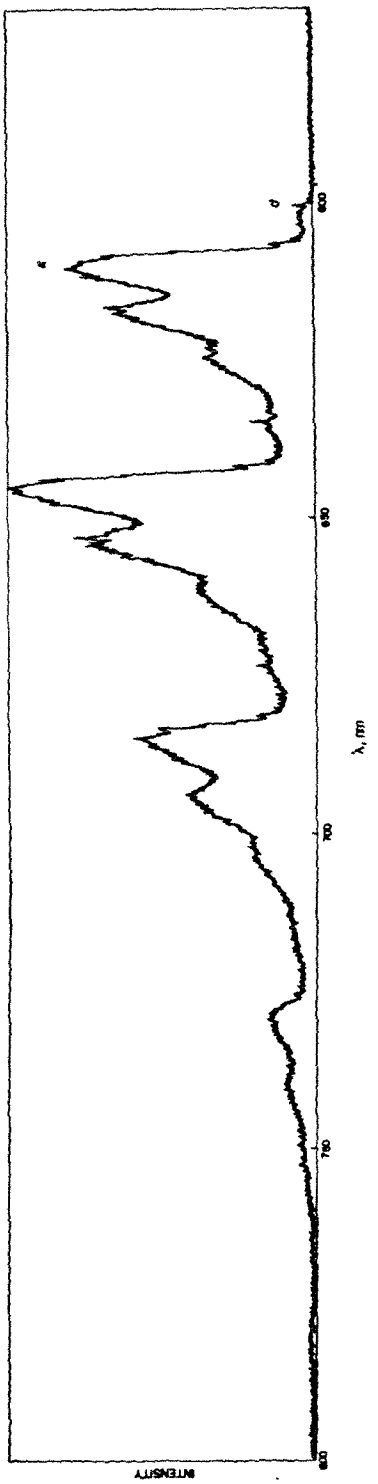
INTENSITY
600
650
700
750
800
λ, nm

Table 4.3. Vibronic peak maxima and energy spacings in the 5 K luminescence spectrum of $[ReO_2(py)_4]BPh_4$.

λ_{max}, nm[a]	$\tilde{\nu}$, cm^{-1}	Energy separations, cm^{-1}		
A′ 609.4	16,410			
		192		
616.6	16,218			
		187		
623.8	16,031			907
645.0	15,503			
		185		
652.8	15,318			
		189		
661.0	15,129			897
684.6	14,606			
		189		
693.6	14,417			
		192		
703.0	14,225			937
731.6	13,669			
		150		
739.7	13,519			

a. Uncertainties are ±0.2 nm.

Figure 4.7. Origin region of the luminescence spectrum of crystalline $[ReO_2(py)_4]BPh_4$ at 5 K recorded with 436 nm excitation. Not corrected for spectrometer response.

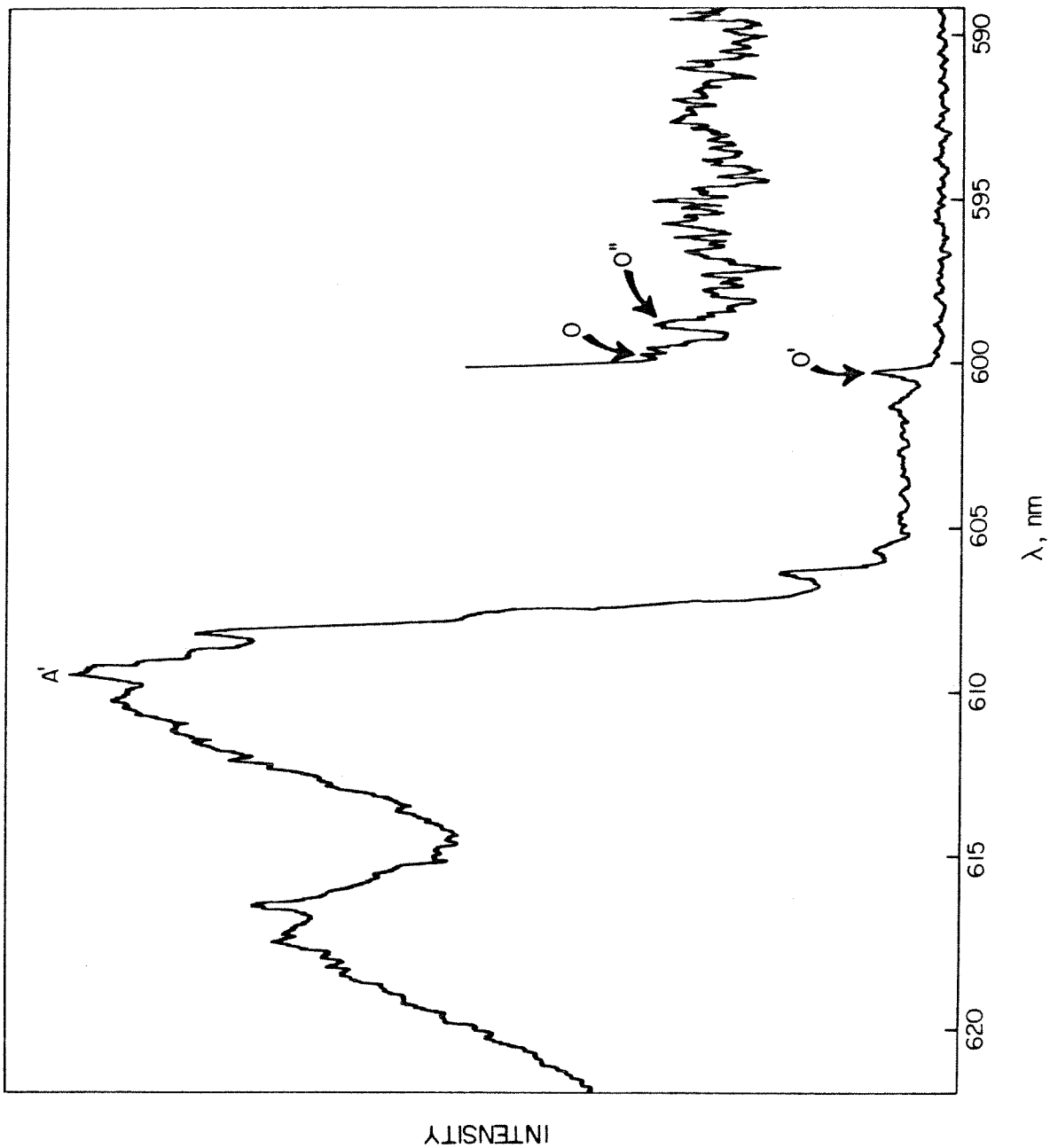
A'
O
O"
O'
590
595
600
605
610
615
620
λ, nm
INTENSITY

$[ReO_2(py)_4]BPh_4$ changes dramatically as shown in Figure 4.8. A new set of peaks resolves, the highest energy component of which is peak B′ at 16,628(10) cm^{-1}. This feature is very analogous to peak B in the absorption spectrum. The fact that B′ appears only at elevated temperatures implies that it corresponds to a state that becomes thermally accessible upon warming from 5 to 30K. Peaks B and B′ would then correspond to vibronic origins of this higher energy state. The position of the pure electronic origin of this second state can be estimated by assuming the vibronic promoting mode that gives rise to peaks B and B′ has the same energy in the ground and excited states. The origin of the second state, then, should lie halfway between B and B′ near 16,688 cm^{-1}, or approximately 10 cm^{-1} higher energy than O. This energy separation is certainly consistent with its thermal population at 30K. Finally, the assignment of peaks A and B in the absorption spectrum of $[ReO_2(py)_4]BPh_4$ to vibronic origins of the two luminescent states demonstrates that band III must correspond to yet another electronic excited state(s) with an origin near 17,200 cm^{-1} ($\sim$581 nm) or about 500 cm^{-1} above O.

Unlike its emission spectrum, the luminescence lifetime of $[ReO_2(py)_4]BPh_4$ does not significantly vary between 5 and 30K (Figure 4.9). At 5K the emission lifetime is about 68 μs and remains so until about 70K whereupon it gradually increases to its room temperature value of 30 μs. If the analysis of the absorption and emission spectra in terms of two closely spaced (ca. 10 cm^{-1}) electronic states is correct then the thermal behavior in Figure 4.9 implies that the two emitting states have nearly identical decay rates.

Figure 4.8. Luminescence spectrum of crystalline $[ReO_2(py)_4]BPh_4$ at 30 K recorded with 436 nm excitation.

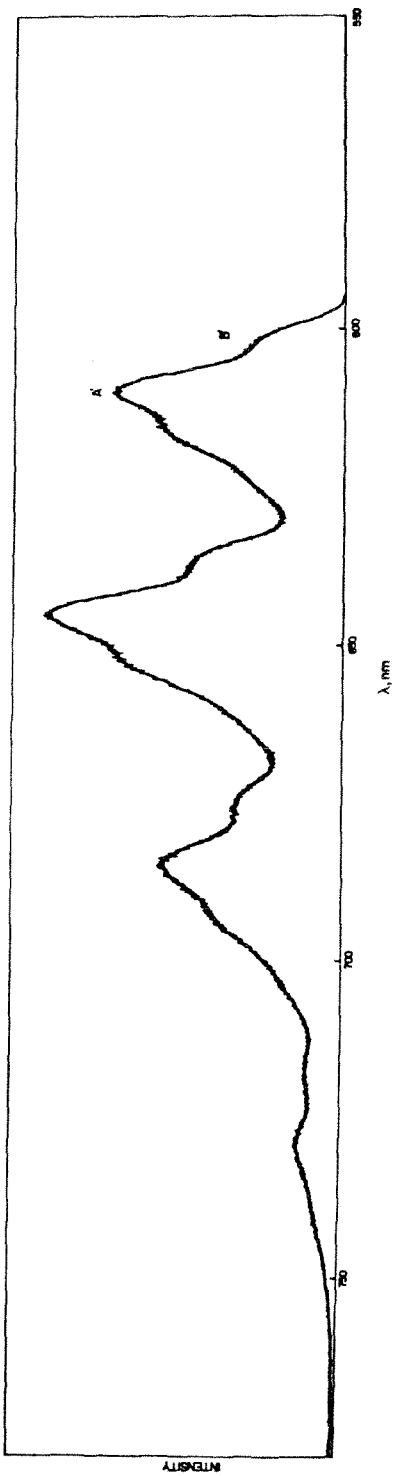
INTENSITY
750
700
650
600
550
λ, nm
A
B

Figure 4.9. Variation in the luminescence decay rate of $[ReO_2(py)_4]BPh_4$ as a function of temperature between 5 and 300 K.

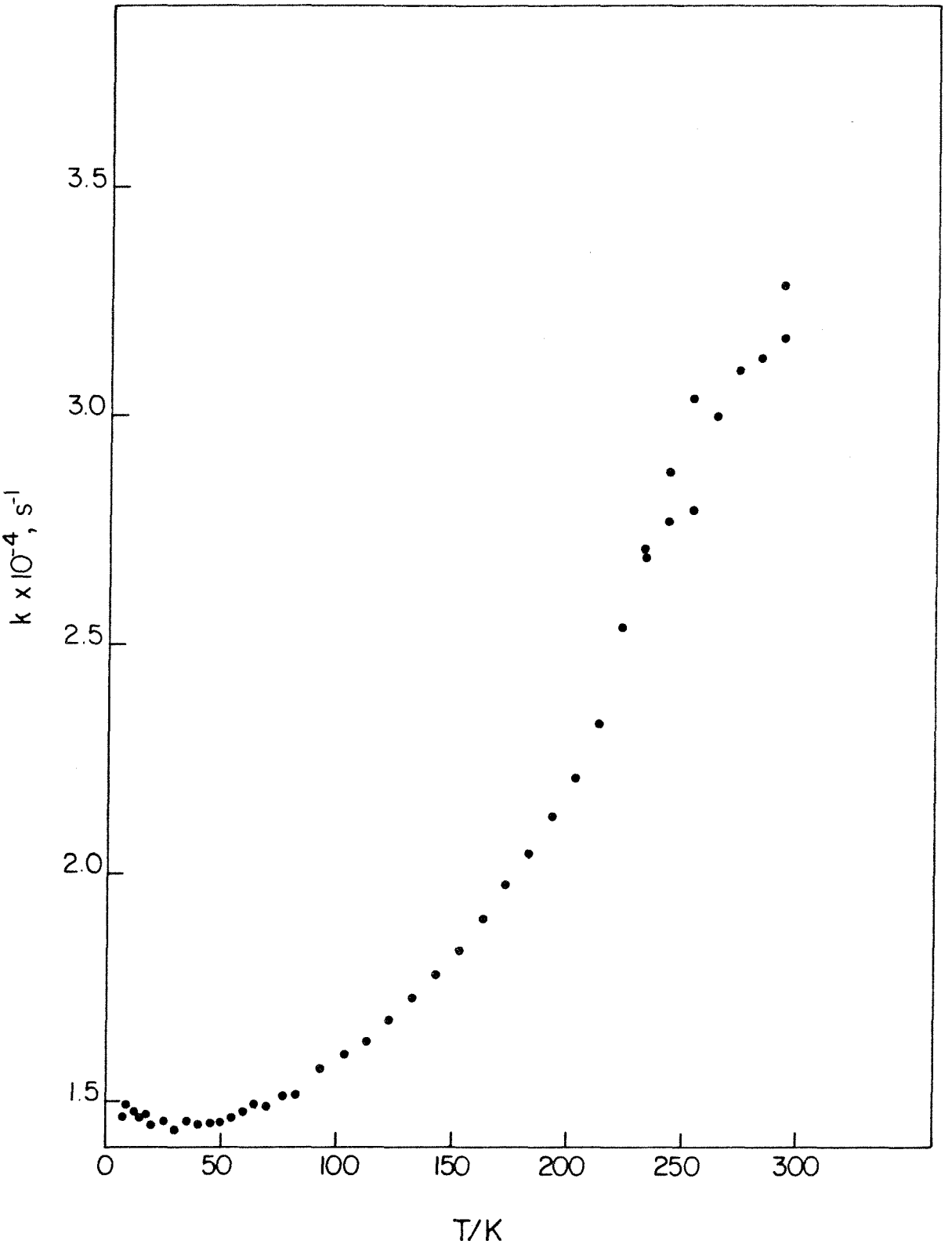
3.5
3.0
2.5
2.0
1.5
k x 10^-4, s^-1
0
50
100
150
200
250
300
T/K

The electronic spectra of the isotopically substituted derivatives $[Re^{18}O_2(py)_4]BPh_4$ and $[ReO_2(py\text{-}d_5)_4]BPh_4$ are qualitatively similar to their natural abundance analogs. The 780 and 900 cm^{-1} progressions in absorption and emission, however, reduce to 740 and 850 cm^{-1}, respectively in the ^{18}O complex. This reduction in frequency by a factor of 0.95(1) upon ^{18}O substitution is consistent with a symmetric O-Re-O stretching vibration where the theoretical reduction factor is 0.94. The vibronic features in the pyridine-d_5 complex spectra are sharper and slightly blue shifted relative to their counterparts in the ^1H complex. The lifetimes of these as well as two para-alkyl substituted pyridine species are listed in Table 4.4. Deuteration of the pyridine rings lengthens the excited state lifetime by about a factor of four, para-alkyl substitution reduces it by about a factor of three, and ^{18}O substitution has very little effect.

The low temperature electronic absorption spectrum of a single crystal of $K_3ReO_2(CN)_4$ is particularly complex (Figure 4.10). The spectrum is further complicated by the fact that $K_3ReO_2(CN)_4$ crystallizes in the triclinic space group $P\bar{1}$,[47] which permits the crystal extinction directions to rotate as a function of the wavelength of the incident light.[55] Polarization studies, therefore, become very difficult indeed and few conclusions will be formed on the basis of the polarization of these absorption bands. Figure 4.10 clearly shows three separate absorption bands (I, II, and III) progessing in a high energy (ca. 770 cm^{-1}) mode maximizing near 310, 400, and 470 nm. These spectra are actually more highly structured than indicated in Figure 4.10. A better resolved spectrum in the region of band III is

Table 4.4. Luminescence lifetimes of crystalline dioxorhenium complexes at 300K.

Complex	$\tau, \mu s^a$
$K_3ReO_2(CN)_4$	330(10)
$[ReO_2(py)_4]BPh_4$	32(3)
$[ReO_2(py\text{-}d_5)_4]BPh_4$	140(5)
$[Re^{18}O_2(py)_4]BPh_4$	36(3)
$[ReO_2(4\text{-picoline})_4]BPh_4$	11(2)
$[ReO_2(4\text{-}\underline{t}\text{-butylpyridine})_4)BPh_4$	11(2)

a. Measured with 532 nm excitation.

Figure 4.10. Single crystal electronic absorption spectrum of $K_3ReO_2(CN)_4$ at 5 K.

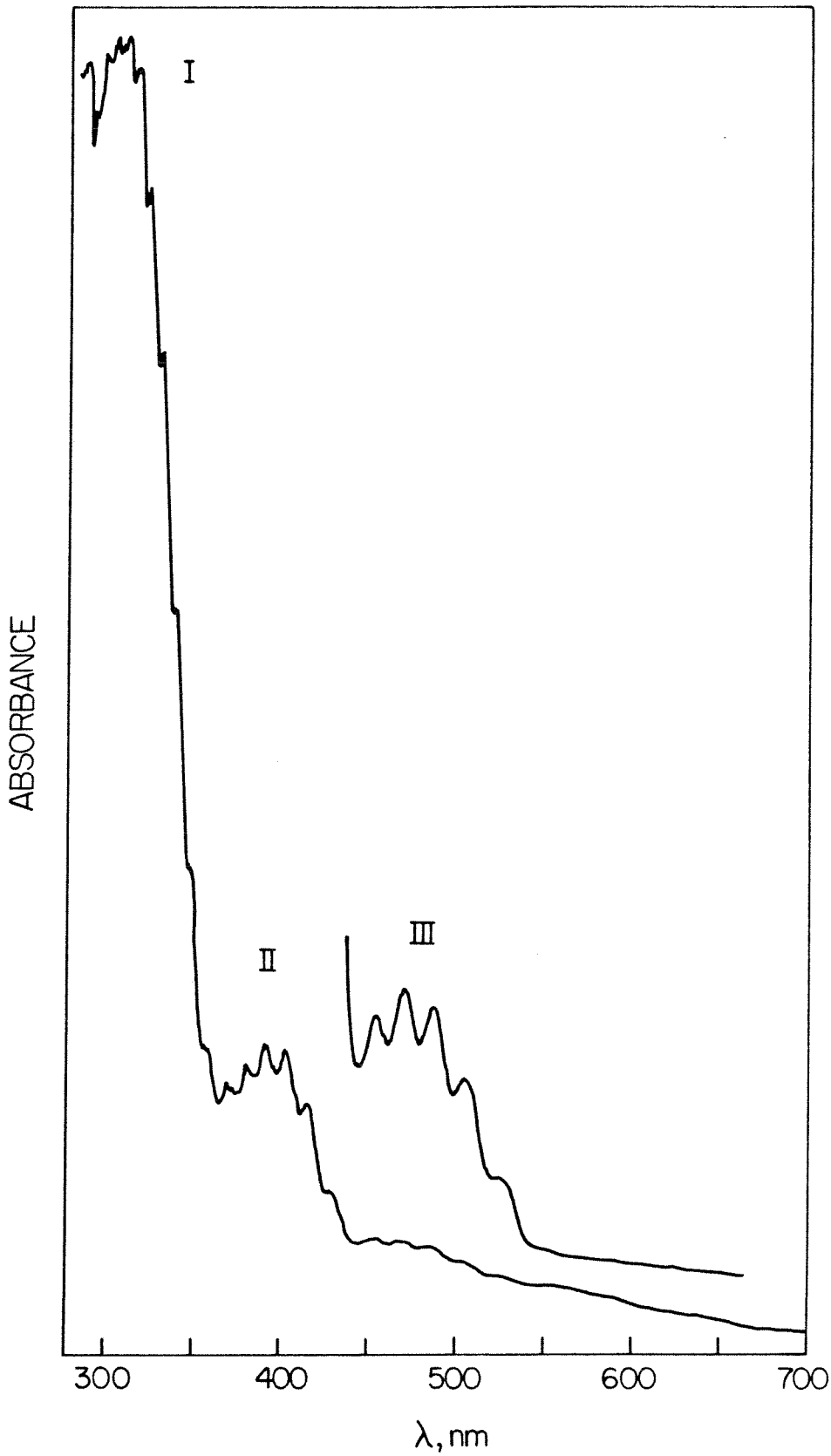
I
II
III
ABSORBANCE
300
400
500
600
700
λ, nm

shown in Figure 4.11 and peak positions are summarized in Table 4.5. Finally, the origin region of band III (520 to 560 nm) is shown in Figure 4.12. The separation and relative intensity of the feature labelled IV in Figure 4.12 demonstrate that it is not a member of the 770 cm^{-1} progression that comprises band III. The absorption spectrum of $K_3ReO_2(CN)_4$, therefore, exhibits four distinct band systems between 300 and 560 nm, three of which progress in a ca. 770 cm^{-1} mode, but none of which display any lower energy progressions.

The luminescence spectrum of $K_3ReO_2(CN)_4$ at 5 K is not a great deal simpler (Figure 4.13). An obvious progression of 870 cm^{-1} resolves at 5 K but within each member of this progression the spectrum is congested with a number of irregularly spaced and structured emission features (Table 4.6). A further complication to this spectrum arises upon warming to 10 K where new and distinct emission features appear (Figure 4.14). It is essentially impossible to understand all of the complex features in these spectra but it is equally impossible to ignore the few very sharp and prominent features in the luminescence spectra and their similarity to features in absorption.

The origin regions of these spectra prove to be most enlightening. The highest energy feature in the 5 K $K_3ReO_2(CN)_4$ emission spectrum (Figure 4.15) is at 17803(10) cm^{-1} (561.7(2) nm, peak O). No corresponding feature at this wavelength can be detected in the absorption spectrum. If peak O is indeed the electronic origin for the 5 K emission band, then the sharp features of the 870 cm^{-1} progression (peaks A′ through E′) are probably vibronic origins built

Figure 4.11. Band III region of the single crystal absorption spectrum of $K_3ReO_2(CN)_4$ at 30 K.

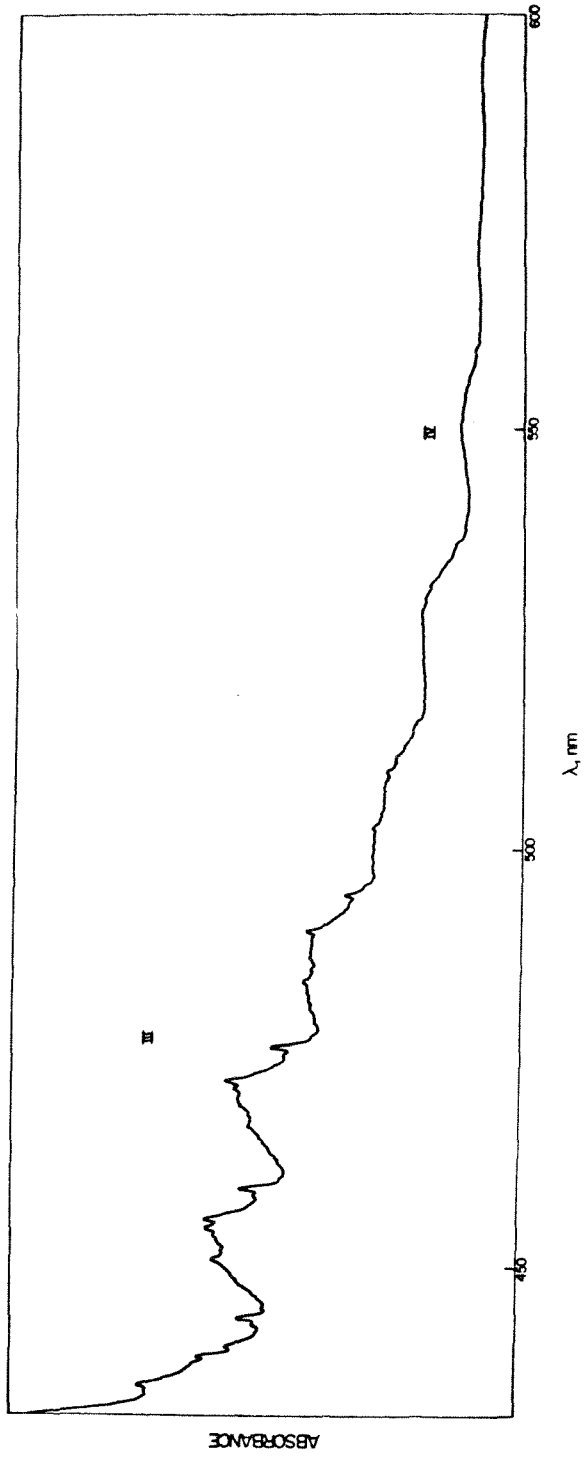
ABSORBANCE
λ, nm
450
500
550
600
II
III

Table 4.5. Vibronic peak maxima and spacings of band III in the 30K absorption spectrum of a $K_3ReO_2(CN)_4$ crystal.

λ_{max}, nm[a]	$\tilde{\nu}$, cm^{-1}	Energy Separations, cm^{-1}
529.9	18,871	
522.4	19,142	768
509.2	19,639	
502.5	19,900	765
494.4	20,227	
490.1	20,404	
484.0	20,661	773
476.2	21,000	
472.2	21,177	
466.8	21,422	767
459.4	21,768	
455.7	21,944	
454.6	22,997	
450.9	22,178	763
443.8	22,533	
440.4	22,707	
439.2	22,769	
435.8	22,946	

a. Uncertainties are ± 0.2 nm.

Figure 4.12. Origin region of the single crystal electronic absorption spectrum of $K_3ReO_2(CN)_4$ at 30 K.

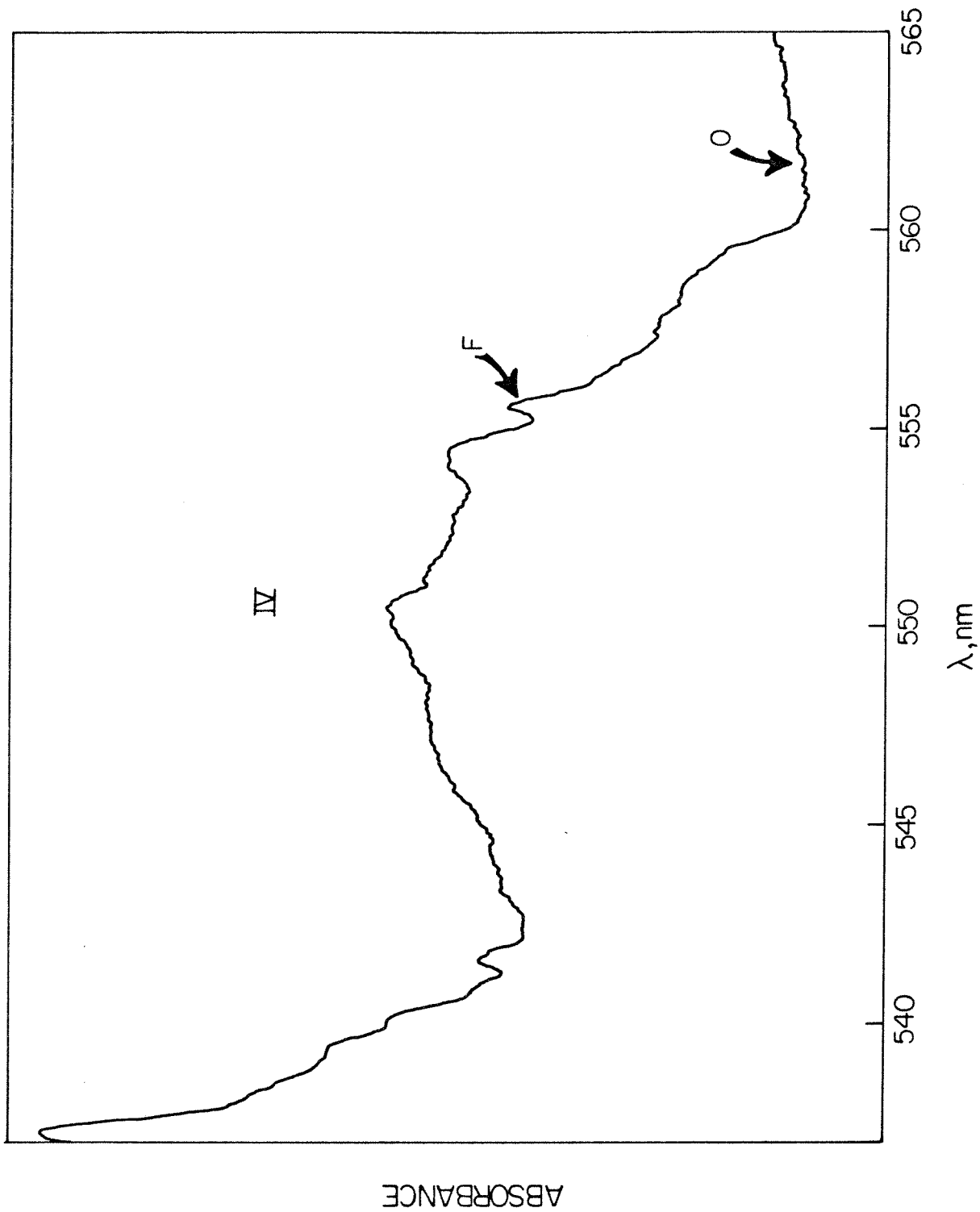
IV
F
O
540
545
550
555
560
565
λ,nm
ABSORBANCE

Figure 4.13. Luminescence spectrum of crystalline $K_3ReO_2(CN)_4$ at 5 K recorded with 436 nm excitation. Not corrected for spectrometer response.

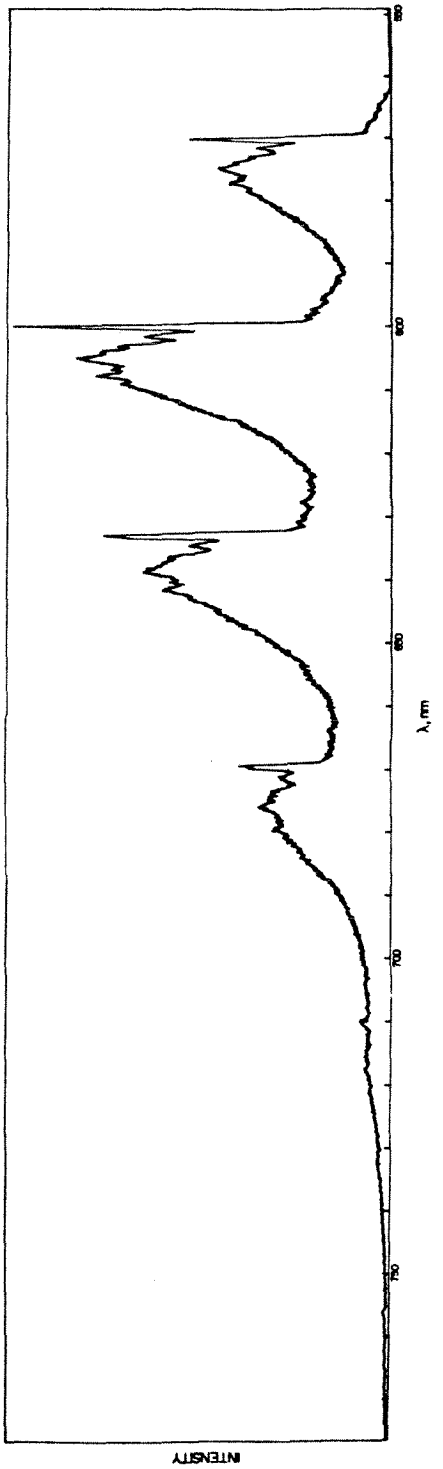
INTENSITY
λ, nm

Table 4.6. Vibronic peak maxima and spacings in the 5 K luminescence spectrum of crystalline $K_3ReO_2(CN)_4$.

	λ_{max}, nm[a]	$\tilde{\nu}$, cm^{-1}	Energy Separations, cm^{-1}
A′	570.1	17,541	
B′	571.4	17,501	
D′	574.7	17,400	872
E′	577.1	17,328	
	599.9	16,669	
	601.5	16,625	
	604.8	16,534	869
	607.7	16,455	
	632.9	15,800	
	634.5	15,760	
	638.7	15,657	857
	641.5	15,588	
	669.2	14,943	
	670.9	14,905	
	675.7	14,799	
	679.2	14,723	

a. Uncertainties are ± 0.2 nm.

Figure 4.14. Luminescence spectrum of crystalline $K_3ReO_2(CN)_4$ at 10 K recorded with 436 nm excitation. Not corrected for spectrometer response.

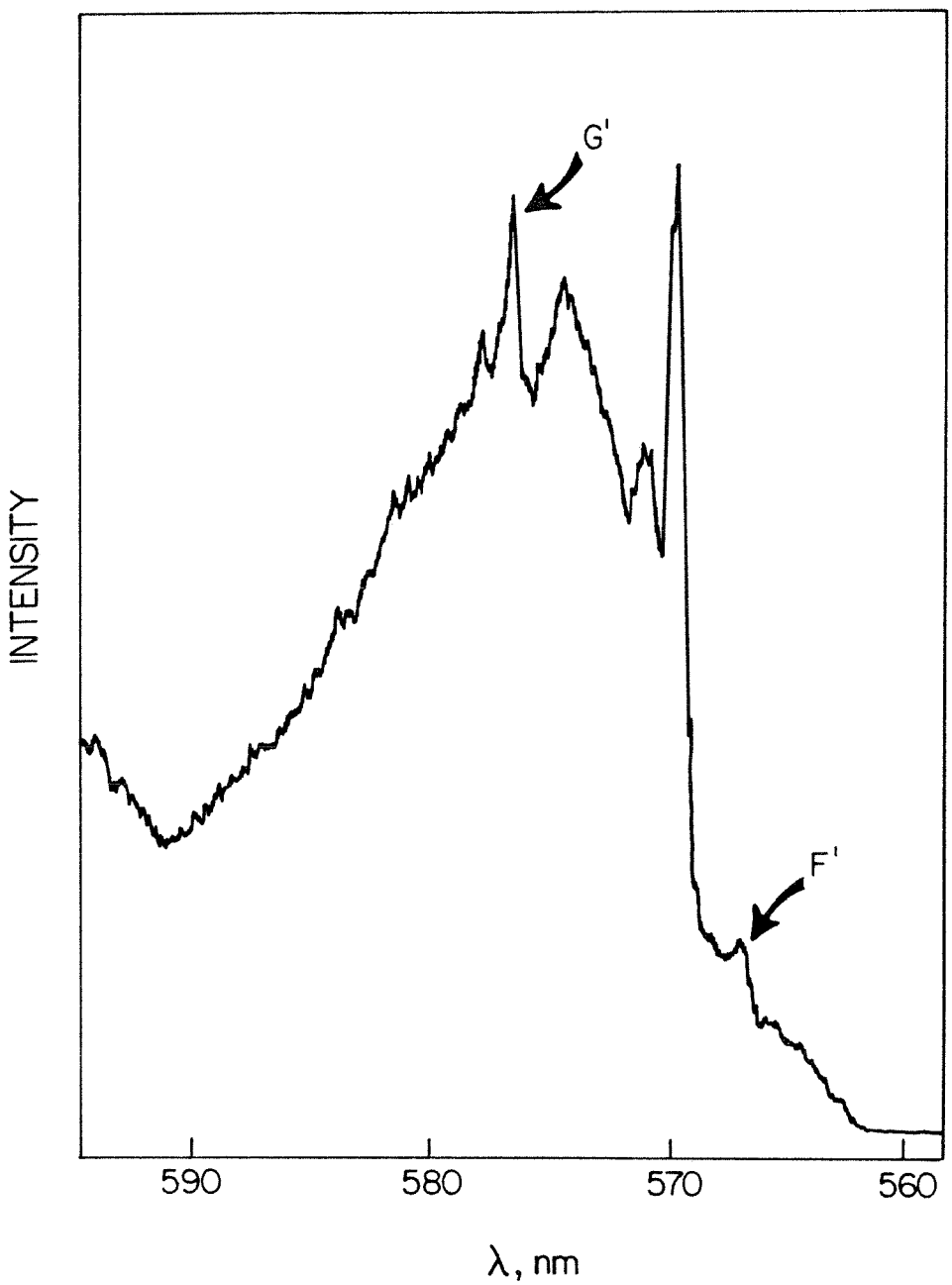
G'
F'
INTENSITY
590
580
570
560
λ, nm

Figure 4.15. Origin region of the luminescence spectrum of $K_3ReO_2(CN)_4$ at 5 K recorded with 436 nm excitation. Not corrected for spectrometer response.

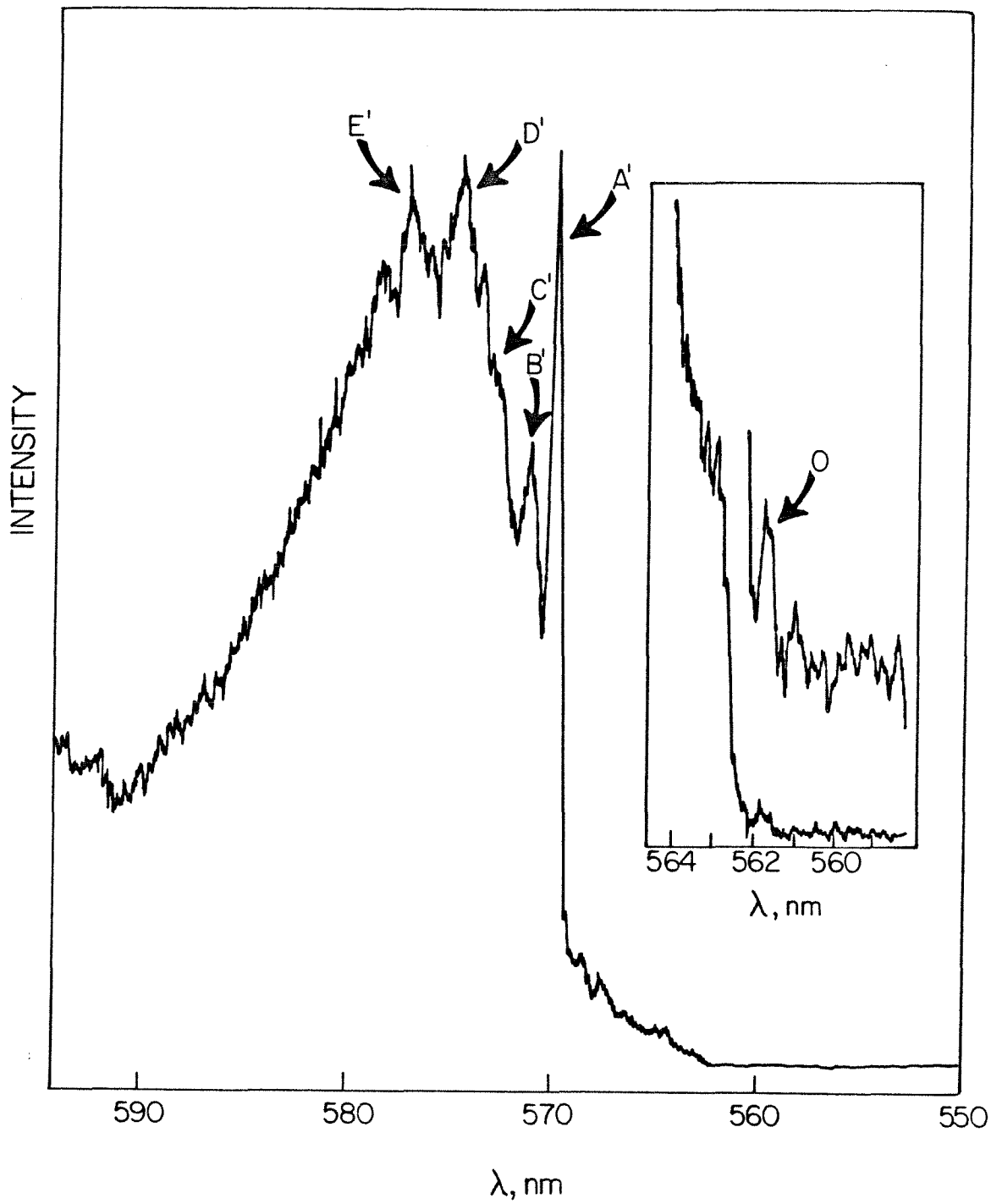
E'
D'
A'
C'
B'
O
INTENSITY
590
580
570
560
550
λ, nm
564
562
560
λ, nm

on O. The energy spacings between these peaks and O correlate very well with a number of features in the infrared spectrum of $K_3ReO_2(CN)_4$ (Figure 4.16, Table 4.7). Another test of the origin assignment for peak O is found in the absorption spectrum and the requirement of mirror symmetry about the origin. Peak O does not fare well in this examination since no counterparts of peaks A′ through E′ are apparent in Figure 4.12. An escape from this trap is provided by the assumption of heavy spectral congestion in the 550 to 560 nm absorption region.

The temperature dependence of the luminescence decay rate tends to support this assumption of a congested origin region in absorption. The variation in k, the inverse of the emission lifetime, as a function of temperature is shown in Figure 4.17. This decay rate increases by about a factor of 2 between 5 and 20 K and new sharp features appear in the emission spectrum at 10 K (Figure 4.14) that are not present at 5 K (Figure 4.13). These data strongly suggest that, as in the pyridine complex, a second electronic state lies just above the lowest energy electronic excited state of $K_3ReO_2(CN)_4$ which can be thermally populated between 5 and 20 K. Additionally, the luminescence intensity increases by about a factor of 1.5 between 5 and 10 K indicating that the change in k is partly a change in the pure radiative decay rate, which implies a greater oscillator strength for the second state. The absorption spectrum, then, should exhibit mirror symmetry with the 10 to 20 K emission spectrum. Below 555 nm, in fact, the spectra are somewhat symmetric and, if peaks F and F′ correspond to vibronic origins in absorption and emission, respectively, then the origin of the second state lies near 17,816 cm^{-1} (561.3 nm) or about 13 cm^{-1} above peak O.

Figure 4.16. Infrared spectrum of $K_3ReO_2(CN)_4$ in a Vaseline mull between CsI plates. A spectrum of just Vaseline between CsI plates is shown in the inset.

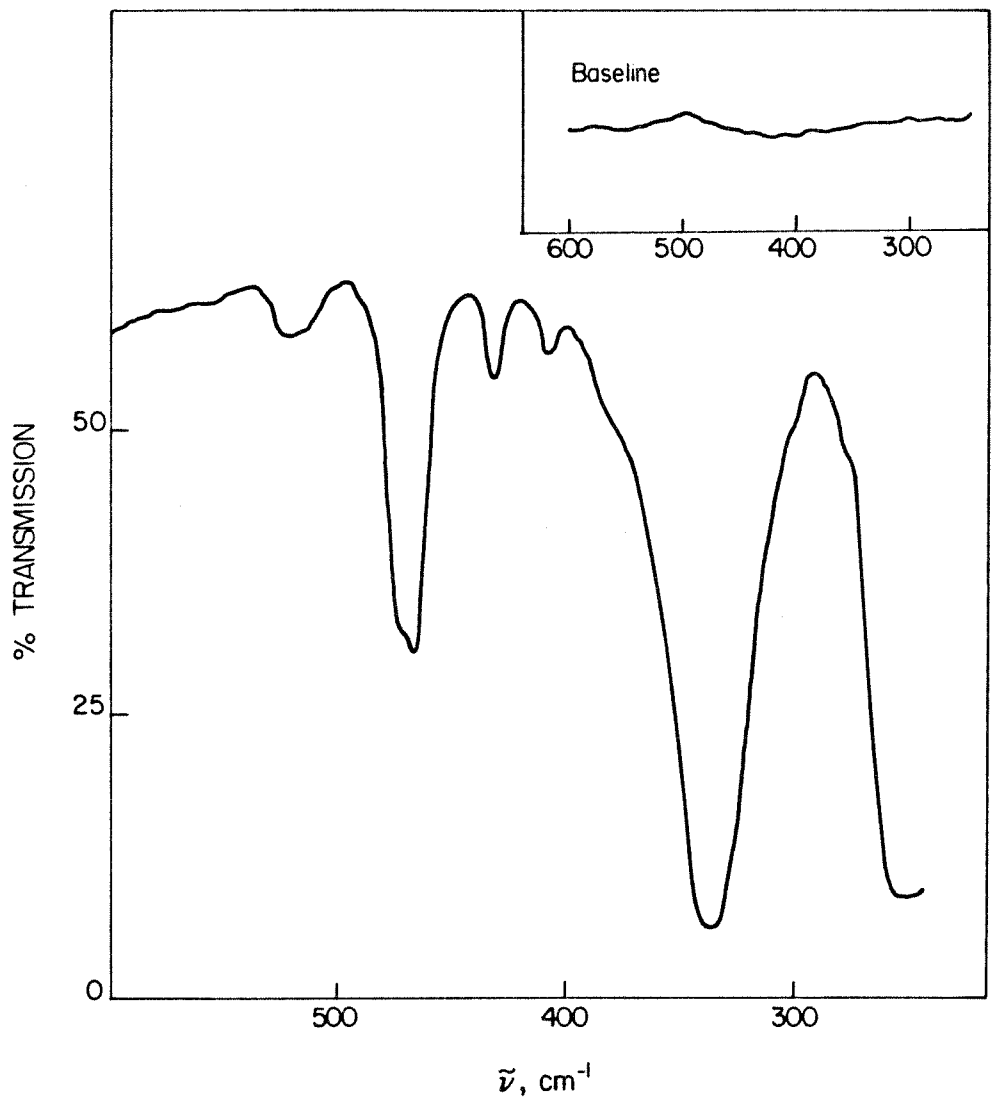
Baseline
600
500
400
300
% TRANSMISSION
50
25
0
500
400
300
$\tilde{\nu}$, cm^{-1}

Table 4.7. Comparison between emission vibronic maxima and peaks in the infrared spectrum of $K_3ReO_2(CN)_4$.

Peak	$\tilde{\nu}$, cm^{-1}	Energy from O, cm^{-1}	IR Peak, cm^{-1}	Assignment[a]
A′	17,541	262(10)	255	
B′	17,501	302(10)	300 sh	
C′	17,461	342(10)	339	δ[b]
D′	17,400	403(10)	411	
E′	17,328	475(10)	469,475	ν(Re-C)

a. By analogy to $Pt(CN)_4^{2-}$, reference 56.

b. In-plane deformation.

Figure 4.17. Variation in luminescence decay rate of $K_3ReO_2(CN)_4$ as a function of temperature between 5 and 300 K.

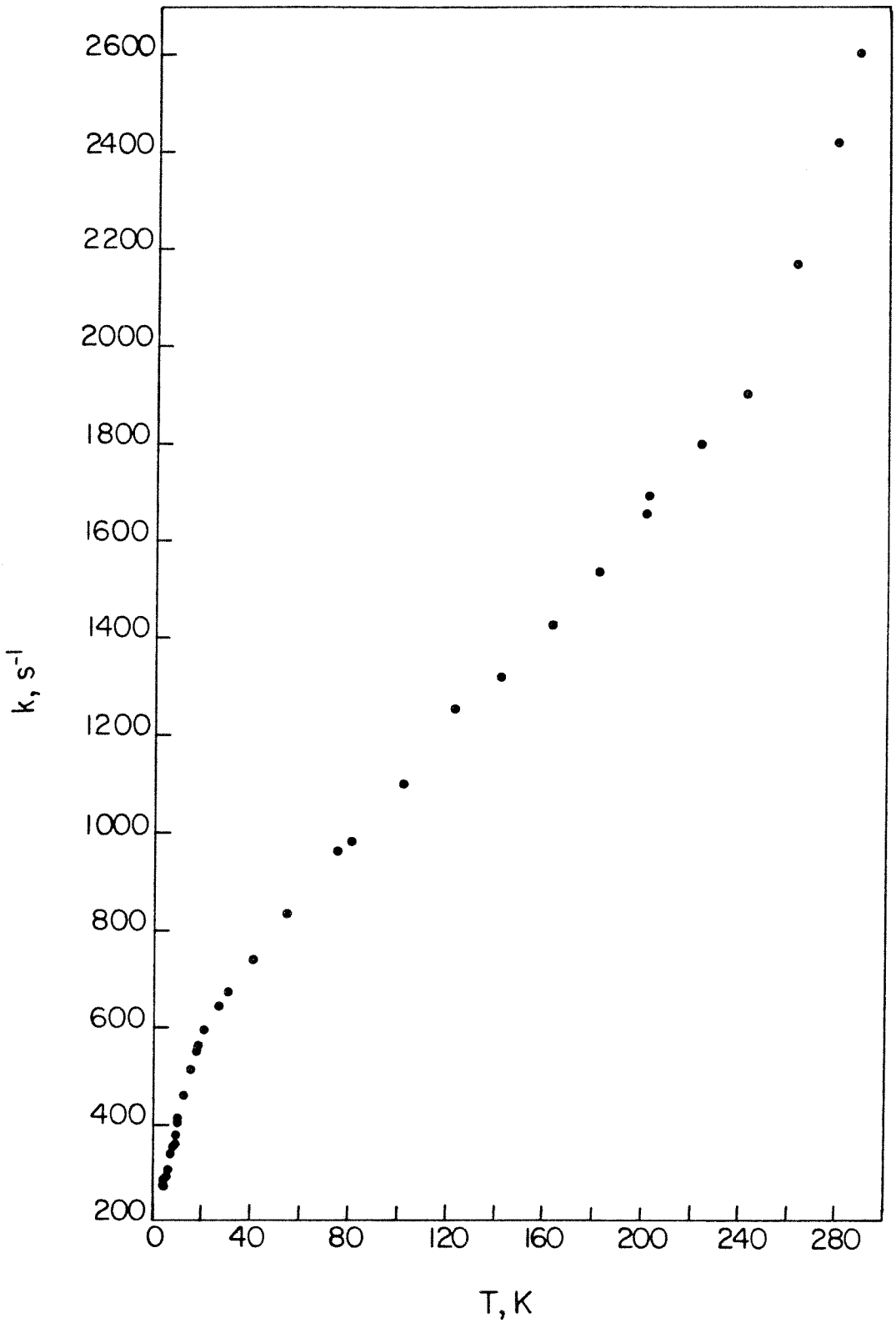
2600
2400
2200
2000
1800
1600
1400
1200
1000
800
600
400
200
k, s⁻¹
0
40
80
120
160
200
240
280
T, K

The peak G′, in fact, lies 477 cm^{-1} below 561.3 nm which agrees closely with the frequency of a peak in the infrared spectrum of $K_3ReO_2(CN)_4$ at 475 cm^{-1} (Figure 4.16). The low temperature lifetime data are fit well by an expression of the form[57]

$$k_{obs} = \frac{k_1 + k_2 \exp(-\Delta E/k_B T)}{1 + \exp(-\Delta E/k_B T)} \qquad (4.4)$$

with $k_1 = 275\ s^{-1}$, $k_2 = 1,500\ s^{-1}$, and $\Delta E = 15\ cm^{-1}$ (Figure 4.18). Equation (4.4) just expresses the observed decay rate for two states in thermal equilibrium that are separated by an energy gap ΔE and have intrinsic decay rates k_1 and k_2. The agreement between ΔE from (4.4) and the value determined from peaks F and F′ is encouraging. The symmetry between absorption and emission is lost at wavelengths shorter than 555 nm and it is likely that intereference from the origin of band III is responsible. It is also possible that the state giving rise to band III in absorption causes the further increase in the luminescence decay rate between 50 and 300K. The origin of band III probably lies about 400 cm^{-1} above peak O.

The final picture that emerges from the spectra of these dioxorhenium ions is not as complex as the individual spectra suggest. Four discrete band systems can be observed in absorption, three of which exhibit progressions in a high energy (750-800 cm^{-1}) mode. Band IV, which does not clearly show a high energy progression because of interference from the more intense band III, could only be detected in the spectra of the cyanide and pyridine complexes and arises from two

Figure 4.18. Fit of the variation in luminescence decay rate of $K_3ReO_2(CN)_4$ to equation (4.4) in the temperature range 5 to 50 K.

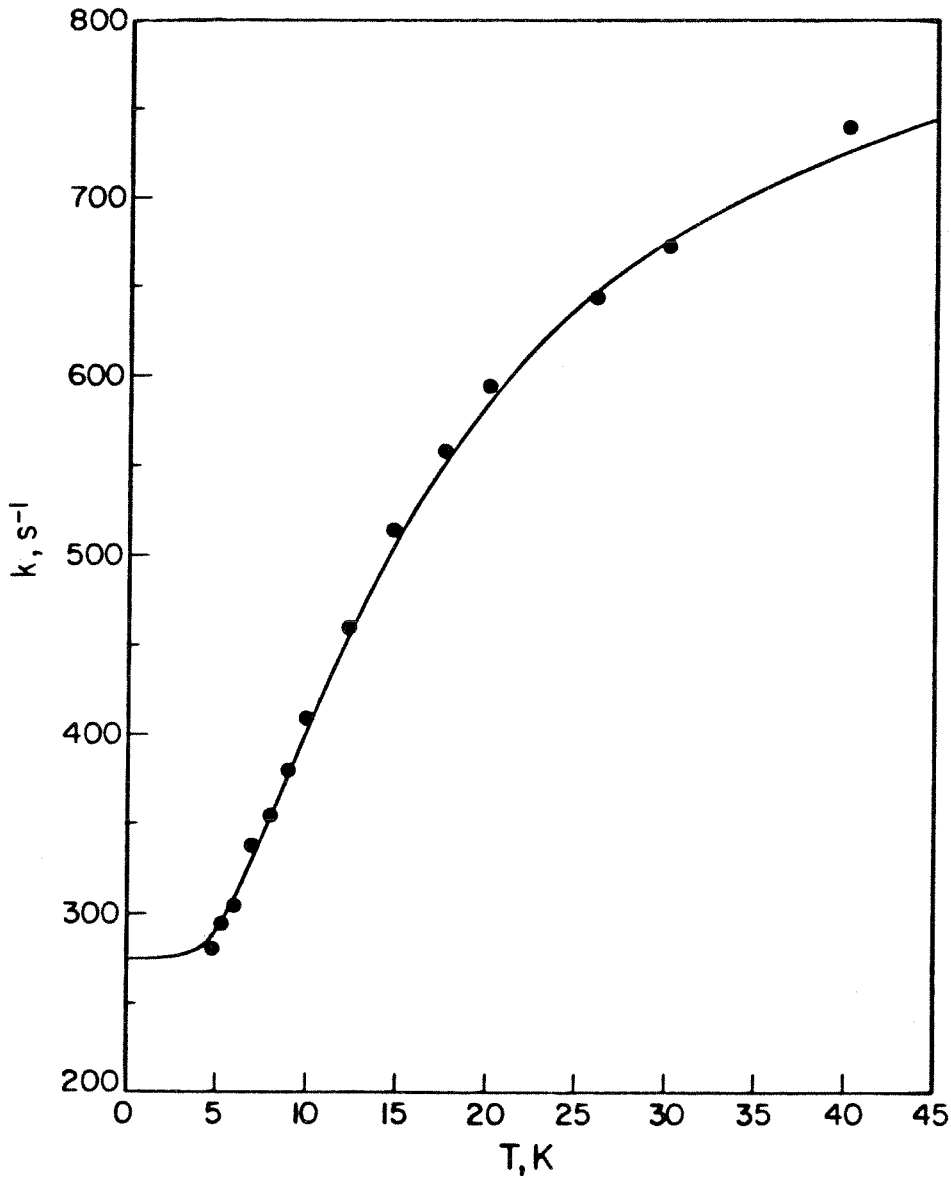
800
700
600
500
400
300
200
k, s⁻¹
0
5
10
15
20
25
30
35
40
45
T, K

very closely spaced ($< 20\ cm^{-1}$) electronic states. The origin of band III probably lies 400 to 500 cm^{-1} above the two origins in band system IV but, as with bands I and II, it is not possible to determine how many electronic states comprise this absorption feature. Finally, both components of band IV luminesce in the pyridine and cyanide complexes but no emission was observed from the ethylenediamine species.

2. Solution Luminescence and Photochemistry

The luminescence properties of dioxorhenium ions in solution are intimately related to their photochemical reactivity since photochemistry is simply a non-radiative decay pathway for an electronically excited molecule. The decay of dioxorhenium excited states is, in fact, quite sensitive to the nature of the solvent. $K_3ReO_2(CN)_4$, for example, is soluble only in water and, as with $[ReO_2(py)_4]^+$, does not luminesce in this solvent. The tetraphenylborate salt of $[ReO_2(py)_4]^+$, however, is soluble in aprotic solvents such as CH_2Cl_2, THF, and pyridine, and luminescence from the cation is easily detected in these media. The emission lifetime and quantum yield data for this ion as well as its isotopically and chemically substituted derivatives are summarized in Table 4.8. The quantum yields, measured with 436 nm excitation, are all in the range of 0.02 to 0.04 and the excited state lifetimes vary from 10 to 20 μs. The small variation in the excited state lifetime of $[ReO_2(py)_4]BPh_4$ among the aprotic solvents pyridine, CH_2Cl_2, and THF is probably a reflection of trace amounts of water in the solvents. The reduction of the $[ReO_2(py\text{-}d_5)]BPh_4$ excited state lifetime relative to its solid state value (140 μs, Table 4.4), however,

Table 4.8. Luminescence lifetimes and quantum yields of dioxorhenium complexes in solution.

Complex	Solvent	τ, μs[a]	ϕ_{em}[b]
$[ReO_2(py)_4]BPh_4$	pyridine	17(2)	0.03(1)
	THF	13(2)	0.03(1)
	CH_2Cl_2	4(1)	
$[ReO_2(py\text{-}d_5)_4]BPh_4$	THF	9(2)	0.04(1)
$[Re^{18}O_2(py)_4]BPh_4$	pyridine	15(2)	0.03(1)
$[ReO_2(4\text{-picoline})_4]BPh_4$	THF	17(2)	0.02(1)
$[ReO_2(4\text{-}\underline{t}\text{-butylpyridine})_4]BPh_4$	THF	21(2)	0.03(1)

a. Measured with 532 nm excitation.

b. Measured with 436 nm excitation.

is quite significant and suggests that some new lifetime limiting process is active in solution.

The effect of protic solvents on the luminescence properties of dioxorhenium ions was investigated by quenching $[ReO_2(py)_4]^+$ emission in pyridine with the proton donors water, methanol, ethanol, and their deuterated analogs. The change in luminescence lifetime of $[ReO_2(py)_4]^+$ as a function of quencher concentration [Q], very closely agrees with the Stern-Volmer equation (4.3) as shown in Figure 4.19. The quenching mechanism depends critically upon the hydroxyl protons of these molecules as demonstrated by the large deuterium isotope effect. It is tempting to suggest that simple proton transfer is the deactivation pathway for the luminescent dioxorhenium excited states, but three pieces of evidence suggest otherwise. First, a 4 ml pyridine solution containing $[ReO_2(py)_4]BPh_4$ (0.5 mM) and 40 μl of CH_3OH ($\sim$ 0.25 M) and 170 μl CH_3OD ($\sim$ 1.0 M) produces a non-exponentially decaying dioxorhenium excited state. The decays, however, are quite nicely fit by single exponentials when either CH_3OH or CH_3OD is used alone as a quencher. Second, addition of these proton donors, especially water, significantly changes the shapes of emission and absorption bands (Figure 4.20). Equal amounts of H_2O and D_2O produce roughly comparable changes in bandshape. Finally, the relatively strong proton donor, pyH^+ (pK_a = 5.25[58]), is not an efficient quencher of $[ReO_2(py)_4]^+$ luminescence even though its pK_a is almost 10 units smaller than that of the other proton donors. Cleary, a rather complex mechanism involving both ground and excited states leads to the rapid deactivation of the dioxorhenium excited state in the presence of

Figure 4.19. Stern-Volmer plots of the quenching of excited $[ReO_2(py)_4]^+$ in pyridine solution by the proton donors: (●) H_2O; (▲) CH_3OH; (■) C_2H_5OH; (○) D_2O; (Δ) CH_3OD; (+) CD_3OD; and (□) C_2H_5OD.

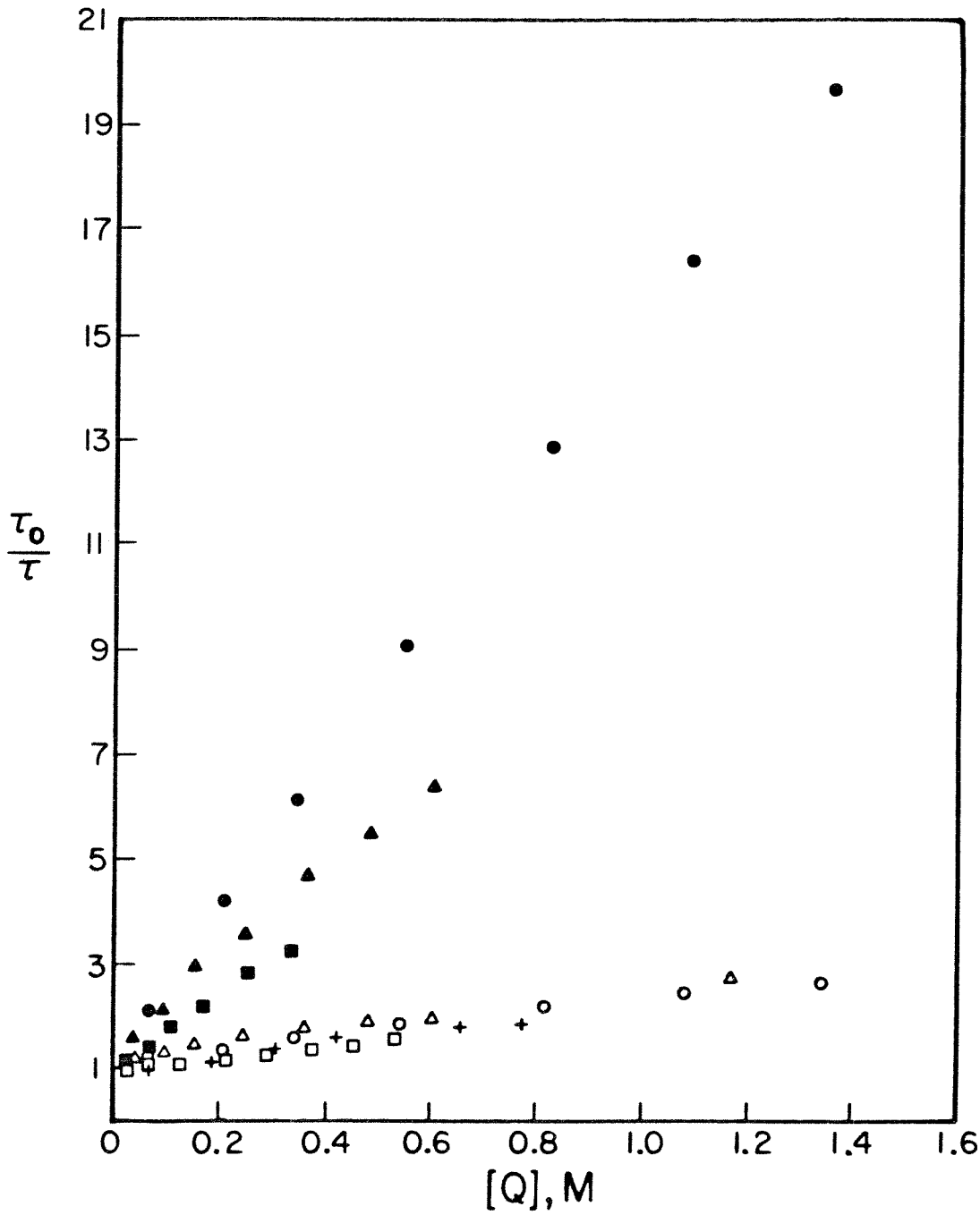
21
19
17
15
13
11
9
7
5
3
1
$\frac{\tau_0}{\tau}$
0
0.2
0.4
0.6
0.8
1.0
1.2
1.4
1.6
[Q], M

Figure 4.20. Perturbations of $[ReO_2(py)_4]^+$ absorption and emission spectra by proton donors. (a), (c) Absorption and emission spectra, respectively, of $[ReO_2(py)_4]BPh_4$ in pyridine (2.2 mg/4 ml) under vacuum. (b), (d) Same spectra recorded after addition of 250 μl H_2O to the solution.

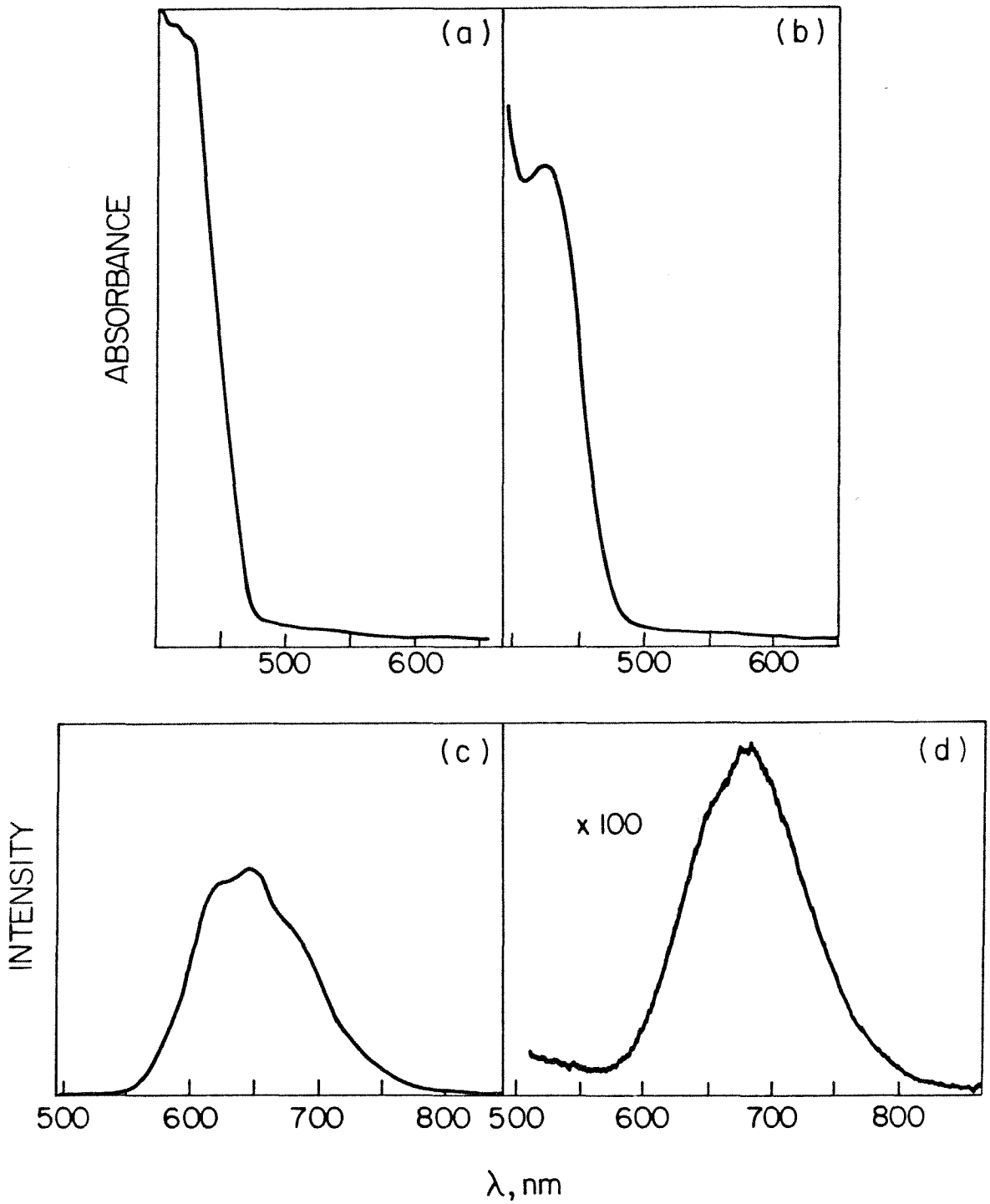
(a)
(b)
ABSORBANCE
500
600
500
600
(c)
(d)
x 100
INTENSITY
500
600
700
800
500
600
700
800
λ, nm

proton donors.

The spectroscopic studies of the previous section suggested (vide infra) that the dioxorhenium complexes might perform as photochemical oxygen atom transfer reagents. In addition, the apparent affinity of the excited ReO_2^+ unit for protons implied that the oxygen atom acceptors should also be susceptible to nucleophilic attack. In this regard, three α,β-unsaturated carbonyls and three trivalent phosphorus compounds were investigated for their ability to quench the luminescence of $[ReO_2(py)_4]BPh_4$ in pyridine. The results are summarized in Table 4.9. Of the six quenchers investigated, only triphenylphosphite, which quenched with a rate constant of $2 \times 10^5 M^{-1} s^{-1}$, led to any net photochemistry upon steady-state irradiation. The products of this photochemical reaction were dark brown, paramagnetic (EPR signal), and air sensitive but, unfortunately, no single species was isolated from the reaction mixture nor was triphenylphosphate detected.

D. Discussion

1. Spectroscopy and Electronic Structure

The electronic spectra and structures of the dioxorhenium ions are probably best explained by a simple adaptation to D_{4h} symmetry of the Gray-Hare molecular orbital model for the molybdenyl ions.[23] This adaptation is illustrated in Figure 4.21. The dioxorhenium ions possess $\underline{d}^2$ metal centers and will produce a diamagnetic $^1A_{1g}[(b_{2g})^2]$ ground state. The lowest energy ligand field transition will involve the promotion of an electron from the $b_{2g}(\underline{xy})$ orbital to the doubly degenerate $e_g(\underline{xz}, \underline{yz})$ level producing $^3E_g[(b_{2g})^1(e_g)^1]$ and $^1E_g[(b_{2g})^1(e_g)^1]$

Table 4.9. Luminescence quenching of $[ReO_2(py)_4]^+$ in pyridine by potential oxygen atom acceptors.

Quencher	Concentration, M	τ_0/τ
PPh_3	0.14	1.0[a]
$P(OCH(CH_3)_2)_3$	0.8	1.2
$P(OPh)_3$	0.8	7.2 ($k_q = 2 \times 10^5\ M^{-1}\ s^{-1}$)
$(CH_3)_2CCHCO(OCH_3)$	1.7	2.4
$H_2CC(CH_3)CO(OC_2H_5)$	1.6	1.6
$(C_2H_5O)OCCHCHCO(OC_2H_5)$	1.2	1.0

a. Luminescence intensity measurement.

Figure 4.21. d orbital splitting diagram for trans-dioxorhenium(V) complexes.

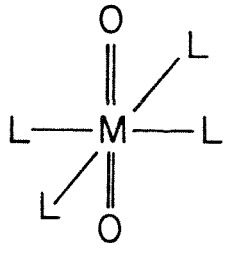

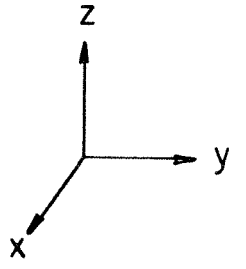

——— a_{1g} (z^2)

——— b_{1g} (x^2-y^2)

Ground State:
$^1A_{1g}[(b_{2g})^2]$

═══ e_g (xz, yz)

Excited States:
$^{3,1}E_g$ $[(b_{2g})^1(e_g)^1]$

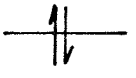 b_{2g} (xy)

excited states. This one-electron transition is entirely analogous to the $^2E \leftarrow {}^2B_2$ transition in the molybdenyl ions but should give rise to two absorption bands corresponding to the singlet and triplet excited states. Both transitions are Laporte forbidden ($g \not\longleftrightarrow g$) and must acquire intensity by vibronic and, in the case of the triplet state, spin-orbit coupling mechanisms. The singlet state is likely to be more intense than the triplet and assignments of bands II and III to the $^1E_g[(b_{2g})^1(e_g)^1] \leftarrow {}^1A_{1g}[(b_{2g})^2]$ and $^3E_g[(b_{2g})^1(e_g)^1] \leftarrow {}^1A_{1g}[(b_{2g})^2]$ transitions, respectively, are most appealing. These simple assignments, however, do not account for the two states in band system IV but their presence can be explained by ligand field theoretical arguments.

A ^3E_g state in D_{4h} symmetry is sixfold degenerate and in the presence of a strong spin-orbit coupling perturbation will decompose into states of A_{1g}, A_{2g}, B_{1g}, B_{2g}, and E_g symmetries in the D_{4h}' double group while the doubly degenerate ^1E_g state just correlates with an E_g level. A simple first order spin-orbit coupling calculation (Appendix 2) produces the diagram in Figure 4.22. At this level of approximation, the (B_{1g}, B_{2g}) and (A_{1g}, A_{2g}) pairs are not split by spin-orbit coupling and only the $E_g(^3E_g)$ level can acquire singlet character by mixing with the $E_g(^1E_g)$ state. The abscissa in Figure 4.22 corresponds to the dimensionless parameter λ/ϵ_{12}, the effective molecular spin orbit coupling constant divided by the magnitude of the singlet-triplet energy gap in the absence of a spin-orbit coupling perturbation, and the ordinate is just the energy of the state Γ divided by ϵ_{12}. Since only the $E_g(^3E_g)$ level can steal singlet character from

Figure 4.22. Perturbations of ^1E_g and ^3E_g states as a result of spin orbit coupling. ϵ_{12} is the singlet-triplet energy gap in the absence of a spin-orbit coupling perturbation; $\epsilon(\Gamma)$ is the energy of state Γ; and λ is effective molecular spin-orbit coupling constant.

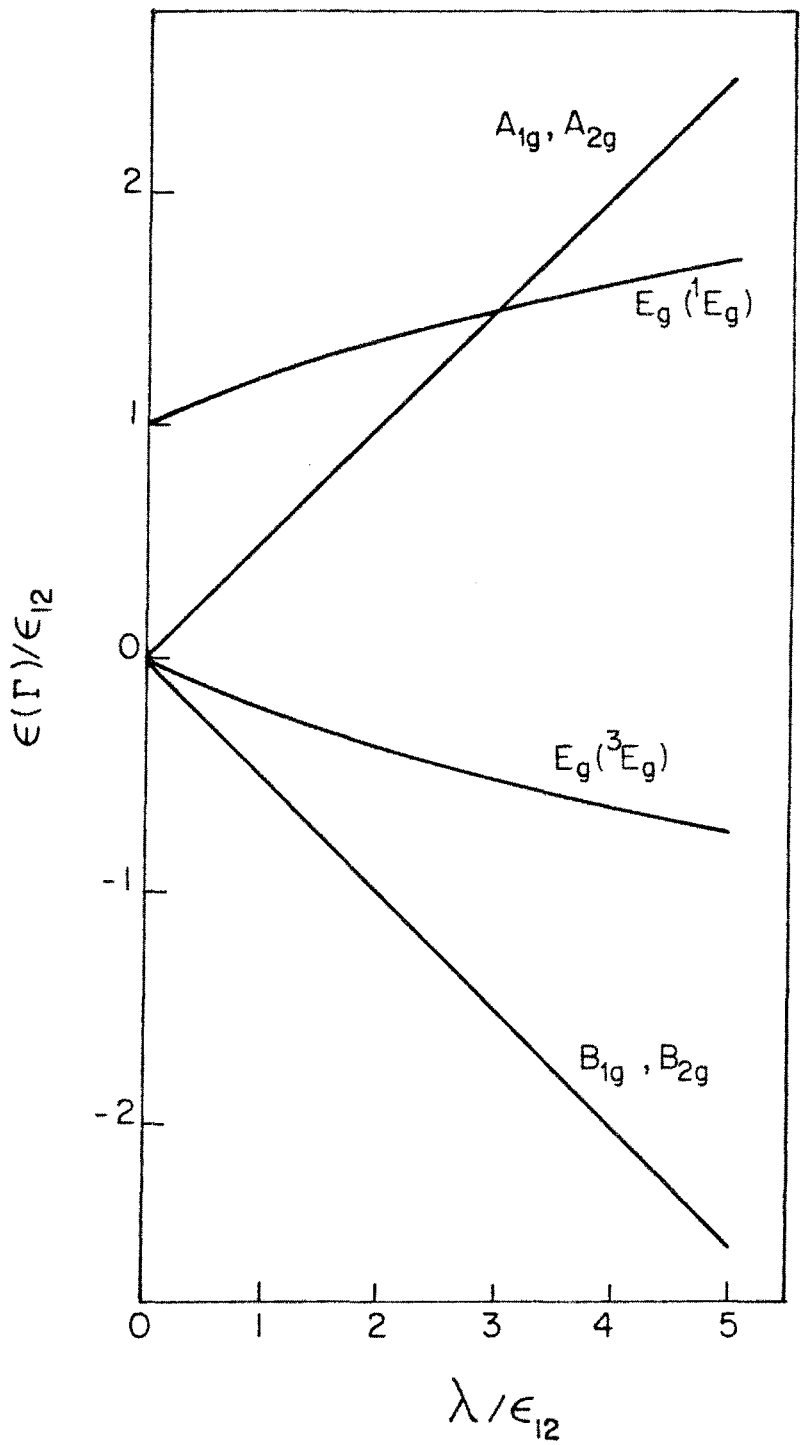
A_{1g}, A_{2g}
E_g (^1E_g)
E_g(^3E_g)
B_{1g} , B_{2g}
2
1
0
-1
-2
0
1
2
3
4
5
$\epsilon(\Gamma)/\epsilon_{12}$
λ/ϵ_{12}

the $E_g(^1E_g)$ state, it should be the most intense of the transitions to states derived from ^3E_g.

The data are in rather good agreement with the model depicted in Figure 4.22. The two states that comprise band system IV are most likely the $B_{1g}(^3E_g)$ and $B_{2g}(^3E_g)$ levels. The fact that these transitions are Laporte forbidden ($g \leftarrow g$) explains the presence of vibronic origins built on vanishingly small pure electronic origins in the spectra of these states. In both the cyanide and pyridine complexes these two states are separated by fewer than 20 cm^{-1} which strongly supports the electronic structure model in Figure 4.22. It is not possible, on the basis of the available data, to determine the relative positions of the B_{1g} and B_{2g} states. Band system III is probably comprised of the $E_g(^3E_g) \leftarrow A_{1g}(^1A_{1g})$ transition which would account for its greater intensity and slightly higher energy than band IV. Band III probably also obscures the $A_{1g}(^3E_g)$ and $A_{2g}(^3E_g)$ states and band II then corresponds to the $E_g(^1E_g) \leftarrow A_{1g}(^1A_{1g})$ excitation. That bands II and III in the pyridine complex are much more intense than the analogous features in the spectra of the cyanide and ethylenediamine complexes is probably the result of the proximity of metal to ligand charge transfer states in the pyridine species from which the $E_g(^1E_g)$ and $E_g(^3E_g)$ states could steal intensity. The two complexes $[ReO_2(CN)_4]^{3-}$ and $[ReO_2(py)_4]^+$ fit on the diagram in figure 4.22 at λ/ϵ_{12} values of 0.2 and 0.3, respectively. The calculated values of ϵ_{12} and λ are 3900 cm^{-1} and 900 cm^{-1}, respectively, for $K_3ReO_2(CN)_4$ and 3900 cm^{-1} and 1200 cm^{-1} for $[ReO_2(py)_4]BPh_4$ (Appendix 2). Finally, band I observed in the cyanide and ethylenediamine complex

spectra must arise from a different one-electron transition, perhaps either $a_{1g}(\underline{z}^2) \leftarrow b_{2g}(\underline{xy})$ or oxygen LMCT.

The low temperature spectra of these dioxorhenium complexes are rife with vibrational fine structure. All of the bands observed, both in absorption and emission, progress in a high energy mode that corresponds to the symmetric rhenium-oxygen stretching vibration.[59] Confirmation of this assignment is provided by the spectra of $[Re^{18}O_2(py)_4]BPh_4$ in which the frequency of the progressing mode decreases by a factor of 0.95(1). That the mode is symmetric is implied by its absence from the infrared spectra of these molecules. These progressions in the rhenium-oxygen stretching vibration indicate a displacement of the potential surfaces of states with the $[e_g(\underline{xz},\underline{yz})^1 b_{2g}(\underline{xy})^1]$ configuration relative to that of the $[b_{2g}(\underline{xy})^2]$ state. This displacement along the symmetric Re-O coordinate is probably an elongation in the excited state since the force constant for this vibration is only three fourths of its ground state value. Furthermore, a transition that removes an electron from the $b_{2g}(\underline{xy})$ orbital and places it in the Re-O π-antibonding $e_g(\underline{xz},\underline{yz})$ level should result in lengthened metal-oxygen bonds. The magnitude of this distortion can be estimated from the Franck-Condon fits to the 5 K emission spectra of $K_3ReO_2(CN)_4$ and $[ReO_2(py)_4]BPh_4$ (Figures 4.23 and 4.24, respectively). Estimated distortions of 0.09(1) Å (from 1.781(3) Å[47]) for $K_3ReO_2(CN)_4$ and 0.07(1) Å for $[ReO_2(py)_4]BPh_4$ were used to generate the calculated spectra in these figures (Appendix 1). These distortions are somewhat smaller than that found in the molybdenyl ion but still represent significant elongations of the rhenium-oxygen bonds. The

Figure 4.23. Franck-Condon fit to the 5 K emission spectrum of $K_3ReO_2(CN)_4$. Upper spectrum: calculated. Lower spectrum: experimental.

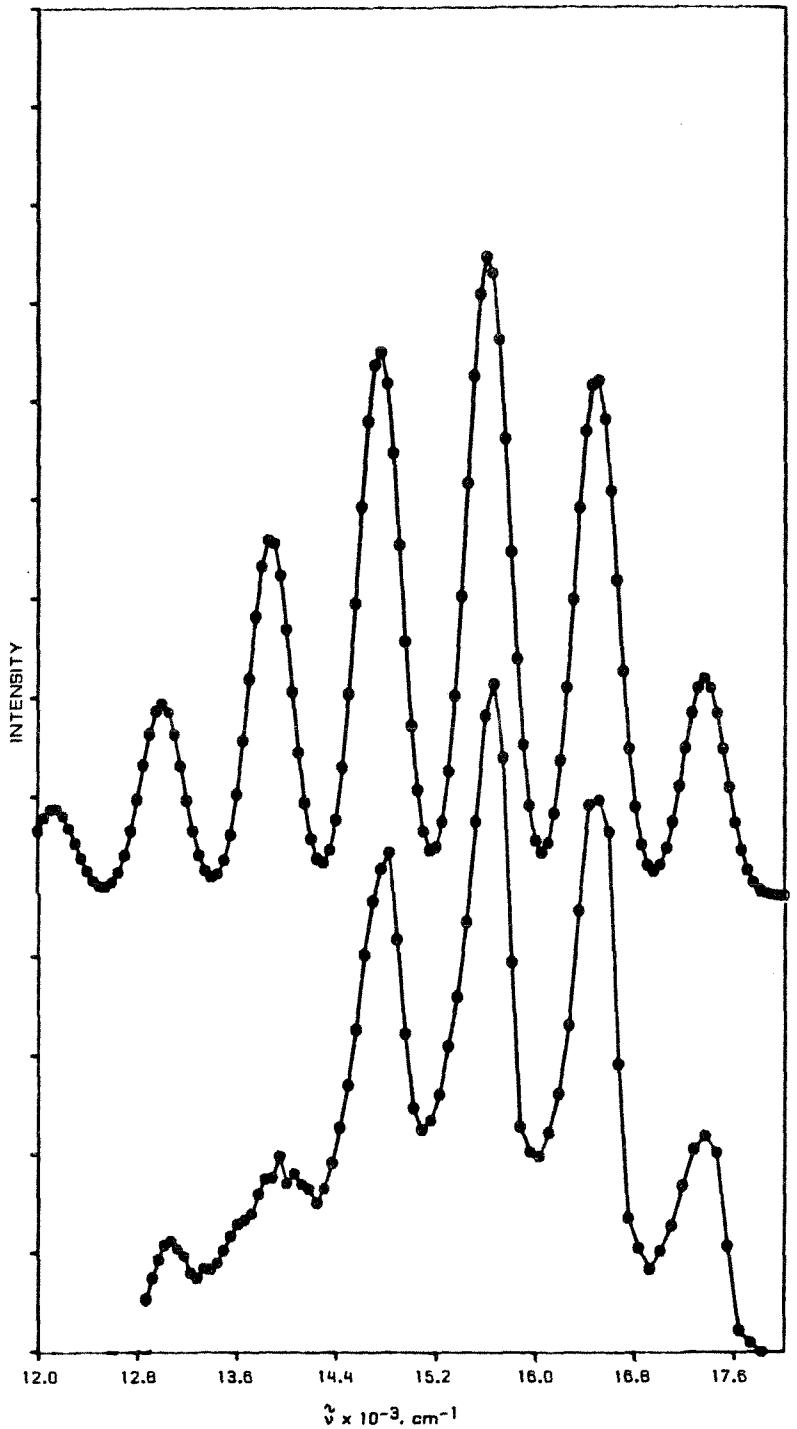
INTENSITY
12.0
12.8
13.6
14.4
15.2
16.0
16.8
17.6
$\tilde{\nu} \times 10^{-3}$, cm^{-1}

Figure 4.24. Franck-Condon fit to the 5 K emission spectrum of $[ReO_2(py)_4]BPh_4$. Upper spectrum: calculated. Lower spectrum: experimental.

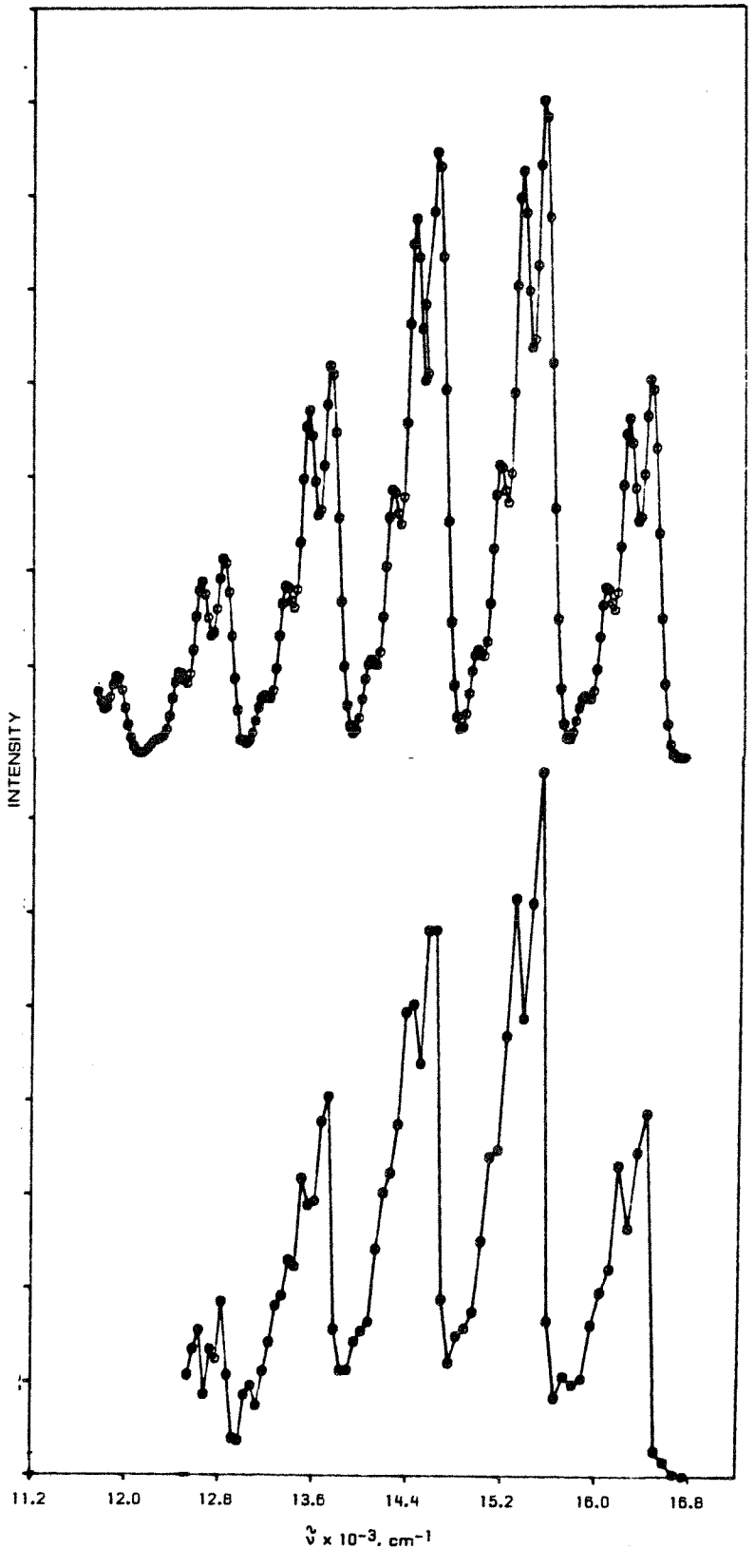
INTENSITY
11.2
12.0
12.8
13.6
14.4
15.2
16.0
16.8
$\bar{\nu}$ x 10^{-3}, cm^{-1}

emission spectrum of $[ReO_2(py)_4]BPh_4$ displays a second progression in a mode of ca. 190 cm^{-1}. Hints of an analogous progression in ca. 170 cm^{-1} are found in band III in the absorption spectrum of this molecule. This vibration probably corresponds to the symmetric rhenium-pyridine stretch[60] and a distortion along this coordinate arises because an electron in a rhenium-pyridine π-bonding orbital, $b_{2g}(xy)$, is involved in the transition. The magnitude of this distortion is calculated to be about 0.03 (1) Å (Appendix 1). The ca. 225 cm^{-1} progression in band II of the $[ReO_2(en)_2]Cl$ absorption spectrum is likely to arise from a small distortion involving the equatorial ethylenediamine ligands.[61] The remaining sharp vibronic maxima in the dioxorhenium absorption and emission spectra are either vibronic origins or components of rhenium-oxygen progressions built on these vibronic origins.

The luminescence decay properties of the $[ReO_2(CN)_4]^{3-}$ ion prove to be of considerable value in the determination of the electronic structure of this complex. The change in luminescence lifetime as a function of temperature in the 5 to 20 K region clearly demonstrates the presence of two emitting states. The luminescence lifetimes of both $K_3ReO_2(CN)_4$ and $[ReO_2(py)_4]BPh_4$ decrease by about a factor of 2 upon warming from 70 to 300 K. This temperature dependence could be the result of the thermal population of another excited state, presumably $E_g(^3E_g)$, or the intrinsic temperature dependence of the decay rates of the $B_{1g}(^3E_g)$ and $B_{2g}(^3E_g)$ states, or both. It is difficult, therefore, to derive any meaningful conclusions about the mechanisms of non-radiative decay in these molecules solely on the basis of the temperature dependence of the emission lifetime. One important

observation that pertains to the non-radiative decay in these molecules is the fact that the excited state lifetime of crystalline $[ReO_2(py)_4]BPh_4$ increases by about a factor of four upon deuteration of the pyridine rings. Similar behavior is observed upon deuteration of the ammine ligands in a numberof Rh ammine species.[62,63] Oxygen-18 substitution, however, does not significantly effect the luminescence lifetime of the $[ReO_2(py)_4]^+$ cation. This behavior, in which the excited state decay rate is sensitive to the highest energy vibrational modes in the molecule, exemplifies the weak coupling limit of non-radiative decay theory.[42] In the weak coupling limit $G \ll 1$ (eqn 2.24) and the relative displacements of potential energy surfaces are small. This situation is mathematically more complex than the Gaussian regime[41] but Englman and Jortner[42] have derived an expression for the non-radiative decay rate in the low temperature weak coupling limit. Their expression for k_{nr} exhibits an exponential dependence on the ratio of the energy gap, ΔE, to the energy of the highest frequency vibrational modes in the molecule, $\hbar\omega_M$. These high energy vibrations are "accepting modes" for the excess energy produced by the non-radiative transition. It is clear, then, how perdeuteration of the pyridine rings in $[ReO_2(py)_4]BPh_4$ could increase the lifetime of the dioxorhenium excited state. It is important to note that $\hbar\omega_M$ is the energy of the highest frequency vibrational mode in the molecule along which there is a distortion between states Ψ_s and Ψ_n.[64] Thus, though it is not apparent from the absorption or emission spectra, the $e_g(\underline{xz}, \underline{yz}) \leftarrow b_{2g}(\underline{xy})$ transition is accompanied by a small distortion along the C-H stretching coordinate of the pyridine rings in

$[ReO_2(py)_4]BPh_4$.

The fact that $[ReO_2(en)_2]Cl$ does not luminesce is quite perplexing. The absorption spectrum of this molecule is quite similar to those of the pyridine and cyanide analogs so it is not likely that major electronic structure differences account for the radically different non-radiative decay properties of the ethylenediamine complex. Subtle changes in the electronic and vibrational structures of $[ReO_2(en)_2]Cl$ must, therefore, be the sources of its unusual photophysical behavior.

The dioxorhenium ions have fulfilled the expectations outlined at the end of Chapter Three. The difference in spin multiplicity between the lowest excited states and the ground state seems to have produced much slower radiative and non-radiative decay rates than found in the molybdenyl ions. The property of an activated metal-oxygen bond in the lowest electronic excited state is, however, retained in the dioxorhenium species. These long lifetimes and activated bonds could lead to some novel dioxorhenium photochemistry.

2. Solution Luminescence and Photochemistry

In order to participate directly in bimolecular chemical reactions, the excited dioxorhenium species must live for greater than 50 ns in solution. A very common constituent of many solvents, the proton, however, very effectively quenches these excited metal complexes. The mechanism of quenching by protons is not clear and, though Stern-Volmer kinetics are obeyed with individual quenchers, it is not a simple bimolecular photochemical reaction. Were it so, the binary mixture of CH_3OH and CH_3OD would have given an apparent quenching

rate constant equal to the sum of the two pseudo-first order rate constants for the two quenchers. To the contrary, the CH_3OH/CH_3OD mixture produced non-exponential luminescence decay, indicative of two discrete luminescing species that are not in chemical equilibrium with one another.[54] This result, coupled with the fact that the presence of these protic quenchers perturbs both the absorption and emission spectra of $[ReO_2(py)_4]^+$, argues for some type of complex formation (perhaps via hydrogen bonding) between the dioxorhenium ion and the proton donors. The isotope effect observed with the hydroxyl hydrogens of these quenchers could then simply be a manifestation of the weak coupling limit of non-radiative decay theory. That is, the dioxorhenium/protic solvent system possesses O-H stretching vibrations that could act as accepting modes for the non-radiative transition.[65] No saturation of the quenching appears at high proton donor concentrations as would be expected from a simple complex formation mechanism. Thus, unless the formation constant for this complex is exceptionally small, still more mechanisms must be contributing to the proton enhanced decay of dioxorhenium excited states.

As shown in Table 4.8, however, dioxorhenium ions do luminesce rather efficiently in aprotic solvents. The lifetimes and quantum yields do not depend greatly upon the nature of the aprotic solvent. The change in lifetime between solid state and solution of the $[ReO_2(py\text{-}d_5)]^+$ complex is significant, as is that of the ^1H analog. This reduction of lifetime in solution could be due to the introduction of new non-radiative decay pathways arising from solvent complex

formation or equatorial ligand dissociation.[46]

Clearly, any bimolecular photochemistry involving the dioxorhenium complexes must be performed in aprotic media. The Franck-Condon analyses described in the previous section indicate a ca. 0.1 Å elongation of the rhenium-oxygen bond in the lowest electronic excited state. This metal-oxygen bond activation could be construed as motion along a photochemical oxygen atom transfer reaction coordinate. The proton quenching behavior of $[ReO_2(py)_4]^+$ also indicates that the excited species might be somewhat nucleophilic. α,β-Unsaturated carbonyls are well known for their susceptibility to nucleophilic attack[66] and to oxidation at the carbon-carbon double bond.[67] Two molecules of this type, mesityl oxide and ethyl methacrylate, in fact, quench the luminescence of $[ReO_2(py)_4]^+$ in pyridine but neither led to any clean photochemical transformation upon steady-state irradiation. Trivalent phosphorus compounds are well known oxygen atom acceptors and their susceptibility to oxygen atom donors such as pyridine-N-oxide increases in the series $PPh_3 \ll P(OC_2H_5)_3 < P(OPh)_3$.[68] Pyridine-N-oxide behaves as a nucleophile in many reactions[69] and could resemble the excited dioxorhenium unit. Of the three trivalent phosphorus compounds investigated, only triphenylphosphite quenched $[ReO_2(py)_4]^+$ luminescence ($k_q = 2 \times 10^5\ M^{-1}\ s^{-1}$). In addition, steady-state irradiation of a $[ReO_2(py)_4]BPh_4/P(OPh)_3$/pyridine mixture led to a net photochemical reaction. No simple oxygen atom transfer products could be isolated from the photolysis mixture and the fault could lie in the inherent unsuitability of dioxorhenium ions to act as oxygen atom transfer reagents. Upon transfer of one oxygen from $[ReO_2(py)_4]^+$ to

an acceptor in an aprotic solvent, a mono-oxorhenium(III) fragment is produced in which two electrons occupy an e(xz,yz) rhenium-oxygen π-antibonding level. This species is likely to be very unstable and, if it can be produced at all, will react rapidly with other molecules in solution. Hence, photochemical oxygen atom transfer with dioxo-rhenium ions should be particularly difficult to induce and will probably not yield clean atom transfer products. The photochemical reaction between $[ReO_2(py)_4]^+$ and $P(OPh)_3$ does, however, resemble some thermal chemistry between a dioxo-osmium(VI) complex and PPh_3 observed by Collins.[70] Though the reaction is rather complicated, net oxidation of PPh_3 by the dioxo-osmium(VI) species is implied. That any d^2 trans-dioxometal complex can transfer oxygen atoms to substrates, regardless of mechanism, offers a faint glimmer of hope that analogous photochemistry might yet be performed.

CHAPTER FIVE

Conclusion

Perhaps the most important result to emerge from the investigations described in Chapters Three and Four is the discovery of a new luminescent chromophore common to transition metal-oxo complexes. The luminescent excited state arises from the promotion of an electron in a primarily metal localized orbital to a metal-oxygen π-antibonding level. This $\pi^*_{M-O} \leftarrow d$ excitation is quite different from the ligand to metal charge transfer transitions in other luminescent metal-oxo complexes such as CrO_2Cl_2,[71] MO_4^{n-} (M = V, n = 3; M = W, n = 2),[72] and UO_2^{2+} species.[73] Both $\underline{d}^1$ and $\underline{d}^2$ metals luminesce from $(\underline{xz}, \underline{yz}) \leftarrow (\underline{xy})$ excited states and in the $\underline{d}^2$ case at least two spin-orbit components of the lowest ^3E_g state emit. The lowest energy excited states of the $\underline{d}^2$ metal centers are typically much longer lived than their $\underline{d}^1$ counterparts probably because of the spin restriction imposed on the radiative and non-radiative transition matrix elements in the $\underline{d}^2$ complexes.

The $(\underline{xz}, \underline{yz}) \leftarrow (\underline{xy})$ transition is also accompanied by a ca. 0.1 Å elongation of the metal oxygen bonds in both the molybdenyl and dioxorhenium systems. This metal-oxygen bond activation could be interpreted as motion along a photochemical oxygen atom transfer reaction coordinate. In spite of this activation, however, electronically excited dioxorhenium ions could not be induced to transfer oxygen atoms. The reasons for this inactivity are probably both kinetic and thermodynamic. The kinetic barrier is imposed by the paradoxical nature of a nucleophilic oxygen atom donor. The oxygen atom acceptor is formally oxidized by two electrons in such a reaction and, therefore, is likely to possess a surfeit rather than a deficit of electron density. A better

excited state for oxygen atom transfer reactions would arise from an oxygen to metal charge transfer transition. The thermodynamic barrier is the result of the oxygen atom that remains behind following oxygen atom transfer from an excited dioxorhenium molecule. Clearly, if photochemical atom transfer reactions do not lead to stable products, the extra ca. 2 eV of driving force in an electronically excited molecule may still be insufficient to facilitate the chemical transformation. In this regard, a better candidate for photochemical oxygen atom transfer reactivity would be a d^2 metal mono-oxo species that, upon reaction, would produce a stable d^4 metal complex. A number of molybdenum(IV) oxo complexes that meet these criteria have been prepared.[21c] Alternatively, initial investigations of a rhenium(V) mono-oxo phosphine complex hint at some success. Irradiation of $[ReOCl_3(PPh_3)_2]$ yields an oxygen sensitive, paramagnetic species that no longer displays a Re-O stretching peak in its infrared spectrum. These experiments suggest that an intramolecular photochemical oxygen atom transfer reaction might be occurring.[74]

A final conclusion that can be drawn from Chapters Three and Four derives from the utility of electronic spectroscopy in the study of photochemical reactivity. Spectroscopic experiments provide more information than a simple ordering and assignment of electronic states. Investigations of transitions between electronic states betray the relative shapes and positions of their potential surfaces. Electronic spectra, therefore, can be rich in that structural information about electronically excited molecules that is essential to their complete characterization. Indeed, in order that excited molecules be treated

and understood as discrete chemical reagents, they must be fully electronically and structurally characterized. Electronic spectroscopy remains the primary tool in this process.

APPENDICES

1. Franck-Condon Analyses

The relative intensities of two components in a vibrational progression is governed by the ratio of the Franck-Condon factors for the particular vibronic transition. Ansbacher has derived a convenient recursion relation within the displaced harmonic oscillator approximation where the Franck-Condon factor for the $\Psi_k^{v''_\mu=n+1} \leftarrow \Psi_j^{v'_\mu=0}$ transition $(R_{0,n+1})^2$, is given by[12]

$$R_{0,n+1} = \frac{-1}{(1+\delta^2)[2(n+1)]} \{2\delta\gamma R_{0,n} + (\delta^2-1)\sqrt{2n}\, R_{0,n-1}\} \quad \text{(A1.1)}$$

where $\delta^2 = \frac{\omega'_\mu}{\omega''_\mu}$, the ratio of the vibrational frequencies of mode μ in the two states, and $\gamma = (\omega'_\mu/\hbar)^{\frac{1}{2}} \Delta s^0_\mu$ where Δs^0_μ is the change in the equilibrium value of the mass weighted normal coordinate s_μ. Expression (A1.1) is especially well suited to comparisons of relative intensities of vibronic bands in a structured electronic spectrum.

In order to estimate the overall intensity of a component in a vibrational progression, the spectra were deconvoluted into a sum of Gaussian envelopes. The ratios $(R_{0,n}/R_{0,0})$ were then determined through equation (2.16). The values of ω'_μ and ω''_μ were either taken directly from the electronic spectra or from the vibrational spectrum of the molecule. Optimum values of γ were determined by iteratively minimizing the sum of the squares of the deviations between the calculated and experimental ratios, $(R_{0,n}/R_{0,0})$. Typically, only the first few members of a progression were used in the iteration procedure since overlapping spectral bands, poorer resolution, and low

spectrometer sensitivity greatly increased the error in estimating the intensities of the higher progression members. The magnitude of the distortion along an internal coordinate of the molecule was determined from the value of γ and the assumed internal coordinate composition of the normal mode. Calculated spectra were generated by minimizing the sum of the squares of the deviations between experimental and calculated vibronic peak intensities then plotting as a sum of Gaussian envelopes. The final values of all parameters involved in the four Franck-Condon analyses described in earlier chapters are listed in Table A1.1.

Table A1.1. Parameters used in Franck-Condon analyses.

	$^2E \rightarrow {}^2B_2$	$^2B_1 \leftarrow {}^2B_2$	$^3E_g \rightarrow {}^1A_{1g}$	$^3E_g \rightarrow {}^1A_{1g}$ [a]
	$(Ph_4As)MoOCl_4$	$(Ph_4As)MoOCl_4$	$K_3ReO_2CN_4$	$[ReO_2(py)_4]BPh_4$
ω'_μ, cm^{-1}	900	35	770	780, 170
ω''_μ, cm^{-1}	1,008	350	870	900, 190
γ	1.73	2.53	2.37	2.04, 1.36
Δq, Å	0.09(1)[b]	0.07(1)[c]	0.09(1)[d]	0.07(1)[d], 0.03(1)[e]
N[f]	3	4	4	4, 3

a. The first number corresponds to the Re-O progression and the second to the Re-py progression.

b. Assumed a pure Mo-O stretching mode.

c. Assumed a pure, totally symmetric Mo-Cl stretching mode.

d. Assumed a pure, totally symmetric Re-O stretching mode.

e. Assumed a pure, totally symmetric Re-py stretching mode.

f. Number of vibronic maxima used in the fit.

2. Spin-Orbit Coupling Calculations

A. Molybdenyl Ions

The four functions that were assumed to comprise the $^2E(\underline{xz}, \underline{yz})$ state in the MoO^{3+} ion are

$$\phi_1 = |x\overset{+}{z}\rangle \qquad \phi_2 = |x\overset{-}{z}\rangle$$

$$\phi_3 = |y\overset{+}{z}\rangle \qquad \phi_4 = |y\overset{-}{z}\rangle$$

where $|xz\rangle$ and $|yz\rangle$ are real $\underline{d}$ orbital wavefunctions. The following linear combinations diagonalize the spin-orbit coupling energy matrix of the Hamiltonian, $\hat{H}_{SO} = \xi \hat{\ell} \cdot \hat{s}$;

$$\psi_1 = \frac{1}{\sqrt{2}} (\phi_2 - i\phi_4)$$

$$\psi_2 = \frac{1}{\sqrt{2}} (\phi_3 - i\phi_1)$$

$$\psi_3 = \frac{1}{\sqrt{2}} (\phi_4 - i\phi_2)$$

$$\psi_4 = \frac{1}{\sqrt{2}} (\phi_1 - i\phi_3) .$$

The expectation values of $\hat{H}_{SO}$ given by these functions are $\epsilon_1 = \epsilon_2 = \frac{1}{2}\xi$ and $\epsilon_3 = \epsilon_4 = -\frac{1}{2}\xi$.[75] The functions ψ_1 and ψ_2 transform as the Γ_7 representation in C'_{4v} symmetry and ψ_3 and ψ_4 as Γ_6.[38]

B. Dioxorhenium Ions

The $(e_g)^1(b_{2g})^1$ electronic configuration in D_{4h} symmetry produces ^1E_g and ^3E_g states. These two states are separated by an energy gap, ϵ_{12}, resulting from differences in interelectron repulsions. The

transformation properties of these states in the D'_{4h} double group are given by the direct product $\Gamma_S \times \Gamma_i$ where Γ_S is the representation of the spin functions and Γ_i is the representation of the spatial function ψ_i. The ^3E_g and ^1E_g states, therefore, correlate with A_{1g}, A_{2g}, B_{1g}, B_{2g}, $E_g(^3E_g)$ and $E_g(^1E_g)$ states in D'_{4h}. Symmetry adapted functions for these states were determined with the aid of the tables in Appendix 2 of Griffith's book[38] and are most easily presented as linear combinations of their O'_h parent functions:

$$|A_1a_1\rangle = \sqrt{\frac{2}{3}}\,|A_1(^3T_1)\,a_1\rangle + \sqrt{\frac{1}{3}}\,|E(^3T_1)\,\theta\rangle$$

$$|A_2a_2\rangle = |T_1(^3T_1)\,z\rangle$$

$$|B_1b_1\rangle = |E(^3T_1)\,\epsilon\rangle$$

$$|B_2b_2\rangle = |T_2(^3T_1)\,\zeta\rangle$$

$$|E(^3E)\,\alpha\rangle = \frac{1}{\sqrt{2}}\,|T_1(^3T_1)\,x\rangle - \frac{1}{\sqrt{2}}\,|T_2(^3T_1)\,\xi\rangle$$

$$|E(^3E)\,\beta\rangle = -\frac{1}{\sqrt{2}}\,|T_1(^3T_1)\,y\rangle - \frac{1}{\sqrt{2}}\,|T_2(^3T_1)\,\eta\rangle$$

$$|E(^1E)\,\alpha\rangle = |T_2(^1T_2)\,\xi\rangle$$

$$|E(^1E)\,\beta\rangle = |T_2(^1T_2)\,\eta\rangle$$

where the subscript g's have been omitted. The matrix elements of the spin-orbit coupling operator, $\hat{H}_{SO} = \lambda \hat{L} \cdot \hat{S}$, were determined from Table A33 in Griffith's book.[38] The only off-diagonal elements within this eight function basis set, of course, occur between the doubly

degenerate E_g states. The spin-orbit coupling energy matrix is shown in Table A2.1 and was diagonalized to yield the following expectation values:

$$\epsilon_{A_{1g}} = \epsilon_{A_{2g}} = \tfrac{1}{2}\lambda$$

$$\epsilon_{B_{1g}} = \epsilon_{B_{2g}} = -\tfrac{1}{2}\lambda$$

$$\epsilon_{E_g(^3E_g)} = \tfrac{1}{2}\epsilon_{12} - \tfrac{1}{2}\left[(\epsilon_{12})^2 + \lambda^2\right]^{\frac{1}{2}}$$

$$\epsilon_{E_g(^1E_g)} = \tfrac{1}{2}\epsilon_{12} + \tfrac{1}{2}\left[(\epsilon_{12})^2 + \lambda^2\right]^{\frac{1}{2}}$$

Since only the (B_{1g}, B_{2g}), $E_g(^3E_g)$, and $E_g(^1E_g)$ states were located, the expressions for the energy separations between these states are symmetric with respect to exchange of λ and ϵ_{12}. Hence the absolute magnitudes of these two parameters are somewhat ambiguous and ϵ_{12} was assigned to the larger value.

Table A2.1. Spin-orbit coupling energy matrix for the $(e_g)^1(b_{2g})^1$ configuration in D'_{4h}.

	$\|E(^3E_g)\alpha\rangle$	$\|E(^3E_g)\beta\rangle$	$\|E(^1E_g)\alpha\rangle$	$\|E(^1E_g)\beta\rangle$
$\langle E(^3E_g)\alpha \|$	0	0	$\frac{1}{2}\lambda$	0
$\langle E(^3E_g)\beta \|$	0	0	0	$\frac{1}{2}\lambda$
$\langle E(^1E_g)\alpha \|$	$\frac{1}{2}\lambda$	0	ϵ_{12}	0
$\langle E(^1E_g)\beta \|$	0	$\frac{1}{2}\lambda$	0	ϵ_{12}

REFERENCES

1. Born, M.; Oppenheimer, R. Ann. Phys. 1927, 84, 457.
2. Marcus, R. A. in Techniques of Chemistry, Volume VI, Part 1; ed. E. S. Lewis, Wiley and Sons: New York, 1974.
3. Hill, T. L. "Introduction to Statistical Thermodynamics"; Addison-Wesley: Massachusetts, 1960.
4. Cotton, F. A.; Wilkinson, G. "Advanced Inorganic Chemistry"; 4th ed. Wiley and Sons: New York, 1980.
5. Schröder, F. A. Acta Cryst. 1975, B31, 2294.
6. Sheldon, R. A.; Kochi, J. K. "Metal-Catalyzed Oxidations of Organic Compound"; Academic Press: New York, 1981.
7. Ballhausen, C. J. "Molecular Electronic Structures of Transition Metal Complexes"; McGraw-Hill: London, 1979.
8. Liehr, A. D. Annals of Physics, 1957, 1, 221.
9. Rebane, K. K. "Impurity of Spectra Solids"; Plenum Press: New York, 1970.
10. Duschinky, F. Acta Phys. Chim. URSS 1937, 7, 551.
11. Merzbacher, E. "Quantum Mechanics" 2nd ed.; Wiley and Sons: New York, 1961.
12. Ansbacher, F. Z. Naturforsch. 1959, 14a, 889.
13. Herzberg, G. "Molecular Spectra and Molecular Structure" Vol I, Spectra of Diatomic Molecules: Van Nostrand; New York, 1950.
14. Yersin, H.; Otto, H.; Zink, J. I.; Gliemann, G. J. Am. Chem. Soc. 1980, 102, 951.
15. Strickler, S. J.; Berg, R. A. J. Chem. Phys. 1962, 37, 814.
16. Förster, T. Fluoreszenz organischer Verbindungen;

Vandenhoek and Ruprecht: Göttingen, 1951.

17. Dexter, D. L. J. Chem. Phys. 1953, 21, 836.

18. (a) An historical account of the development of the theory of non-radiative decay appears in a chapter by Robinson, G. W. Excited States 1974, 1, 1.

(b) A comprehensive review of this theory is presented by Freed, K. F. Top. App. Phys. 1976, 15, 23.

19. Bixon, M.; Jortner, J. J. Chem. Phys. 1969, 50, 3284.

20. Kubo, R.; Toyozawa, Y. Progr. Theoret. Phys. 1955, 13, 160.

21. (a) Collison, D.; Gahan, B.; Garner, C. D.; Mabbs, F. E. J. Chem. Soc., Dalton 1980, 667.

(b) Garner, C. D.; Kendrick, J.; Lambert, P.; Mabbs, F. E.; Hillier, I. H. Inorg. Chem. 1976, 15, 1287.

(c) Stiefel, E. I. Progr. Inorg. Chem. 1977, 22,1.

(d) Dori, Z. Progr. Inorg. Chem. 1981, 28, 239.

22. Ballhausen, C. J.; Gray, H. B. Inorg. Chem. 1962, 1, 111.

23. Gray, H. B.; Hare, C. R. Inorg. Chem. 1962, 1, 363.

24. Sasakim Y.; Sykes, A. G. J. Chem. Soc., Dalton 1974, 1468.

25. Marov, I. N.; Dubrov, Y. N.; Belyaeva, V. K.; Ermakov, A. N. Dokl. Akad. Nauk. SSSR 1967, 177, 1106.

26. Garner, C. D.; Hill, L. H.; Mabbs, F. E.; McFadden, D. L.; McPhail, A. T. J. Chem. Soc. 1977, 853.

27. Bino, A.; Cotton, F. A. Inorg. Chem. 1979, 18, 2710.

28. Cotton, F. A. Inorg. Synth. 1972, 13, 87.

29. Drushel, H. V.; Sommers, A. L.; Cox, R. C. Anal. Chem. 1963, 35, 2166.

30. Abragam, A.; Bleany, B. "Electron Paramagnetic Resonance of Transition Ions"; Oxford University Press: London, 1970.

31. (a) Kon, H.; Sharpless, N. E. J. Phys. Chem. 1966, 70, 105.
(b) Manoharan, P. T.; Rogers, M. T. J. Chem. Phys. 1968, 49, 5510.

32. (a) Garner, C. D.; Hillier, I. H.; Mabbs, F. E.; Guest, M. F. Chem. Phys. Lett. 1975, 32, 224.
(b) Garner, C. D.; Hillier, I. H.; Kendrick, J.; Mabbs, F. E. Nature, 1975, 258, 138.
(c) Garner, C. D.; Lambert, P.; Mabbs, F. E.; King, T. J. J. Chem. Soc., Dalton 1977, 1191.
(d) Garner, C. D.; Hill, L. H.; Howlader, N. C.; Hyde, M. R.; Mabbs, F. E.; Routledge, V. I. J. Less Common Met. 1977, 54, 27.

33. Weber, J.; Garner, C. D. Inorg. Chem. 1980, 19, 2206.

34. Figgis, B. N. "Introduction to Ligand Fields"; Interscience Publishers: New York, 1966.

35. (a) Horner, S. M.; Tyree, S. Y. Inorg. Chem. 1963, 2, 568.
(b) Patterson, H. H.; Nims, J. L. ibid. 1972, 11, 520.

36. Reference 7, p. 119.

37. Collin, R. J.; Griffith, W. P.; Pawson, D. J. Mol. Structure 1973, 19, 531.

38. Griffith, J. S. "The Theory of Transition-Metal Ions"; Cambridge University Press: London, 1961.

39. Jahn, H. A.; Teller, E. Proc. Roy. Soc. 1937, A161, 220.

40. (a) Gächter, B. F.; Koningsten, J. A. J. Chem. Phys. 1974, 60, 2003.

(b) Krasser, W.; Koglin, E.; Wiedemann, E.; Brocke, W. A. Z. Naturforsch. 1972, 27a, 1119.

41. Englman, R. "Non-Radiative Decay of Ions and Molecules in Solids"; North-Holland Publishers: Amsterdam, 1979.

42. Englman, R.; Jortner, J. Mol. Phys. 1970, 18, 145.

43. Freed, K. F.; Jortner, J. J. Chem. Phys. 1970, 52, 6272.

44. Gardner, W. C. "Rates and Mechanisms of Chemical Reactions"; Benjamin: California, 1972.

45. (a) Mo: Day, V. W.; Hoard, J. L. J. Am. Chem. Soc. 1968, 90, 3374.

(b) W: Samotus, A.; Dudek, M.; Kanas, A. J. Inorg. Nucl. Chem. 1975, 37, 943.

(c) Tc: Kastner, M. E.; Lindsay, M. J.; Clarke, M. J. Inorg. Chem. 1982, 21, 2037.

(d) Os: Malin, J. M.; Schlemper, E. O.; Murmann, R. K. Inorg. Chem. 1977, 16, 615.

46. Beard, J. H.; Calhoun, C.; Casey, J.; Murmann, R. K. J. Am. Chem. Soc. 1968, 90, 3389.

47. Murmann, R. K.; Schlemper, E. O. Inorg. Chem. 1971, 10, 2352.

48. Beard, J. H.; Casey, J.; Murmann, R. K. Inorg. Chem. 1965, 4, 797.

49. Hurd, L. C.; Reinders, V. A. Inorg. Syn. 1939, 1, 178.

50. Murmann, R. K. Inorg. Syn. 1966, 8, 173.

51. Sergienko, V. S.; Porai-Koshits, M. A.; Khodashova, T. S. Zh. Strukt. Khim. 1974, 15, 275.

52. Demas, J. N.; Crosby, G. A. J. Phys. Chem. 1971, 75, 991.

53. van Houten, J.; Watts, R. J. J. Am. Chem. Soc. 1976, 98, 4853.

54. Balzani, V.; Moggi, L.; Manfrin, M. F.; Bolletta, F. Coord. Chem. Rev. 1975, 15, 321.

55. Born, M.; Wolf, E. "Principles of Optics" 2nd ed.; Pergamon Press: New York, 1964.

56. Kubas, G. J.; Jones, L. H. Inorg. Chem. 1974, 13, 2816.

57. Fordyce, W. A.; Rau, H.; Stone, M. L.; Crosby, G. A. Chem. Phys. Lett. 1981, 77, 405.

58. "Handbook of Chemistry and Physics" 58th ed.; CRC Press: Ohio, 1977.

59. Adams, D. "Metal Ligand and Related Vibrations"; Edward Arnold Publishers: London, 1967.

60. Clark, R. J. H.; Williams, C. S. Inorg. Chem. 1965, 4, 350.

61. Omura, Y.; Nakagawa, I.; Shimanouchi, T. Spectrochim. Acta 1971, 27A, 2227.

62. Thomas, T. R.; Watts, R. J.; Crosby, G. A. J. Chem. Phys. 1973, 59, 2123.

63. Robbins, D. J.; Thomson, A. J. Mol. Phys. 1973, 25, 1103.

64. It is important to note that this derivation is based upon the assumption that a displaced harmonic oscillator model accurately reflects the nuclear wavefunctions in states Ψ_s and Ψ_n.

65. A similar result and similarly noncommittal conclusion are described in reference 62.

66. Morrison, R. T.; Boyd, R. N. "Organic Chemistry" 3rd ed.; Allyn and Bacon: Boston, 1974.

67. Chinn, L. J. "Selection of Oxidants in Synthesis; Oxidation at the Carbon Atom"; Marcel Dekker: New York, 1971.

68. Rowley, A. G. in "Organophosphorus Reagents in Organic Synthesis" ed. J. I. G. Cadogan; Academic Press: London, 1979.

69. (a) Shaw, E. N. in "The Chemistry of Heterocyclic Compounds, Pyridine and Its Derivatives" Part Two, ed. E. Klingsberg; Interscience Publishers: New York, 1961.

(b) Acheson, R. M. "An Introduction to Heterocyclic Compounds" 2nd ed.; Interscience Publishers: New York, 1967.

70. Collins, T. J. Caltech Industrial Associates Conference; March, 1983.

71. Dunn, T. M.; Francis, A. H. J. Mol. Spectrosc. 1968, 25, 86.

72. (a) V: Ronde, H.; Blasse, G. J. Inorg. Nucl. Chem. 1978, 40, 215.

(b) W: Treadway, M. J.; Powell, P. C. J. Chem. Phys. 1974, 61, 4003.

73. Burrows, H. D.; Kemp, T. J. Chem. Soc. Rev. 1974, 3, 139.

74. Nocera, D. G.; Maverick, A. W.; Winkler, J. R.; Che, C. M.; Gray, H. B. in "Inorganic Chemistry Toward the 21st Century" ed. M. H. Chisholm; American Chemical Society: Washington, D.C., 1983.

75. Ballhausen, C. J. "Introduction to Ligand Field Theory" McGraw-Hill: New York, 1962.